Laser-Induced Thermal Acoustics

Thesis by
Eric B. Cummings

In Partial Fulfillment of the Requirements
for the Degree of
Doctor of Philosophy

California Institute of Technology
Pasadena, California
1995

(Submitted 20 February 1995)

Acknowledgments

I express deepest gratitude to my advisor, Professor Hans Hornung, for his unfaltering patience and support. His enthusiasm, optimism, and wisdom have revived me in times of difficulty, and inspired me in times of triumph. I value his friendship dearly.

The members of GALCIT have made the past six years most enjoyable and enlightening. I would like to thank Professor Paul Dimotakis for his timely and helpful advice. I also thank Professor Bradford Sturtevant, Professor Hans Liepmann, Professor Anatol Roshko, Professor Joe Shepherd, Professor Mori Gharib, and Karen Cheetham for stimulating discussions and support. Ivett Leyva, Jeffrey Mach, and Bonifacio Calayag have provided much-appreciated assistance in experiments and data analysis. My thanks also goes to members of the T5 team: Phillipe Adam, Jacques Bélanger, Jean-Paul Davis, Patrick Germain, Patrick Lemieux, Simon Sanderson, Bahram Valiferdowsi, and Chihyung Wen for camaraderie and occasional commiseration.

My sincerest thanks goes to Dr. Michael Brown for the many hours of testing and brainstorming we have shared.

Finally, I thank my family, especially my mother, Barbara Cummings, and my father, Dr. Derald Cummings, and my wife-to-be, Kirsten Pace for helping me to appreciate the beauty of the world.

This research was funded by AFOSR Grant F49610-92-J-0110 (Dr. L. Sakell) and AFOSR grant F49620-93-1-0338 (Dr. J. Tishkoff). I thank the United States Office of Naval Research for funding my graduate education through their fellowship program.

Abstract

Laser-induced thermal acoustics (LITA) is a new technique for remote nonintrusive measurement of thermophysical gas properties. LITA involves forming, via opto-acoustic effects, grating-shaped perturbations of gas properties using intersecting beams from a short-pulse laser. A third beam scatters coherently into a signal beam off the perturbation grating via acousto-optical effects. The evolution of the gas perturbations modulates the scattered signal beam. Accurate values of the sound speed, transport properties, and composition of the gas can be extracted by analyzing the signal beam.

An analytical expression for the spectrum, absolute magnitude, and time history of the LITA signal is derived. The optoacoustic effects of thermalization and electrostriction are treated. Finite beam-diameter, beam-duration, and thermalization-rate effects are included in the analysis. The expression accurately models experimental signals over a wide range of gas conditions.

Experimental tests using LITA have been conducted on pure and NO_2-seeded air and helium at pressures ranging from ~0.1 kPa–14 MPa. Carbon dioxide has been explored near its liquid-vapor critical point. Accuracies of 0.1% in sound speed measurements have been achieved in these tests. Accuracies of ~1% have been achieved in measurements of thermal diffusivity, although beam misalignment effects have typically degraded this accuracy by a factor of ~10–20. Using LITA, susceptibility spectra have been taken of approximately a femtogram of NO_2. The effects of fluid motion and turbulence have been explored. LITA velocimetry has been demonstrated, in which the Doppler shift of light scattered from a flowing fluid is measured. LITA velocimetry requires no particle seeding, has a coherent signal beam, and can be applied to pulsed flows. LITA has also been applied to measure single-shot $|\chi^{(1)}|^2$ or "Rayleigh scattering" spectra of a gas using a technique of wavelength-division multiplexing, called multiplex LITA. The LITA apparatus used in these tests costs about one-tenth that of many conventional laser diagnostics. Narrowband LITA measurements of the sound speed and transport properties and multiplex LITA measurements of the spectral properties of gases may be taken in a single laser shot.

Table of Contents

List of Tables

List of Figures

List of Symbols

Upper-case English Symbols

$A_{\{D,P,T\}}$	defined by Eq. 8.2
$\mathbf{B}$	magnetic induction field vector
$\mathbf{D}$	displacement field vector
D_s	diffusivity of excited-state target molecules through fluid
D_T	thermal diffusivity of fluid
D_V	longitudinal kinematic diffusivity of fluid $(1/\rho(\eta_v + (4/3)\eta_s))$
D_{ij}	mutual diffusivity of species i and j
$\mathbf{E}, E$	electric field vector and amplitude
$\mathcal{E}$	slowly varying electric field envelope
E_d	energy per driver laser pulse
G	acoustic damping per cycle $(\Gamma q/c_s)$
$\mathbf{H}$	magnetic field vector
H_θ, H_e	defined by Eq. 5.14b
$H_{\{D,P,T\}}$	defined by Eq. 5.14e
H_{eP}, H_{eT}	defined by Eq. 5.14f
$\mathbf{I}$	identity tensor of rank 2
I	normalized spatial electric field distribution
$\mathcal{L}$	detected LITA signal intensity
M	characteristic equation of linear hydrodynamics, see Eq. 4.2d
N	number of species comprising the fluid
$N_{\{D,P,T\}}$	defined by Eq. 7.3b
$P(t)$	normalized time history of laser beam field amplitudes
P	pressure (distinguished from perturbation pressures in Sec. 4.2)
P_i	mean partial pressure of i-th species
$\mathbf{R}, R$	position vector of detector element and vector magnitude
$\mathcal{R}$	universal gas constant
T	mean absolute temperature
U	energy per unit volume

$\mathcal{U}_e, \mathcal{U}_\theta$	electrostrictive and thermal grating parameter, Eq. 5.12
V	characteristic speed of large scale turbulent motion

Lower-case English Symbols

b_e, b_T	amplitude of electrostrictive and thermal gratings, respectively
c	local speed of light
c_p, c_v	specific heat at constant pressure and volume, respectively
c_s	isentropic speed of sound
h	dimension of half-minor axis of grating in y-direction
$\mathbf{k}, k$	wave vector and vector magnitude
ℓ	dimension of half-major axis of grating (in x-direction)
m_i	molecular mass of i-th species
$\mathbf{n}, n_i$	vector of species concentrations, concentration of i-th species
p	mean pressure
p_i	partial pressure perturbation
$\mathbf{q}, q, q_x, q_y, q_z$	spatial Fourier transform vector, magnitude, Cartesian comps.
q_ϕ	grating/phase-matched scattering vector
$q'_{y\{D,T,P\}}$	defined as $q_y - q_\phi \eta^2_{\{D,P,T\}}$
$\mathbf{r}$	position vector
s	Laplace transform variable
t	time
$\mathbf{u}$	fluid velocity vector
w	driver-beam half-width
x,y,z	position vector components in the Cartesian frame shown in Fig. 3.1

Upper-case Greek Symbols

Γ	acoustic damping rate $(1/2[(\gamma-1)D_T + D_V])$
Δ	thermal grating damping over a period of acoustic motion
$\mathrm{H}_{\{D,P,T\}}$	length scale defined by Eq. 5.15d
Θ	arbitrary thermalization rate model in Eq. 5.10
$\Lambda_{\{D,P,T\}}$	length scale defined by Eq. 5.15d
Π	ratio of acoustic wave frequency to thermalization rate, Eq. 5.14g
$\Sigma_{\{D,P,T\}}$	defined by Eq. 7.3e

$\Phi_{\{D,P,T\}}$	defined by Eq. 5.14d
$\Phi^{(d)}_{\{D,P,T\}}$	defined by Eq. 5.15a–d
$\Phi^{(d,o)}_{\{D,P,T\}}$	defined by Eq. 7.3a
$\Psi_{\{D,P,T\}}$	defined by Eq. 7.3c
$\Omega_{\{D,P,T\}}$	length scale defined by Eq. 5.15d

Lower-case Greek Symbols

α	thermal expansion coefficient
γ	ratio of specific heats
$\gamma_{n\theta}$	rate of excited-state energy decay not caused by thermalization
γ_{θ}	rate of excited-state energy decay caused by thermalization
ϵ	dielectric constant
ϵ_0	vacuum dielectric constant
ζ	length scale defined by Eq. 8.3.b
$\zeta_{\{D,P,T\}}$	length scales defined by Eq. 7.3f
η_v, η_s	bulk and shear viscosities, respectively
$\eta_{\{D,P,T\}}$	length scales defined by Eq. 5.15d
θ	angle of driver beams with respect to x-axis
λ	wavelength
λ_g	grating wavelength
μ, μ	dipole moment density vector, vector magnitude
μ_m, μ_m	molecular dipole moment vector, vector magnitude
ξ	length scale defined by Eq. 8.3b
$\xi_{\{D,P,T\}}$	length scales defined by Eq. 7.3f
π	Hertz vector
ρ	mass density
σ	half-width of source beam
τ	trigger time delay
ϕ	angle of source beam with respect to x-axis
χ	dielectric susceptibility
χ_m	molecular electric susceptibility
ψ	divergence of the velocity
ω	angular frequency

Miscellaneous Symbols

$M.W.$	molar mass of gas mixture
$\dot{T}$	energy equation forcing term
$\dot{\Psi}$	momentum equation forcing term
$\dot{n}_i$	species diffusion equation source term
$\hat{\mathbf{e}}_i$	unit vector in i-th direction

Superscript Symbols

(1)	linear (used for linear susceptibility $\chi^{(1)}$)
(d)	including driver beam spatial effects
(o)	including source beam spatial effects

Subscript Symbols

D	related to the creation of the thermal grating
P	related to the acoustic waves
T	related to the thermal grating
d	related to the driver beams
e	related to electrostriction
ex	related to excited states
het	related to heterodyne detection
hom	related to homodyne detection
i, j	related to the i-th or j-th species, respectively
m	related to a molecule
$n\theta$	not related to thermalization
o	related to the source beam
s	related to the signal beam
1	related to a perturbation, except where noted
θ	related to thermalization

Part I. Background Material

CHAPTER 1

Introduction

This thesis describes a new laser measurement technique developed by the author, called laser-induced thermal acoustics (LITA). LITA is a laser-based technique for remotely measuring physical and chemical properties of fluids. LITA can remotely and nonintrusively measure the sound-speed and transport properties of a fluid with accuracy comparable to the best conventional intrusive methods. LITA can measure the velocity of a fluid in pulsed or particle-laden flows where other techniques of velocimetry fail. LITA can measure properties of chemical species in extremely low concentrations, exceeding the sensitivity of other laser-measurement techniques in gases at and above atmospheric pressure. For example, in Chapter 11, high-resolution and noise-free susceptibility spectra of about *a femtogram* of NO_2 are presented. LITA excels in high-pressure environments, where many other diagnostics fail, permitting its use in studying high-pressure combustion. The development of the technique has necessarily addressed issues that are not often considered in laboratories that specialize in laser diagnostics: the need to make measurements in a single laser pulse, the need to make measurements in extremely challenging environments, and the need to make measurements using affordable experimental apparatus. This thesis contains a description of the physics of LITA, a derivation of an accurate analytical expression for the LITA signal, experimental validation of the expression, results of a variety of experiments exploring potential applications of LITA, and experimental notes to assist future users of LITA.

1.1 Motivation

While laser techniques to measure properties of flowing and combusting fluids have been in development since the earliest lasers became available, all techniques suffer limitations. Many of these techniques are adversely affected by molecular collisions and are thus limited to low-pressure studies, e.g., laser-induced fluorescence (LIF), degenerate four-wave mixing (DFWM).* Some techniques are limited to probing species that exist in high concentrations, e.g., Raman scattering, coherent anti-Stokes Raman scattering (CARS), etc. (Eckbreth, 1988). The signals from many techniques are difficult to analyze. For example, LIF suffers from its reliance on modeling of a large number of energy transfer processes in order to interpret signals quantitatively. This modeling currently requires exhaustive study of the interactions with potential collision partners and internal energy transfer mechanisms of the target molecule. After many years of development, LIF measurements of temperature in a well-behaved laboratory flame are ~10% uncertain. DFWM signals are also generally difficult to model accurately. Accurate modeling of the DFWM signal spectrum from a single spectral line of a species currently requires about a day's processing time on a workstation computer (Lucht et al., 1993).** Modeling of broadband or *multiplex* DFWM signals (used to obtain single-shot measurements) is even more formidable (Cooper, 1989).

Realizing the limitations of conventional laser techniques, the author developed LITA as a nonintrusive diagnostic technique for use on the T5 hypervelocity shock tunnel. T5 is a free-piston shock tunnel capable of creating the flow speeds and chemical reactions that occur in hypersonic atmospheric flight and atmospheric re-entry. This flow facility is described in Hornung et al. (1992). The flow in the tunnel is pulsed, lasting for approximately 2 ms. Shock heating of the gas during tests can create flow regions with temperatures ~10,000 K, about twice the temperature of the surface of the sun, or three times the temperature of molten lava. These regions of the flow create high levels of luminosity. Particulates are also apparent in the flows. The

---

* A semantic distinction is drawn that DFWM derives its signal from population gratings while LITA uses gratings that evolve on hydrodynamic time-scales, e.g., thermal gratings. This distinction is well-justified in the mathematics and physics of the two techniques, and will be clarified in Chapter 2.

** However, modeling of DFWM spectra with sufficient accuracy for diagnostic purposes is much more practical, e.g., ~10 minutes for a 50-line NO spectrum.

turn-around time between tests is of the order of two hours. Conventional laser spectroscopic techniques were considered to be inconsistent with the challenging physical environment and practical requirements of the T5 laboratory. Laser-scanning experiments and techniques inherently limited to single-point measurement were considered impractical. Techniques which provide only semi-quantitative information were not considered to be worth the required effort and expense. Techniques requiring large quantities of ancillary experimental data and computational effort were likewise dismissed. The technique had to employ equipment that was available or readily designed and built in-house and had to be robust enough for use on T5.

In 1992, the author realized that measurement using a technique later called LITA should satisfy the requirements of T5. At that time however, LITA had not been demonstrated as a diagnostic technique. An adequate analysis of the LITA signals from which to extract gas-property information or predict signal levels did not exist. Thus the author derived an approximate expression for the absolute intensity and time-history of the LITA signals and began building an experiment to test the analysis. Ten months later, the first single-shot LITA signals were detected using this apparatus. These signals validated the author's analysis and demonstrated the importance of hitherto neglected beam-size effects. These additional effects were later treated in the analysis which is presented in this thesis. A variety of experimental applications of LITA have been implemented. Selected results of these experiments are presented in Chapter 11.

The analytical expression presented in this thesis accurately models experimental signals. Using the analytical model as a basis for a nonlinear filter of the experimental data, fluid properties including the sound speed, thermal diffusivity, bulk viscosity, and linear susceptibility have been measured from experimental signals.† Calibrated measurements of the sound speed agree with independent, published values typically within 0.1%. Agreement within ~1% of independent published values of the thermal diffusivity has been achieved through LITA measurements at high pressures, although typical results are less accurate because of modeling and experimental non-idealities.

† The nonlinear filter is a nonlinear least-squares fitting routine which adjusts gas property and beam geometrical parameters until the best match between experimental and modeled signals is found.

The numerical filtering of the experimental signals has been automated. Filtering of a 2000-(time) point experimental signal typically requires ~1 minute on a Sun Sparc 5, during which the modeled signal is calculated ~100 times. The practicality of such filtering attests to the benefit of having an accurate analytical model of the signal.

Using LITA, fluid properties have been accurately measured without knowledge of any details of intra- and inter-molecular energy transfer, or spectroscopic properties of the fluid. LITA signals are directly modulated by fluid processes, such as diffusion and wave motion, not molecular processes, such as rotational and vibrational energy transfer. While molecular excited state quenching affects LITA signals, LITA is largely insensitive to the details of quenching processes.‡ Thus, unlike other laser-based gas-property diagnostics, LITA measures fluid properties directly.

As interest in the technique grows, LITA is being pursued as a flow and combustion diagnostic technique in a growing number of laboratories. LITA excels at high pressures or molecular collision rates, required for rapid chemical reactions. LITA can remotely measure transport properties, essential for modeling of combustion and hot-hypersonic flows. Various implementations of LITA to measure flow velocity, absolute species concentration, and mutual diffusion coefficients are in active development at the Graduate Aeronautical Laboratories of the California Institute of Technology (GALCIT). LITA experiments are planned for the near future on T5 and also in a NASA experimental next-generation jet engine combustor, highlighting a remarkably rapid technique development.

1.2 Laser-induced Thermal Acoustics (LITA)

The physics behind the generation of LITA signals is discussed throughout this thesis. An overview is useful to provide insight into LITA before digesting the details of the physics. LITA scattering involves two steps: *driving* of perturbations of a medium via opto-acoustic effects and *coherent scattering* of light off these perturbations into a coherent signal beam via acousto-optic effects.

---

‡ LITA signals are sensitive to the overall quenching rates.

In the driving step, light from a powerful pulsed laser is split into two phase-coherent beams that intersect at a shallow angle in the medium. The region of intersection of the beams defines a sample volume of the LITA measurement. Interference of the driver beams creates an electric field intensity grating in the sample volume.‡ The medium responds to the intensity of these driver beams in several possible ways. In an effect called thermalization in this thesis, light energy can be absorbed by the medium, subsequently heating the medium locally. The medium expands thermally upon heating. If the thermal expansion speed is comparable to the sound speed, sound waves are generated. A second, less intuitive effect called *electrostriction* also occurs. In electrostriction, molecules of the medium are either accelerated toward or away from regions of intense light, depending on molecular properties. If the driving is rapid, the acceleration is impulsive and sound waves are created. If the driving is slower, the molecules diffuse into or away from the regions of intense light, thereby creating species concentration gradients in the medium. Thus the driver laser can perturb the bulk properties of the medium by forming thermal gradients, concentration gradients, and sound waves. These effects are a subset of the many mechanisms by which the macroscopic properties of the gas may be perturbed by intense optical electric fields. In this thesis, these mechanisms are called opto-acoustic effects and are described quantitatively in Chapter 5.*

The perturbations induced by the driver laser create perturbations in the susceptibility of the medium (and therefore the index of refraction) via acousto-optic effects. These perturbations therefore have the appearance of volume diffraction gratings. In the coherent scattering step, a CW or long-pulse source laser is trained on the sample volume at the Bragg-angle of the gratings. Light from the source laser is scattered off the gratings into a coherent, or laser-like, signal beam. The signal beam is detected using large f-number optics, and is often many orders of magnitude stronger than incoherently scattered light.

The signal beam is modulated in time by the evolution of the laser-induced per-

‡ Figs. 3.1 and 3.2 show schematically the driving and scattering geometries described here.

* This definition of opto-acoustic effects is generalized from the standard definition, since it includes effects which create perturbations that propagate at zero wave speed, unlike ordinary acoustic waves.

turbations. From this modulation, accurate physical properties of the medium may be inferred, including the sound speed, thermal diffusivity, and other properties that affect the evolution of the laser- induced gratings. The concepts sketched here are expounded in the remainder of the thesis.

1.3 Overview

This thesis contains four major sections. The first covers background material included in this chapter, and in Chapter 2, a review of work relevant to the development of LITA. The second section, spanning Chapters 3 through 8, is the derivation from the linearized equations of hydrodynamics and light scattering of an analytical expression for LITA signals from finite beams. Discussions and interpretations of the physics clarified by the derivation punctuate the algebra in these chapters. The author elected not to exclude major steps of the analysis so that future researchers would be able to amend or tailor the analysis to their specifications without undue duplication of effort. Experiments, data analysis, and results of various applications of LITA fill the third section which spans Chapters 9 through 11. Experimental notes and pitfalls are discussed in Chapter 11. The final section which includes Chapters 12 and 13 attempts to answer the questions 'what have we learned?' and 'what next?'.

CHAPTER 2

Review of Developments Relevant to LITA

LITA is a hybrid technique arising from a cross-pollination between the fields of dynamic light scattering and optical four-wave mixing. Dynamic light scattering is a means of measuring the evolution of random thermal and acoustic fluctuations in a medium by measuring properties of light scattered off the dielectric field perturbed by these fluctuations. Optical four-wave mixing (FWM) occurs when two light beams perturb the dielectric field of a medium and the perturbed field scatters light from a third beam into a fourth beam. The properties of the fourth beam can provide information about physical properties of the medium in which the mixing occurs. If the frequencies of the beams are the same, the optical interaction is called degenerate four-wave mixing (DFWM).

The advent of laser light made both fields practical. Dynamic light scattering measurements require laser light's high spectral brightness for adequate signal level and purity. Four-wave mixing, a nonlinear phenomenon, requires high field intensities since most materials are only weakly nonlinear. Thus the history of the development of LITA begins in the middle of the 1960's.

2.1 Dynamic Light Scattering

Light scattering is a common phenomenon, responsible for sunbeams, blue skies, and blue oceans. Perturbations in the susceptibility of a medium scatter light. Light passing through a polarizable medium induces microscopic oscillating dipole moments in the constituent molecules. These oscillating dipoles re-emit light like an array of dipole antennas, each dipole having no directivity. By symmetry, the light emitted by ordered or homogeneous collections of dipoles adds up in phase only in the direction of motion of the incident light. Phase cancellation occurs in every other direction (except as provided by diffraction from a finite array of dipoles). Thus, ordered or homogeneous media do not scatter light. However, disturbances in the dielectric constant of the medium break this symmetry, allowing imperfect phase cancellation of the re-emitted light, or light scattering. Einstein (1910) showed that dielectric disturbances from random thermal-density fluctuations cause the natural scattering phenomena listed earlier, called Rayleigh scattering. Random microscopic acoustic pressure waves scatter light in Brillouin scattering. Random fluctuations in molecular orientation, chemical composition, quantum state population, similarly produce scattered light. The heading "dynamic light scattering" categorizes the quantitative study of these forms of light scattering. Berne and Pecora (1976) provide a lucid description of the study and history of dynamic light scattering.

A linearized equation of light scattering derived from Maxwell's equations describes these weak scattering phenomena accurately. A derivation of this equation modified only slightly from that of Landau and Liftshitz (1960) appears in Appendix A. The magnitude of the scattered electric field far from the scatterer at a given scattering angle is proportional to a single Fourier component of the scattering fluctuation field, defining a scattering wavelength. Thus, angularly resolving the scattered field intensity provides a measure of the fluctuation-scale distribution. The finite lifetimes of the fluctuations with the scattering wavelength broaden the spectrum of light scattered at a particular angle from a monochromatic source. Since the fluctuations decay by diffusion and molecular processes, the spectrum of the scattered light provides a window for quantifying transport properties of the fluid. The fluctuations responsible for Brillouin scattering propagate as sound waves in the fluid. The light scattered off these structures bears a Doppler shift that is proportional to the sound speed. These shifts are quite small compared to the frequency of light and

are only observable using narrow-bandwidth laser light. The high spectral resolution (one part in approximately 10^9) needed to resolve these shifts usually mandates the use of optical heterodyne detection in dynamic light scattering.

Landau and Placzek (1934) performed early analysis in this field, deriving a simple expression for the relative strengths of spontaneous Rayleigh and Brillouin scattering. Mountain (1966), using the technique suggested by Landau and Placzek (1934), derived the spectral distribution of light scattered by a simple fluid using the linearized equations of hydrodynamics. This study permitted quantification of the thermal diffusivity, acoustic damping rate, and sound speed of a fluid given a scattering spectrum at a particular scattering angle. Mountain stressed the application of the dynamic light scattering technique to the measurement of thermophysical gas properties near the liquid-vapor critical point, citing the ability of such measurements to be made with minimal perturbation to the system. Numerous researchers have applied dynamic light scattering to the study of critical-point phenomena, e.g., see Green and Sengers (1966), Berne and Pecora (1976).

Dynamic light scattering remains in wide use thirty years after its practical inception, a fact that speaks highly of the technique. However, there are several notable shortcomings that arise from the incoherence of the technique. The incoherence of the scattered light forces detection using low-f-number optics, which limits the angular resolution of the scattered light, increasing the uncertainty of derived measurements. The signals are weak, often requiring long time-averages to obtain acceptable signal-to-noise ratios. The necessity of signal averaging prevents use of the technique to make measurements of pulsed and unsteady phenomena. Averaging dramatically complicates heterodyne detection, which is sensitive to optical phase drift. The technique is sensitive to incoherent scattering from particulates (Mie scattering) and reflections.

Randomly excited fluctuations intrinsically produce incoherent scattered light. LITA improves over pure dynamic light scattering by *coherently* exciting "fluctuations" with the desired Fourier component. The scattered signal emerges as a beam that may be many orders of magnitude stronger than the incoherently scattered signal. This improvement links the dynamic light scattering nature of LITA with the burgeoning field of optical four-wave mixing.

2.2 Laser-Induced Grating Spectroscopy and Four-Wave Mixing

The advent of optical four-wave mixing (FWM) closely follows the development of the laser. The pioneering text by Bloembergen (1965) codified the then-nascent field of nonlinear optics, the principle behind four-wave mixing. Boersch and Eichler (1967) demonstrated spatial "hole burning" in a ruby laser rod using a clever scheme in which the periodic modulation of the gain (and thereby susceptibility) in the laser rod caused by hole burning acted like a diffraction grating. This grating coherently scattered light from a second laser into a signal beam, which he detected. Thus was born the field of laser-induced grating spectroscopy. The applications and development of laser-induced grating spectroscopy are far too expansive to outline in this brief history. Regrettably, this survey overlooks a wealth of interesting and brilliant applications of laser-induced grating effects in favor of the most germane work. The interested reader is guided to Eichler (1986), an excellent and inclusive review of early developments in laser-induced dynamic grating work.

This survey ignores the distinction between optical four-wave mixing and light scattering off laser-induced dynamic gratings.** The nomenclature "four-wave mixing" tends toward the mathematical interpretation of nonlinear signal mixing, while the "dynamic grating" nomenclature tends toward the physically intuitive interpretation. The field encompasses a wide variety of techniques, all of which are mathematically similar, and many of which are physically similar. A laser-induced dynamic grating technique involves the formation of a coherent perturbation "grating" in a medium using two coincident laser beams. Usually laser-induced gratings contain multiple sinusoidal periods, as one would ordinarily suppose of a grating, although gratings may contain only a partial cycle. The third-order nonlinear response of the medium creates a material property or population grating with the shape of the optical intensity interference pattern of the coincident beams.† If the coincident beams have different frequencies, they form field intensity gratings with a finite phase velocity. Beams with the same frequency in the frame of the medium, i.e., degenerate beams, form stationary gratings. This thesis only considers gratings formed by degenerate

** The term "four-wave mixing" applies only to techniques using the third-order nonlinearity of a medium. Laser-induced dynamic gratings may arise from nonlinearities of any order.

† More precisely, gratings are formed as a result of the interaction of one beam with the molecular oscillation induced by the other and vice versa. Thus there is no requirement that the beams be temporally coincident.

and nearly degenerate beams in which the phase speed of the grating is many orders of magnitude smaller than that of the grating-forming light. In FWM, the presence of the grating in the medium causes an accompanying susceptibility grating. This susceptibility grating scatters light from a third beam into a signal beam. The signal beam bears information about the nonlinear physical process and other properties of the medium. Shen (1986) provides a good review of FWM physics and technique.

In LITA, a sequence of opto-acoustic and acousto-optic effects generate the signal beam. Classical acoustic-scale material perturbation gratings are formed from opto-acoustic effects such as thermalization, electrostriction, photophoresis, and photolysis. In thermalization, super-elastic molecular collisions convert excited-state energy absorbed from laser light into thermal energy. In electrostriction, gradients in the potential of induced-dipole moments accelerate molecules in a non-uniform optical electrical field. In photophoresis, bulk migration of species occurs, for example by diffusion during the prolonged application of an electrostrictive field. In photolysis, laser-induced chemical reactions produce chemical species, thermal, and pressure perturbations. Acousto-optical effects include the change in susceptibility with density, temperature, and composition, among other properties. These classical nonlinearities are physically distinct from "quantum-mechanical" nonlinearities involving quantum-state population dynamics.

One of the earliest-observed nonlinear scattering effects is that of stimulated Brillouin scattering (SBS). In stimulated Brillouin scattering, a high-intensity laser pulse propagates into a nonlinear medium. A small fraction of the propagated light is back-scattered from random fluctuations, interfering with the forward-propagating light to form a weak intensity grating. This grating creates a weak density grating through a medium nonlinearity, notably electrostriction or thermalization. The density grating creates a susceptibility grating which back-scatters more light, providing a gain mechanism for the back-scattered beam. Large gains in the quantity of back-scattered light arise when the grating matches the phase-velocity and wavelength of sound waves in the medium. SBS in transparent and absorbing liquids may achieve high back-scattering efficiencies (~50%).‡ The back-scattered beam in SBS is down-shifted in frequency by the frequency of the induced sound waves. SBS has been

‡ There are other related stimulated back-scattering effects, e.g., Stimulated Rayleigh Scattering, of somewhat lesser renown.

widely studied because the back-scattered beam is the phase conjugate of the incident beam. The term "phase conjugate" comes from the usual complex exponential depiction of light waves. The phase conjugate of a wave is the complex conjugate of the exponential depiction of the incident wave, essentially a time reversal of the wave. Thus, the phase conjugate beam retraces the original path of the incident beam through an optical system, reversing any aberrations encountered along the way.‡ Early work in the analysis of SBS was performed by Herman et al., (1967) and Pohl et al., (1968) who extended Mountain's analysis (1966) of dynamic light scattering to include forcing terms for electrostriction and thermalization, which were considered to be proportional to the instantaneous field intensity. Since then there have been numerous experimental studies of SBS, mostly of its phase-conjugation efficiency and fidelity (Ottusch, 1991; Hu, 1989; Schelonka, 1989), and its applications, for example in phase-conjugate laser mirrors (Miller, 1989), and spectroscopy (Faris, 1990). Nonlinear effects in SBS have been also been studied using simplified optical and fluid equations (Masson, 1991). The field is a topic of continued study for commercial and scientific applications.*

Noteworthy among early research in FWM is the contribution of Key et al. (1970), who generated volume thermal gratings in a cell containing absorbing liquids using a Q-switched ruby laser and its (SBS) back-scattered phase conjugate beam.** A CW argon-ion laser probed the laser-induced grating. The decay rate of the thermal grating was poorly resolved because of the geometry of the grating-forming beams. Nevertheless, the experiments are notable for their remarkable sophistication. Winter et al. (1992) have recently used a SBS-back-scattered beam in gas-phase degenerate four-wave mixing (DFWM) experiments, a tribute to the work of these pioneers. Key et al. discussed the potential to measure electrostriction and Kerr rates, although these were hopelessly fast for their apparatus.

Another of the early pioneers of the use of laser-induced thermal and acoustic gratings was Eichler (1972) who used an absorbing liquid film for the nonlinear

---

‡ Of course the frequency shift and any changes in the optical aberrations during the transit and return time of the beam limit the fidelity of aberration correction.

* The first lasers with SBS phase-conjugate mirror technology have become commercially available this year.

** ...yet another dynamic grating effect!

medium. In these experiments, a pulsed ruby laser excited a thermal grating in the film, forming a transient hologram of the grating-forming beams. A delayed pulse from the ruby laser or a CW beam from an argon ion laser "reconstructed" the image of a grating-forming beam onto a detector that measured the holographic reconstruction intensity (thus grating modulation depth) in time. The decay rate of the grating agreed well with that calculated from a 1-D heat-transfer analysis. This work was originally performed to evaluate the resolution and power requirements of real-time holography. However, it helped to spawn the use of laser-induced dynamic gratings to observe and measure molecular and continuum relaxation processes. Eichler termed scattering from thermal and acoustic gratings, forced light scattering.

With improved time resolution and technique, laser-induced thermal gratings have probed the elasticity coefficients and thermal diffusivities of solids and liquids. Calling the technique forced Rayleigh scattering (FRS), Desai et al. (1983) extended Mountain's analysis of dynamic light scattering to obtain simplified equations for the signal from FRS considering instantaneous thermalization and neglecting spatial effects.

A development that has significantly improved FWM measurement capabilities is the picosecond mode-locked laser, whose pulse is short enough to probe fast dynamics. A mode-locked picosecond Nd:YAG laser generated acoustic waves via electrostriction and absorption in crystals (Nelson et al., 1980, 1981) and liquids (Miller et al., 1982; Wiese, 1989; Yiping et al., 1992). Calling the technique, laser-induced phonon scattering and laser-induced ultrasonics, Nelson et al. and Miller et al. measured sound speed and acoustic attenuation by scanning the time delay from grating formation and scattering from a picosecond source laser. Charmet et al. (1986) performed an interesting study of turbulence in a liquid undergoing plane Poiseuille flow by measuring the intensity of light scattered off convecting laser-induced thermal gratings.

2.3 Degenerate Four-Wave Mixing

In developments parallel to those of thermal/acoustic scattering, degenerate four-wave mixing (DFWM), in which all waves of the nonlinear interaction bear the same frequency, arose as a sensitive coherent technique with potential for combustion diagnostics. The technique is sensitive when its signal is resonantly enhanced by tuning the laser frequency to that of a molecular electronic dipole transition. Also, using a backward phase conjugate DFWM beam geometry mitigates Doppler broadening of spectral lines by thermal motion of a fluid and produces a signal beam that is proportional to the phase conjugate of one of the input beams. Abrams and Linde (1978) derived an expression for the intensity of the DWFM signal scattered from population gratings induced in two-level stationary atoms by monochromatic plane-wave beams. Various extensions of this approximate analysis have been derived (e.g., Gruneisen, 1985; Cooper, 1985, 1989), but general quantitative signal interpretation remains elusive. Nevertheless, DFWM has been used to detect radicals in a flame (e.g., Dreier et al., 1990; Bervas et al., 1992; Brown et al., 1992; Ewart et al., 1991, Rakestraw et al., 1990) and has been used otherwise in spectrochemical analysis (e.g., Ramsey et al., 1987; Rose et al., 1987; Fourkas et al., 1991 Vander Wal et al., 1992; and many others). For combustion diagnostics, DFWM was to have employed nonlinearities related to laser-induced, quantum-state population gratings. At moderate pressures, e.g., above ~100-1000 torr, however, collisions may quench the population gratings rapidly, forming thermal gratings and acoustic waves. Experimenters accustomed to quantum-mechanical grating techniques discovered that thermal and acoustic grating signals "contaminated" the signals from population gratings.

2.4 Developments in Laser-Induced Thermal Acoustics

This discovery forged a link between the fields of thermal/acoustic light scattering and DFWM. D. W. Chandler of Sandia National Laboratories Combustion Research Facility, in a private communication with the author, described acoustic oscillations he, Buntine and Hayden had observed in signals obtained by time delaying the third beam in a two-color (dual frequency) four-wave mixing experiment (Buntine et al., 1994). Chandler recommended pursuing the technique that is explored in this thesis over that of DFWM thermometry. Following a suggestion by P. E. Dimotakis at

GALCIT, the author sought to establish the practicality of the technique. The author found Mountain's 1966 derivation of the hydrodynamics in dynamic light scattering in Berne and Pecora (1976) and modified it with a thermal forcing term given by a rate-equation description of the thermalization of excited-state energy. Using this analysis and an expression for linear light scattering from Landau and Liftschitz (1960), the author derived an analytical expression for the absolute magnitude and time history of such signals (Cummings, 1992). The author termed the technique, laser-induced thermal acoustics (LITA) to differentiate it from DFWM.

Govoni et al. using a two-laser, two-color, time-delay-scanning technique, reproduced Chandler, Buntine, and Hayden's observation of the acoustic response of the fluid (Govoni et al., 1993a). By tuning the grating-forming laser off resonance, they measured signals which they subsequently attributed to electrostriction (Govoni et al., 1993b). The author independently made a series of exploratory narrowband LITA measurements of laboratory air (Cummings, 1993), demonstrating the variation of electrostriction and thermalization behavior with laser-tuning and validating the previous analysis. In this study, the author detected atmospheric NO_2 in concentrations less than 50 parts-per-billion, demonstrating the sensitivity of the technique. Seeding the gas with NO_2 provided single-shot LITA signal levels that enabled accurate single-shot measurement of thermal diffusivity, acoustic damping coefficient, and sound speed (Cummings, 1994a, 1994b). Working independently, (Stampanoni-Panariello et al., 1994) detected narrowband LITA signals caused by nonresonant electrostriction in air using time-delay scanning techniques.

Williams et al. (1994) obtained time-resolved LITA signals in an atmospheric flame by time-delay scanning of the grating probing beam. Paul et al. (1995) adapted Mountain's 1966 analysis to include forcing by finite-rate thermalization and electrostriction and compared theoretical predictions with experimental FWM measurements also time-resolved by time-delay scanning of the probing beam.

Having demonstrated the importance of finite-beam size effects in LITA signals in the first series of LITA experiments, the author derived an expression for LITA signals from finite Gaussian laser beams with temporal laser effects and the complete spatial effects of the hydrodynamic evolution of the laser-induced gratings (Cummings et al., 1995). This analysis also treated heterodyne signal detection, used in

a form of LITA velocimetry that the author proposed. The analysis predicted the spectrum of scattered light in multiplex LITA, a single-shot technique proposed by the author to measure absolute and relative species quantum-state populations and thereby temperature. The analysis treated the acousto-optical effects of electrostriction and finite-rate thermalization. Detector-size effects and the "proper" physical picture of LITA were discussed for the first time to the author's knowledge.

With assistance from H. G. Hornung, M. S. Brown, I. A. Leyva, J. Mach, and B. Calayag, the author conducted a second series of tests that verified the accuracy of the improved model. Sound speed, transport property, susceptibility, velocity, and turbulence measurements were taken in a variety of NO_2-seeded and pure gases including air, helium, and CO_2, over a pressure range from 0.1 kPa–20 MPa using LITA in a high-pressure bomb with optical access. Calibrated sound speed measurements of air above ~50 kPa (absolute) agreed with published values better than 0.1%. Measurements of the thermal diffusivity within ~10% of published values were made over the same range of conditions, with accuracy limited by beam-misalignment and thermalization rate effects. With well-aligned beams, LITA measurements of transport properties have achieved ~1% agreement with published values. The properties of CO_2 near its critical point were explored. Sensitive measurement of visible spectra of laboratory air by driver-laser-frequency scanning revealed the presence of the pollutant NO_2 in concentrations less than fifty parts-per-billion. These exceptional results are harbingers of the capabilities of measurement using LITA. Wide interest in the technique promises to accelerate the development of LITA into a precision scientific tool used in studies of gas-dynamics, combustion, fluid physics, and physical chemistry.

Part II. Derivation of an Analytical Expression for LITA Signals

CHAPTER 3

Overview of LITA Analysis

Before embarking on the analysis that occupies the next five chapters, it is useful to present the main assumptions made, summarize the steps, and illustrate the beam geometry treated in the analysis. Interspersed between equations are interpretations of the physics they describe, discussions of the assumptions leading to the results, and descriptions of potential extensions and generalizations of the analysis. Chapter 6 discusses the physics behind the mathematical results for the fluid response to laser driving. The analysis of acousto-optics follows, ultimately leading to analytical solutions for the detected scattered field from laser-induced thermal acoustics.

The principal assumptions made in the analysis are discussed in the derivation. It is handy to have them compiled here to save the interested reader undue eye-strain. Linear hydrodynamic behavior is assumed. This assumption is valid only if the grating wavelength is considerably larger than the mean-free molecular path of the fluid. Also, the magnitude of perturbation must be small. For instance, the thermal perturbation field should not alter the sound-speed field appreciably. For simplicity, perfect-gas behavior is assumed, although this restriction can be trivially relaxed by a change in nomenclature. The driver and source laser are assumed to be monochromatic and Gaussian in space, with planar wave-fronts in the region where they intersect. The beams are assumed to be perfectly aligned and in-plane. Both these assumptions are made for notational brevity, although the results may be readily modified to include in-plane source-beam misalignment without further approximation. The temporal envelope of the beams is assumed to vary slowly compared to the frequency of the beams. The convection velocity is assumed to be identically zero, although simple modifications permit approximate use of the analysis in certain well-behaved velocity fields. Species concentration gratings are ignored, although the framework is presented for the extension of the analysis to include them. Single-rate

thermalization is assumed, although a simple extension permits approximate multi-rate models to be used. Absorption and scattering are assumed to be linear. The divergence angle of the signal beam is assumed to be much smaller than the scattering angle.† The propagation of the acoustic waves is treated approximately, in effect ignoring high-order effects in the diffraction of the acoustic wave.

Chapters 4–6 describe the formation and evolution of the driver-laser induced gratings. Chapter 4 lists the equations that describe the evolution of perturbations in a fluid. The three-dimensional linearized equations of hydrodynamics are solved by Laplace and Fourier transform techniques, assuming uniform gas composition. This solution may be considered a Green's function for linear hydrodynamic evolution in Laplace and Fourier transform space. The equations of species diffusion for multiple-component gases are also presented, linearized, and transformed to a system of linear algebraic equations. These may be solved with the equations of hydrodynamics to obtain the evolution of species concentration perturbations.

Chapter 5 contains derivations of equations for opto-acoustic forcing by electrostriction and thermalization. Electrostriction is essentially instantaneous on LITA time-scales. Thus a quasi-steady model of electrostriction, in which the effect is proportional to the instantaneous field intensity, is used. Thermalization involves molecular quenching, thus its dynamics cannot generally be ignored on LITA time scales. Thermalization is treated by a simple rate equation involving the laser-induced excited-state energy density and its quenching rates. Other opto-acoustic effects, including photo- and thermo-phoresis are discussed. These additional effects generate species concentration gratings and are not pursued further. The specific driver-beam electric field distribution assumed in this part of the analysis is illustrated schematically in Fig. 3.1. The two driver beams have a Gaussian electric field profile with $1/e$ electric field amplitude half-widths of w. The beam crossing half-angle is θ, the height of the sample volume—the ellipsoidal region of intersection of the Gaussian beams—is h, the length of the sample volume is ℓ. Where the beams intersect, they interfere, forming an electric field intensity grating that is "written" into the fluid by the opto-acoustic effects. At the end of Chapter 5, the opto-acoustic driving terms

† This assumption is satisfied for gratings with many fringes.

from the assumed driver laser fields are substituted into the Laplace- and Fourier-transformed Green's function solution of the equations of hydrodynamics. Laplace and Fourier inversion provide the density perturbation field in three space dimensions and time.

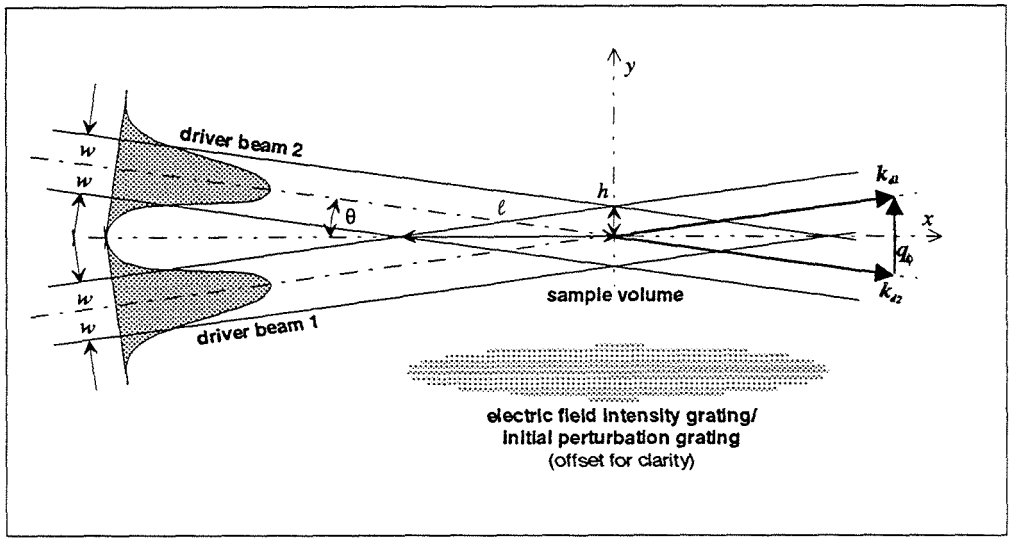

FIG. 3.1. Schematic diagram of the driver-beam field distribution. The axes and definitions correspond to those in Ch. 5 and the remainder of the analysis.

Chapter 6 describes in physical terms the results of the derivation of the density perturbation evolution. An illustration shows the difference in the nature of the gratings produced by electrostriction and thermalization. The effects of driving with finite-duration lasers and finite thermalization rates are discussed.

Chapter 7 treats acousto-optical scattering, emphasizing scattering from density perturbations, usually the most important acousto-optical effect in gases. A Gaussian source-beam field distribution is assumed. The geometry of the field and the gratings is as shown in Fig. 3.2. The half-width of the beam is σ, and the crossing angle is ϕ, the phase-matched or Bragg angle. The signal beam emerges at this angle as by a mirror reflection off the gratings. The scattered electric-field amplitude is obtained from the equation derived in Appendix A for the far field of linearly scattered light and the solution for the laser-induced perturbation field.

Finally, the solution for the signal beam is integrated over a detection angle to obtain the absolute magnitude and time-history of the LITA signal in Chapter 8.

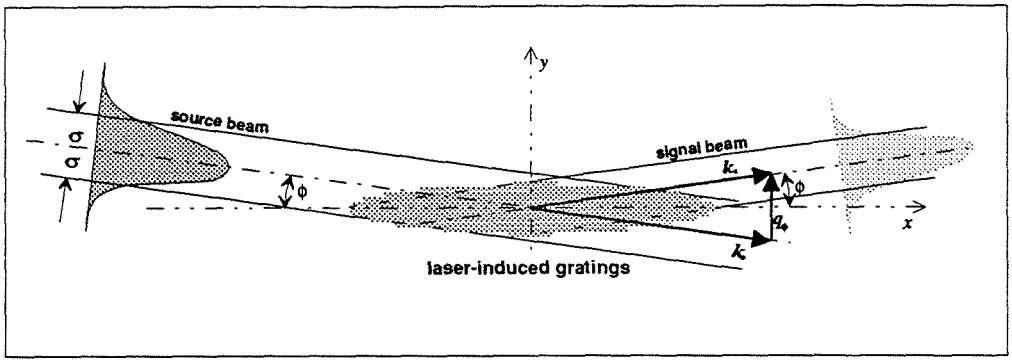

FIG. 3.2. Schematic diagram of the source and signal beam geometry. Note how the difference in wave vector from the source to the scattered beam is the grating (or phase-matching) vector q_ϕ

Two types of detection are considered: heterodyne, or phase-sensitive, detection that is required for velocimetry and homodyne detection, the more common technique. Special limiting cases are included. The complete expression for the homodyne LITA signal appears in Appendix B. The detector size, or detection angle, is found to have a profound impact on the time history of the signal. This detector effect helps to clarify the physical picture of LITA scattering and is analogous to the problem of the detection of quantum (wave)-mechanical interferences.

The results of the analysis include an expression for the time-history and absolute intensity of the detected LITA signal. This expression is experimentally validated in Chapter 11. An equally important result of the analysis is the clarification of the intuitive physical picture of LITA that leads to the correct inferences about the effects of finite beam and detector size. These results apply generally, not just to the assumed Gaussian-beam profiles.

CHAPTER 4

Solution of Linear Equations of Grating Evolution

LITA relies upon lasers to generate nonuniformities in a fluid. The generation and evolution of these nonuniformities modulate the LITA signal. The equations governing this evolution fall into two categories: the hydrodynamic conservation equations that describe the bulk behavior of fluids, including acoustics and heat transfer, and diffusion equations that describe "currents" internal to a bulk fluid caused by species-concentration gradients. Together with an equation of state of the fluid, these sets of equations close a system for describing fluid evolution from a general laser-induced state of perturbation. For brevity, the analysis presented here is completed only for the case in which species concentration gratings are negligible, which applies when the driver laser pulse is short compared to diffusive time-scales, photolysis does not occur in the fluid, and thermophoresis (Soret effect) is negligible. In this case, the field equations degenerate to the conservation equations of hydrodynamics. The equations which describe chemical diffusion are discussed and transformed into a system of algebraic equations. Together with the equations of hydrodynamics and an equation of state, these equations form a closed system that can be solved and manipulated completely analogously to the simplified derivation presented using only the equations of hydrodynamics.

4.1 Hydrodynamics

Hydrodynamics describes the motion of a continuous fluid. For fluids which are well approximated as continua, concepts such as diffusivities, densities, etc., can be defined. In this limit, the equations of conservation of mass (continuity), momentum, and energy describe the hydrodynamic evolution of disturbances in the fluid. If the disturbances are sufficiently small, as should apply to the perturbation gratings used in LITA, the hydrodynamics equations can be linearized. The linearized equations for the conservation of mass, momentum, and energy in terms of perturbations in density (ρ), temperature (T), and divergence of the velocity ($\psi \equiv \nabla \cdot \mathbf{u}$) in a Cartesian frame are (Mountain, 1966)

$$\frac{\partial \rho_1}{\partial t} + \rho \psi_1 = 0, \tag{4.1a}$$

$$\frac{\partial \psi_1}{\partial t} + \frac{c_s^2 \nabla^2 \rho_1}{\gamma \rho} + \frac{\alpha c_s^2}{\gamma} \nabla^2 T_1 - D_V \nabla^2 \psi_1 = \dot{\psi}(\mathbf{r}, t), \tag{4.1b}$$

$$\frac{\partial T_1}{\partial t} - \frac{\gamma - 1}{\alpha \rho} \frac{\partial \rho_1}{\partial t} - \gamma D_T \nabla^2 T_1 = \dot{T}(\mathbf{r}, t), \tag{4.1c}$$

where perturbation terms are indicated by the subscript '1', $\psi_1 \equiv \nabla \cdot \mathbf{u}_1$, and $\nabla^2 \equiv \partial^2/\partial x^2 + \partial^2/\partial y^2 + \partial^2/\partial z^2$. The parameter γ is the ratio of specific heats of the medium, α is the thermal expansion coefficient, $-(1/\rho)(\partial \rho/\partial T)_p$, c_s is the isentropic sound speed, D_V is the longitudinal kinematic viscosity, $1/\rho(\eta_v + (4/3)\eta_s)$, and D_T is the thermal diffusivity. The forcing terms, $\dot{\psi}$, and $\dot{T}$, describe the opto-acoustic effects. The boundary and initial conditions are

$$\rho_1(\mathbf{r}, t = 0) = 0; \qquad \psi_1(\mathbf{r}, t = 0) = 0; \qquad T_1(\mathbf{r}, t = 0) = 0, \tag{4.1d}$$

$$\rho_1(\mathbf{r}, t) \to 0; \qquad \psi_1(\mathbf{r}, t) \to 0; \qquad T_1(\mathbf{r}, t) \to 0, \quad \text{as} \quad |\mathbf{r}| \to \infty.$$

Strictly speaking, these equations apply to fluids with no mean velocity. However, they are good approximations in a moving inertial frame where the local apparent mean fluid velocity vanishes, provided that the local shear and rotation rates are negligible. Opto-acoustic forcing that rests in the laser frame moves relative to the fluid frame. Thus, the forcing terms account for the local velocity. The simplified analysis presented here ignores the effects of fluid motion. In the complete analysis, the effects of fluid motion are basically three-fold. Fluid motion across the electric-field grating that is comparable to the grating wavelength during the driver laser pulse

reduces the modulation depth of the grating and hence the LITA reflectivity. Grating convection across the source beam that is comparable to the source beam diameter over the lifetime of the acoustic grating changes the time history of the LITA signal by changing the source beam intensity on the grating. Finally, the driver, source, and signal beams have Doppler shifts and are nondegenerate in the fluid frame. The scattered field has a Doppler shift in the laser frame proportional to the laser-frame velocity of the grating. Optical heterodyne techniques recover this Doppler shift, permitting measurement of the cross-grating component of the gas velocity. The effects of fluid motion on experimental LITA signals is illustrated and discussed in Chapter 11.

Eqs. 4.1a–d may be solved by applying Fourier and Laplace transforms (Mountain, 1966; Cummings, 1994). The acousto-optic effect responsible for the LITA signal in gases arises predominantly from density perturbations, although thermal and velocity perturbations may also contribute to the signal. The solution for the perturbation fields is

$$\frac{\rho_1(\mathbf{q},s)}{\rho} = M(q,s)^{-1}\left[-c_s q\left(s+\gamma D_T q^2\right)\frac{\dot{\psi}}{c_s q} - \left(\frac{c_s^2 q^2}{\gamma}\right)\frac{\dot{T}}{T}\right], \tag{4.2a}$$

$$\frac{\psi_1(\mathbf{q},s)}{c_s q} = M(q,s)^{-1}\left[s\left(s+\gamma D_T q^2\right)\frac{\dot{\psi}}{c_s q} + \left(\frac{s c_s q}{\gamma}\right)\frac{\dot{T}}{T}\right], \tag{4.2b}$$

and

$$\frac{T_1(\mathbf{q},s)}{T} = M(q,s)^{-1}\left[-(\gamma-1)s\dot{\psi} + \left(s(s+q^2 D_V) + \frac{c_s^2 q^2}{\gamma}\right)\frac{\dot{T}}{T}\right], \tag{4.2c}$$

where perfect gas behavior has been assumed. The quantity $M(q,s)$ is the characteristic equation of the system of algebraic equations,

$$M(q,s) = s^3 + (D_V q^2 + \gamma D_T q^2)s^2 + (c_s^2 q^2 + \gamma D_T q^2 D_V q^2)s + c_s^2 q^2 D_T q^2. \tag{4.2d}$$

Factoring $M(q,s)$ facilitates Laplace inversion. To first order in the grating Knudsen number (ratio of the mean-free path to the grating wavelength), the roots of $M(q,s)$ are approximately (Berne et al., 1976)

$$s_1 = -D_T q^2; \qquad s_2 = -\Gamma q^2 + i c_s q, \qquad s_3 = -\Gamma q^2 - i c_s q, \tag{4.3}$$

where Γ is the classical acoustic damping coefficient, i.e., $\frac{1}{2}[(\gamma-1)D_T + D_V]$. The inclusion of higher-order terms in grating Knudsen number is unnecessary because the first-order analysis breaks down at about the same point as the hydrodynamic equations, which assume that scales of gradients of fluid properties are small compared to molecular mean-free paths. Thus the solution is valid for acoustic disturbances with characteristic dimensions much larger than the mean free path of the fluid. Otherwise, a molecular gas-dynamics model, e.g., the Chapman-Enskog or Boltzmann equations, may be needed. Chapter 11 contains illustrations and discussions of finite-Knudsen-number effects. This analysis also does not include the effects of scattering, or dephasing, of sound waves, which can be important, particularly near the critical point of a gas. These effects may be included in an *ad hoc* manner by incorporating the realties of linear scattering theory (see Appendix A.)

For brevity, consider only the evolution of density perturbations, ρ_1/ρ, since these typically produce the dominant scattering signal. A partial-fractions expansion of the solution in the approximate roots of $M(q,s)$ elucidates the fluid behavior,

$$\frac{\rho_1}{\rho} = \left[\frac{\dot{T}}{\gamma T} + \frac{(s+\gamma D_T q^2)}{c_s q}\frac{\dot{\psi}}{c_s q}\right]\frac{1}{[1+(\Delta-\mathrm{G})^2]} \times \left[\frac{1+i(\Delta-\mathrm{G})}{2(s+\Gamma q^2 - ic_s q)} + \frac{1-i(\Delta-\mathrm{G})}{2(s+\Gamma q^2+ic_s q)} - \frac{1}{(s+D_T q^2)}\right], \tag{4.4}$$

where $\Delta \equiv D_T q/c_s$ and $\mathrm{G} \equiv \Gamma q/c_s$ are, respectively, the fraction of the thermal and acoustic perturbations with a wave vector q that diffuse during the period of the wave. Typically, $\{\Delta, \mathrm{G}\} \ll 1$ for LITA performed at low grating Knudsen number. The three terms in the expansion correspond to three acoustic-scale structures that are generated opto-acoustically. The first two describe conjugate, spatially isentropic, density structures that decay at the classical acoustic damping rate and translate at the sound speed. These are referred to as acoustic wavepackets in this analysis, and can be envisioned as counter-propagating sound waves in the fluid. The third term describes a stationary, spatially isobaric density grating that decays by heat conduction. This structure is a perturbation in the temperature field. The formation and shape of the acoustic wavepacket and thermal grating depend upon the driving terms, $\dot{T}$ and $\dot{\psi}$. The physics of these results is discussed after expressions are derived for the opto-acoustic forcing terms, $\dot{T}$ and $\dot{\psi}$.

4.2 Species Diffusion

Laser-induced species concentration perturbations, which also evolve on hydrodynamic (diffusive) time scales, can contribute to the LITA signal, in which case it is necessary to examine the gas composition fields. Let the probed gas be a mixture of N types of molecules with molecular mass m_i, concentration n_i, and molecular susceptibility $\chi_i(\omega, \mathbf{n}, T)$, where ω is the optical frequency, $\mathbf{n}$ is the N-dimensional concentration vector with components n_i, and T is the temperature. The density (ρ) and pressure (p) of the mixture are,

$$\rho = \sum_{i=1}^{N} m_i n_i; \qquad p = \mathcal{R}T \sum_{i=1}^{N} n_i. \tag{4.5}$$

The evolution of the concentration field for each species obeys a diffusion equation coupled to that of every other species. The coupling arises from interactions between diffusing species, e.g., species with a net diffusion velocity in a particular direction will, on average, impart to other species momentum in that direction, hindering or assisting diffusion of the other species. There are $N-1$ such independent vector equations (the hydrodynamic momentum equation provides closure). These coupled equations may be expressed in terms of the partial pressures of the species, $p_i = n_i \mathcal{R}T$, (Chapman, 1970)

$$\sum_j \frac{1}{pD_{ij}} \left[p_i(\mathbf{r},t) \left(\frac{\partial p_j(\mathbf{r},t)}{\partial t} - \mathcal{R}T\dot{n}_j(\mathbf{r},t) \right) - p_j(\mathbf{r},t) \left(\frac{\partial p_i(\mathbf{r},t)}{\partial t} - \mathcal{R}T\dot{n}_i(\mathbf{r},t) \right) \right]$$

$$= \nabla^2[p_{e,i}(\mathbf{r},t) - p_i(\mathbf{r},t)] - \frac{m_i P_i}{n\mathcal{R}T} \sum_j \nabla^2[p_{e,j}(\mathbf{r},t) - p_j(\mathbf{r},t)], \tag{4.6}$$

where $D_{ij} = D_{ji}$ is the mutual diffusivity of Species i and j, $\dot{n}_i$ is a forcing term corresponding to a sink or source of Species i, and $p_{e,i}$ is a body-force term expressed as a pressure. The forcing terms are formulated in anticipation of the opto-acoustic effects of photolysis, which can create and destroy molecules of a particular species and photophoresis via electrostriction, which generates species-specific body-force fields. Thermophoresis may be included by adding a forcing term for the Soret effect to Eq. 4.6.‡ The mutual diffusivities D_{ij} depend only weakly on species concentration. The

‡ The Dufour effect may likewise be included by adding forcing terms to the energy equation (4.1c).

products pD_{ij} are roughly constant at constant temperature. Linearization of these equations enables solution by Fourier and Laplace transform. Express the partial-pressure fields in the sample volume as the sum of a constant term P_i and a time and space-dependent perturbation $p_i(\mathbf{r},t)$ (the subscript '1' convention is dropped here for clarity), then, retaining only first-order terms in the perturbations,

$$\sum_j \frac{1}{PD_{ij}} \left[P_i \left(\frac{\partial p_j(\mathbf{r},t)}{\partial t} - \mathcal{R}T\dot{n}_j(\mathbf{r},t) \right) - P_j \left(\frac{\partial p_i(\mathbf{r},t)}{\partial t} - \mathcal{R}T\dot{n}_i(\mathbf{r},t) \right) \right]$$
$$= \nabla^2[p_{e,i}(\mathbf{r},t) - p_i(\mathbf{r},t)] - \frac{m_i P_i}{n\mathcal{R}T} \sum_j \nabla^2[p_{e,j}(\mathbf{r},t) - p_j(\mathbf{r},t)]. \tag{4.7}$$

Even in this linear form, the mutual diffusion equations are complicated enough to inhibit interpretation. In special cases, the equations simplify. For a two-component gas with species X_1, which is undergoing forcing, Eqs. 4.7 reduce to

$$\frac{P_1}{P} \left(\frac{\partial p_2}{\partial t} \right) - \frac{p_2}{P} \left(\frac{\partial p_1}{\partial t} - \mathcal{R}T\dot{n}_1 \right) = D_{12} \left(\frac{\rho_2}{\rho} \nabla^2[p_{e,1} - p_1] - \frac{\rho_1}{\rho} \nabla^2[-p_2] \right), \tag{4.8}$$

where ρ_1 and ρ_2 are the densities of Species 1 and 2 (not to be confused with density perturbations). If Species 1 is a minor species, P_1/P and ρ_1/ρ are small. Eq. 4.8 for the concentration of X_1 becomes a regular, forced diffusion equation:

$$\frac{\partial n_1}{\partial t} - D_{12}\nabla^2 \left(n_1 - \frac{p_{e,1}}{\mathcal{R}T} \right) = \dot{n}_1, \tag{4.9}$$

which is expressed in terms of the number density to emphasize that molecules, not pressures, are diffusing.

Applying Laplace and Fourier transforms to Eqs. 4.7 yields $N-1$ independent algebraic vector equations:

$$\sum_j \frac{1}{PD_{ij}} \left[P_i \left[sp_j(\mathbf{q},s) - \mathcal{R}T\dot{n}_j(\mathbf{q},s) \right] - P_j \left[sp_i(\mathbf{q},s) - \mathcal{R}T\dot{n}_i(\mathbf{q},s) \right) \right]$$
$$= q^2 \left[(p_{e,i}(\mathbf{q},s) - p_i(\mathbf{q},s)) - \frac{m_i P_i}{n\mathcal{R}T} \sum_j (p_{e,j}(\mathbf{q},s) - p_j(\mathbf{q},s)) \right]. \tag{4.10}$$

Closure of the system requires the relations $p = \sum_i p_i$, the (linearized) equation of state, and Eqs. 4.1a–c. Calculating concentration fields is not generally necessary when driver laser durations are short compared to diffusive LITA time scales and photolysis does not occur. However, the framework has been developed here for the analysis of LITA signals from laser-induced concentration fields. The potential application of LITA to measure species-specific mutual diffusion coefficients is indicated.

CHAPTER 5
Modeling of Opto-Acoustic Forcing

In this thesis, any mechanism by which an optical electric field perturbs the macroscopic properties of a fluid is labeled an opto-acoustic effect. This definition is a generalization of the standard definition, since effects which produce perturbations with zero wave speed are included. Because the same physical mechanisms produce both types of waves, distinction between effects which produce propagating and non-propagating perturbations is not physically supported.

Two opto-acoustic effects have been observed in LITA, electrostriction and thermalization. Electrostriction using short driver pulses forces the momentum equation by impulsively accelerating gas molecules toward or away from regions of high optical electric field intensity, depending on the sign of the real part of the susceptibility. Thermalization, a conversion of electric-field to thermal energy, forces the energy equation. Other opto-acoustic effects that may prove to be important in LITA studies are photophoresis, the bulk migration of species or particles caused by an applied optical electric field and photolysis, light-induced chemical reactions. While LITA has not yet been performed using these effects, such experiments are planned since they should permit the measurement of species-specific mutual diffusion coefficients and other properties of interest, for example, in combustion modeling.

The forcing terms for the governing equations are fluid response operators acting on the driver laser fields. Evaluation of the operators involves modeling of the physical opto-acoustic interaction. In this analysis, the fluid response operators act upon narrowband Gaussian-profile driver beams. The assumed laser beam field is separable into the product of a spatial term and a temporal term. Only effects associated with the interference between the driver beams are pursued since only these contribute directly to the LITA signal. Non-interference terms, however, can indirectly modify the signal. For example, bulk heating of a gas by absorption raises the temperature and thus the sound speed.

Denote the electric fields of the two driver lasers $E_{d1}(x,y,z,t)$ and $E_{d2}(x,y,z,t)$, so that

$$E_{d1} = E_1 + E_1^*; \qquad E_{d2} = E_2 + E_2^*, \tag{5.1a}$$

where * denotes complex conjugation, and

$$\begin{aligned} E_1(x,y,z,t) &= \frac{\mathcal{E}(t)}{2}\sqrt{\frac{2}{\pi w^2}}\exp\left[-\frac{(y\cos\theta - x\sin\theta)^2 + z^2}{w^2}\right] \\ &\quad \times \exp i\left[\omega_d t - k_d(x\cos\theta + y\sin\theta)\right], \\ E_2(x,y,z,t) &= \frac{\mathcal{E}(t)}{2}\sqrt{\frac{2}{\pi w^2}}\exp\left[-\frac{(y\cos\theta + x\sin\theta)^2 + z^2}{w^2}\right] \\ &\quad \times \exp i\left[\omega_d t - k_d(x\cos\theta - y\sin\theta)\right], \end{aligned} \tag{5.1b}$$

where x, y, and z are coordinates of a Cartesian frame whose x-axis is the bisector of the two beams and y-axis is normal to the bisector in the plane of intersection (see Fig. 3.1). $\mathcal{E}(t)$ is the electric field envelope, ω_d is the driver laser frequency, k_d is the wave vector magnitude of the driver laser, θ is the beam-crossing half-angle, and w is the Gaussian half-width. The derivation in the next section requires the driver-beam intensity grating and its spatial Fourier transform. Defining the phase-matched scattering or grating vector, q_ϕ

$$q_\phi \equiv 2k_d \sin\theta, \tag{5.2a}$$

and the grating dimensions

$$\ell \equiv w/\sin\theta \qquad h \equiv w/\cos\theta, \tag{5.2b}$$

the expression for the electric field grating becomes

$$E_1^*(\mathbf{r},t)E_2(\mathbf{r},t) + E_2^*(\mathbf{r},t)E_1(\mathbf{r},t) = E_d I_d(\mathbf{r})P_d(t), \tag{5.2c}$$

where E_d is the total energy of the driver laser field, $P_d(t) = \mathcal{E}^2(t)/2E_d$ is the normalized driver laser intensity history, and $I_d(\mathbf{r})$ is the normalized grating intensity distribution,

$$I_d(\mathbf{r}) = \frac{2}{\pi w^2}\exp\left[-2\left(\frac{x^2}{\ell^2} + \frac{y^2}{h^2} + \frac{z^2}{w^2}\right)\right]\cos(q_\phi y). \tag{5.2d}$$

The spatial Fourier transform of $I_d(\mathbf{r})$ is

$$I_d(\mathbf{q}) = \frac{\sqrt{2\pi}\ell h}{4w}\exp\left(-\frac{\ell^2 q_x^2}{8} - \frac{w^2 q_z^2}{8}\right)\left[\exp\left(-\frac{h^2(q_y - q_\phi)^2}{8}\right) + \exp\left(-\frac{h^2(q_y + q_\phi)^2}{8}\right)\right]. \tag{5.3}$$

The interference grating is simply a Gaussian ellipsoid with a sinusoidal modulation in the y-direction. Its Fourier transform is a pair of Gaussian lobes centered on $q_y = \pm q_\phi$. The spacing of the lobes is proportional to the number of grating "fringes." The width of the lobes is inversely proportional to the diameter of the driver beams. The opto-acoustic effects generate susceptibility gratings that initially have the shape of the field intensity grating.

5.1 Electrostriction Model

Electrostriction is the tendency of polarizable molecules to move under the action of a potential field caused by the interaction of an optically induced dipole moment and the optical field (Boyd, 1992). The energy of a dipole in an electric field is $u(t) = -\epsilon_0 \mathbf{E}(t) \cdot \boldsymbol{\mu}_m(t)$, where $\mathbf{E}(t)$ is the instantaneous electric field vector, $\boldsymbol{\mu}_m(t)$ is the instantaneous molecular dipole moment, and ϵ_0 is the permitivity of empty space. A macroscopic ensemble average of this energy over a random distribution of dipole moments sums to zero. However, a macroscopic dipole moment, $\boldsymbol{\mu}$, may be induced by a second applied electric field (or the same field). If $\boldsymbol{\mu}$ and $\mathbf{E}$ are in phase, then the molecules experience a potential field proportional and opposite to the electric field amplitude. The gradient of this potential exerts a force on these molecules toward regions of high electric field. The opposite occurs when $\boldsymbol{\mu}$ and $\mathbf{E}$ are out of phase. In terms of the molecular susceptibility, χ_m, the electrostrictive energy density (per unit volume), U_e, to second order in field strength induced by an optical field $E(t)\cos(\omega t)$ with a slowly varying envelope $E(t)$ is

$$U_{e,m}(t) = -\mathrm{Re}\{\chi_m(\omega)\}\frac{\epsilon_0 E^2(t)}{2}, \tag{5.4}$$

where optical-frequency terms have been ignored. The subscript e denotes electrostriction. In a multi-species gas, the effective electrostrictive potential is proportional to the real part of the gas susceptibility,[‡] $\chi = (\epsilon/\epsilon_0 - 1)$, where ϵ is the local permitivity of the gas.

[‡] This result can be generalized for liquids with a large susceptibility using the well-known *Clausius-Mossotti* equation.

When Doppler shifts from fluid velocity are considered, the electrostrictive potential field experienced by a gas in a LITA experiment is proportional to the average of the real part of the gas susceptibility at the apparent frequencies of the two beams. Each driver beam induces a dipole moment oscillation on which the electric field of the other driver beam acts. Other effects are higher order in the driver fields.

The electrostrictive energy of a molecular species i acts like an electrostrictive partial pressure, $p_{e,i} = U_{e,i}$, on the evolution of the molecules. These electrostrictive partial pressures force diffusion of the species. The sum of these partial pressures is the electrostrictive pressure, $p_e(t) = U_e(t)$, that directly forces the momentum equation through the term $\dot{\psi}_e = \nabla^2 p_e/\rho$. Hence the electrostriction fluid response operator acting on the driver-beam interference pattern is

$$\dot{\psi}_e(\mathbf{r},t) = -\frac{\mathrm{Re}\{\chi(\omega_d)\}}{\rho}\nabla^2(E_d I_d(\mathbf{r})P_d(t)), \tag{5.5}$$

where $I_d = E_1^* E_2 + E_2^* E_1$, and $\mathbf{r}$ is the position vector. Taking the spatial Fourier transform and temporal Laplace transform of Eq. 5.5 provides the forcing term for Eqs. 4.4 and 4.1.b,

$$\dot{\psi}_e(\mathbf{q},s) = -\frac{\mathrm{Re}\{\chi(\omega_d)\}}{\rho}q^2 E_d I_d(\mathbf{q})P_d(s). \tag{5.6}$$

5.2 Thermalization Model

Thermalization describes the process by which driver laser energy is absorbed by fluid molecules and converted to thermal energy through inelastic collisions. A formal treatment of thermalization dynamics is complicated. The equations of evolution of excited-state populations could be considered governing equations for LITA, as they certainly are for DFWM and CARS. However, in LITA, it is unnecessary to model the energy transfer and excited-state populations provided the thermal energy addition rate is modeled accurately on LITA time scales. At atmospheric conditions, the dynamics of thermalization cannot be completely ignored because quenching of ordinary electronic states typically occurs over 0.1–100 ns, while typical Brillouin periods (LITA time scales) are of the order 10–100 ns. As collision rates increase, thermalization dynamics decrease in importance until the forcing may be treated as a delta function, with no resolvable temporal structure.

Second-order density-operator perturbation theory indicates that the rate of driver-laser-induced population of excited states is proportional to the negative imaginary part of the susceptibility, i.e., the linear absorption coefficient (Boyd, 1992). The overpopulation of the excited states is assumed to decay to the ground state by superelastic (thermalization) collisions at a rate γ_θ and by other processes at a rate $\gamma_{n\theta}$. The rate of thermal energy addition to the fluid is $\partial U_\theta/\partial t = \gamma_\theta U_{ex}$, where the subscript θ denotes thermalization. The excited-state energy density, U_{ex}, obeys the field equation

$$\frac{\partial U_{ex}}{\partial t} + \gamma_\theta U_{ex} + \gamma_{n\theta} U_{ex} - D_s \nabla^2 U_{ex} = -2k_d \mathrm{Im}\{\chi(\omega_d)\}\{E_d P_d(t) I_d(\mathbf{r})\}, \tag{5.7}$$

$$U_{ex}(\mathbf{r}, t = 0) = 0.$$

D_s is the diffusivity of excited-state molecules through the gas. The excited-state energy grating induced by narrow-bandwidth driver beams in a moving fluid is proportional to the absorption coefficient at the apparent frequencies of the driver beams. Physically, this means that the excited-state grating is being populated through the interaction of each driver beam with the macroscopic dipole moment induced by the other driver beam.

Taking the spatial Fourier transform and temporal Laplace transform of Eq. 5.7 and substituting the expression for U_θ provides

$$U_\theta(\mathbf{q}, s) = \frac{-2\gamma_\theta k_d \mathrm{Im}\{\chi(\omega_d)\} E_d I_d(\mathbf{q}) P(s)}{s(s + \gamma_{n\theta} + \gamma_\theta + D_s q^2)}. \tag{5.8}$$

The rate of temperature rise is $\dot{T}(\mathbf{q}, s) = sU_\theta(\mathbf{q}, s)/\rho c_v$, hence the fluid response operator for thermalization acting on the driver-beam interference pattern is

$$\dot{T}(\mathbf{q}, s) = \frac{-2\gamma_\theta k_d \mathrm{Im}\{\chi(\omega_d)\} E_d I_d(\mathbf{q}) P(s)}{\rho c_v (s + \gamma_{n\theta} + \gamma_\theta + D_s q^2)}. \tag{5.9}$$

More realistic thermalization models are simple to devise and incorporate by generalizing

$$\dot{T}(\mathbf{q}, s) = \frac{-2k_d \mathrm{Im}\{\chi(\omega_d)\} E_d I_d(\mathbf{q}) P_d(s) \Theta(q, s)}{\rho c_v}, \tag{5.10}$$

where $\Theta(q, s)$ models the energy transfer. However, the single-rate thermalization model elucidates the physics, matches actual behavior with reasonable accuracy, and serves as a basis for improved models (Cummings, 1993), e.g., $\Theta(q, s) \simeq \sum_i a_i \gamma_{\theta,i}(s + \gamma_{n\theta,i} + \gamma_{\theta,i} + D_{s,i} q^2)^{-1}$.

This physical modeling of opto-acoustic forcing is valid only if local collisional equilibration occurs on a time scale that is short compared to time scales of interest. This caveat is consistent with the requirement that the LITA grating Knudsen number be small, which is needed for the hydrodynamic equations 4.1a–c to be valid, and the quasi-continuum concepts of pressure, density, sound speed, and transport properties to be valid on the LITA length scale.

5.3 Photophoresis and Thermophoresis

Photophoresis describes light-induced bulk migration of chemical species or particles. Photophoresis can be caused by resonant electrostriction over a time scale that is comparable to that of molecular diffusion across a grating wavelength. This effect is differentiated here from electrostriction by the time scale of the process. What is called simply electrostriction in this context is the impulsive forcing of molecules in a pulsed optical electric field. The principal effect in simple electrostriction is the rapid addition of momentum to the bulk gas through equilibrating collisions. In photophoresis, the resonant molecules are repeatedly reaccelerated by the optical electric field after undergoing collisions. The species thus diffuse along gradients of the optical electric field intensity. Photophoresis can also be caused by thermalization through the Soret effect (Köhler, 1993), which is usually called thermophoresis. The evaluation of these effects requires the the treatment of species diffusion in addition to hydrodynamics, but requires no further opto-acoustic modeling. In particle-laden flows, particles can be accelerated in optical field intensity gradients by differential heating (Gomez et al., 1992). Over long time-scales, this acceleration also produces a photophoretic effect.

LITA using photophoresis may be used to measure molecular mutual diffusion and thermo-diffusion rates, which are of paramount importance in combustion dynamics. The author is not aware of any other non-intrusive, remote techniques for making these measurements. Experiments and study to evaluate the practicality of this technique are planned.*

---

* The major experimental obstacle is the need for a narrow-bandwidth, long-pulse driver laser for forming the species gratings.

5.4 Photolysis

LITA using photolysis to generate acoustic structures has not yet been reported, but could find interesting application in the future. The analysis of photolysis-induced structures is more complicated than that of either thermalization or electrostriction because photolysis in general forces the momentum, energy, and species concentration equations. These effects can be understood physically as follows. When a laser-induced chemical reaction occurs which changes the number of molecules, the pressure rises or falls according to Dalton's law of partial pressures, directly forcing the momentum equation. When the chemical potential of the products and reactants differ, the energy difference is transferred to the bulk gas through elastic collisions, forcing the energy equation. Photolysis directly forces the species diffusion equations by adding a species source term.

5.5 Derivation of Green's Functions for the Opto-Acoustic Response

Green's functions for the fluid response to electrostriction and thermalization are derived in this section. Photophoresis and photolysis may be similarly treated. Combining Eqs. 4.4, 5.6, and 5.9, we obtain an expression for the Fourier and Laplace transforms of the opto-acoustic density fields in terms of driver laser and fluid parameters

$$\frac{\rho_1(\mathbf{q},s)}{\rho} = I_d(\mathbf{q})P_d(s)E_d\left[\frac{-2k_d\gamma_\theta \mathrm{Im}\{\chi(\omega_d)\}}{\rho c_p T}\frac{1}{(s+\gamma_{n\theta}+\gamma_\theta+D_s q^2)} - \frac{\mathrm{Re}\{\chi(\omega_d)\}}{\rho c_s^2}(s+\gamma D_T q^2)\right]$$
$$\times\frac{1}{[1+(\Delta-\mathrm{G})^2]}\left[\frac{1+i(\Delta-\mathrm{G})}{2(s+\Gamma q^2-ic_s q)}+\frac{1+i(\Delta-\mathrm{G})}{2(s+\Gamma q^2+ic_s q)}-\frac{1}{(s+D_T q^2)}\right]. \tag{5.11}$$

Laplace inversion is aided by another partial fractions expansion. Define

$$\mathcal{U}_\theta = -\frac{2k_d\mathrm{Im}\{\chi(\omega_d)\}E_d}{w^2\rho c_p T}\frac{\gamma_\theta}{\gamma_{n\theta}+\gamma_\theta+D_s q^2}; \qquad \mathcal{U}_e = -\frac{q\mathrm{Re}\{\chi(\omega_d)\}E_d}{w^2\rho c_s^2}. \tag{5.12}$$

$\mathcal{U}_\theta$ and $\mathcal{U}_e$ may be considered the approximate modulation depths of the thermalization and electrostriction gratings, respectively. Let the symbol $\circ$ denote Laplace convolution, i.e.,

$$f(t)\circ g(t) \equiv \int_0^\infty f(\tau)g(t-\tau)\,d\tau. \tag{5.13}$$

The density field time-behavior is

$$\frac{\rho_1(\mathbf{q},t)}{\rho} = -w^2 I_d(\mathbf{q}) P_d(t) \circ \left[H_\theta(q,t)\mathcal{U}_\theta + H_e(q,t)\mathcal{U}_e\right]. \tag{5.14a}$$

Hence the temporal behavior of the opto-acoustic gratings is a convolution over the laser time history of H_θ and H_e, which may be regarded as Green's functions in time for the fluid response to thermalization and electrostriction respectively, given by

$$H_\theta(q,t) \equiv H_{\theta P}(q)\Phi_P(q,t) + H^*_{\theta P}(q)\Phi^*_P(q,t) + H_{\theta T}(q)\Phi_T(q,t) + H_{\theta D}(q)\Phi_D(q,t); \tag{5.14b}$$

$$H_e(q,t) \equiv H_{eP}(q)\Phi_P(q,t) + H^*_{eP}(q)\Phi^*_P(q,t) + H_{eT}(q)\Phi_T(q,t), \tag{5.14c}$$

where

$$\Phi_P(q,t) \equiv \exp(-\Gamma q^2 t + ic_s q t); \qquad \Phi_T(q,t) \equiv \exp(-D_T q^2 t);$$

$$\Phi_D(q,t) \equiv \exp(-(\gamma_\theta + \gamma_{n\theta})t - D_s q^2 t); \tag{5.14d}$$

$$H_{\theta P} \equiv \frac{[1+i(\Delta-\mathrm{G})][1-\mathrm{G}\Pi - i\Pi]}{2[1+(\Delta-\mathrm{G})^2][(1-\mathrm{G}\Pi)^2+\Pi^2]}; \qquad H_{\theta T} \equiv \frac{-1}{[1+(\Delta-\mathrm{G})^2][1-\Delta\Pi]};$$

$$H_{\theta D} \equiv \frac{\Pi^2}{[(1-\mathrm{G}\Pi)^2+\Pi^2][1-\Delta\Pi]}; \tag{5.14e}$$

$$H_{eP} \equiv i\frac{[1-i(\gamma\Delta-\mathrm{G})][1+i(\Delta-\mathrm{G})]}{2[1+(\Delta-\mathrm{G})^2]}; \qquad H_{eT} \equiv \frac{(\gamma-1)\Delta}{[1+(\Delta-\mathrm{G})^2]}, \tag{5.14f}$$

and

$$\Pi \equiv c_s q/(\gamma_\theta + \gamma_{n\theta} + D_s q^2). \tag{5.14g}$$

The parameter Π is the ratio of the frequency of sound waves with wave vector q to the excited-state energy decay rate. Π should be small for efficient acoustic-wave formation. In the limit of fast thermalization and negligible damping over a wave period, the parameters $H_{\theta_P} \to 1/2$, $H_{\theta_T} \to -1$, $H_{\theta_D} \to 1$, $H_{eP} \to i/2$, and $H_{eT} \to 0$. At atmospheric conditions, Δ and $\Gamma \sim 0.4/\lambda_g$, where λ_g is the grating wavelength expressed in μm; hence for typical grating spacings of 5–50 μm, these parameters are negligible. Under the same conditions, $\Pi \sim 2/\lambda_g$–$50/\lambda_g$, depending upon the quenching rates of the excited state, and therefore may not be negligible.

5.6 Solution for Density Perturbation Field

The Fourier transform of the driver grating, $I_d(\mathbf{q})$, is strongly peaked at $\mathbf{q} = q_\phi \hat{\mathbf{e}}_y$, where $\hat{\mathbf{e}}_y$ is the unit vector in the q_y-direction. Assume therefore that the coefficients of the elements $H_{\theta\{P,T,D\}}$ and $H_{e\{P,T\}}$ are equal to their values at $q = q_\phi$. This assumption becomes worse as the number of grating fringes decreases. Also, to second order in q/q_ϕ, approximate that $q \simeq q_y + (q_x^2 + q_z^2)/2q_\phi$. This assumption ignores higher-order effects in the diffraction of the acoustic gratings, such as the curvature of the phase fronts, which invalidates this model when the acoustic gratings have propagated far from their point of formation. The inverse Fourier transforms of the products $I_d(\mathbf{q})\Phi_{\{P,T,D\}}(q,t) \equiv \Phi^{(d)}_{\{P,T,D\}}$ are, without further approximation,

$$\Phi_P^{(d)}(\mathbf{r}) = \frac{2\ell h}{\pi w \Lambda_P \Omega_P \mathrm{H}_P} \exp\left[-2\frac{x^2}{\Lambda_P^2} - 2\frac{z^2}{\Omega_P^2} - 2\frac{(y+c_s t)^2}{\mathrm{H}_P^2}\Gamma q_\phi^2 t \eta_P^2\right] \cos\left[(y+c_s t) q_\phi \eta_P^2\right], \quad (5.15a)$$

$$\Phi_{P^*}^{(d)}(\mathbf{r}) = \frac{2\ell h}{\pi w \Lambda_P^* \Omega_P^* \mathrm{H}_P} \exp\left[-2\frac{x^2}{\Lambda_P^{*2}} - 2\frac{z^2}{\Omega_P^{*2}} - 2\frac{(y-c_s t)^2}{\mathrm{H}_P^2}\Gamma q_\phi^2 t \eta_P^2\right] \cos\left[(y-c_s t) q_\phi \eta_P^2\right], \quad (5.15b)$$

$$\Phi_T^{(d)}(\mathbf{r}) = \frac{2\ell h}{\pi w \Lambda_T \Omega_T \mathrm{H}_T} \exp\left[-2\frac{x^2}{\Lambda_T^2} - 2\frac{y^2}{\mathrm{H}_T^2} - 2\frac{z^2}{\Omega_T^2} - D_T q_\phi^2 t \eta_T^2\right] \cos(y q_\phi \eta_T^2), \text{ and} \quad (5.15c)$$

$$\Phi_D^{(d)}(\mathbf{r}) = \frac{2\ell h}{\pi w \Lambda_D \Omega_D \mathrm{H}_D} \exp\left[-2\frac{x^2}{\Lambda_D^2} - 2\frac{y^2}{\mathrm{H}_D^2} - 2\frac{z^2}{\Omega_D^2} - D_s q_\phi^2 t \eta_D^2 - (\gamma_\theta + \gamma_{n\theta})t\right] \cos(y q_\phi \eta_D^2), \quad (5.15d)$$

where**

$$\Lambda_P^2 \equiv \ell^2 + 8\Gamma t - 4ic_s t/q_\phi; \quad \Lambda_T^2 \equiv \ell^2 + 8D_T t; \quad \Lambda_D^2 \equiv \ell^2 + 8D_s t;$$

$$\mathrm{H}_P^2 \equiv h^2 + 8\Gamma t; \quad \mathrm{H}_T^2 \equiv h^2 + 8D_T t; \quad \mathrm{H}_D^2 \equiv h^2 + 8D_s t;$$

$$\Omega_P^2 \equiv w^2 + 8\Gamma t - 4ic_s t/q_\phi; \quad \Omega_T^2 \equiv w^2 + 8D_T t; \quad \Omega_D^2 \equiv w^2 + 8D_s t;$$

$$\eta_P \equiv h/\mathrm{H}_P; \qquad \eta_T \equiv h/\mathrm{H}_T; \qquad \eta_D \equiv h/\mathrm{H}_D. \quad (5.15e)$$

This relatively complicated nomenclature results from allowing all the dimensions of each grating to change at different rates. Note that, except for gratings with very few fringes, the LITA signals will decay before these new length-scales depart significantly from their values at $t = 0$, with one exception, Ω_P, for which the imaginary part increases relative to the real part at a rate c_s/w. Thus, normally, the spreading of the grating envelope by diffusion may be ignored but the wave motion may not.

** Be careful to avoid confusion between capital Greek *eta* defined here for the length scales, $\mathrm{H}_{\{P,T,D\}}$, and the capital H's used elsewhere!

CHAPTER 6

Discussion of Grating Formation and Evolution

The results of the derivation of expressions for the creation and evolution of acoustic gratings by electrostriction and thermalization bear discussion. The creation and evolution of the gratings may be understood simply by first considering the situation in which the opto-acoustic driving occurs instantly. Consider the properties of the fluid across the grating at cross-section A—A in Fig. 6.1, at time $t = 0$, immediately after driving using a delta-function laser pulse. If thermalization occurs instantly, the temperature perturbation follows the electric field intensity grating. However, at time $t = 0$, there has been no bulk displacement of the gas, thus no density grating exists. The gas is in a nonequilibrium state since at equilibrium the density is inversely proportional to temperature. The response of the gas may be explained in terms of the production of thermal gratings and acoustic wavepackets. The flat density profile at $t = 0$ is the superposition of the equilibrium density field borne by the thermal grating and two opposing density fields borne by two conjugate acoustic wavepackets. At $t = 0$, the field of the acoustic wavepackets cancels the field of the thermal grating. At $t > 0$, the motion of the acoustic wavepackets modulates the density field as the waves alternately interfere constructively and destructively with the thermal grating. The frequency of the density field modulation, the "Brillouin" frequency ω_B, is $\omega_B = c_s q_\phi$. As the acoustic waves propagate, they decay by diffusion at the acoustic damping rate. The thermal grating decays by thermal diffusion. The assumption of linear hydrodynamic behavior eliminates a variety of effects which could affect signals in real experiments. For example, the thermal grating will perturb the local sound speed, causing coupling between the acoustic waves and thermal grating. Limiting the modulation depth of the grating suitably, e.g., $< 1\%$, mitigates nonlinear effects.

Instantaneous electrostriction impulsively accelerates the target molecules toward or away from regions of high electric field. By (assumed instantaneous) local equilibration of molecular velocities, the target molecules transfer momentum to the bulk

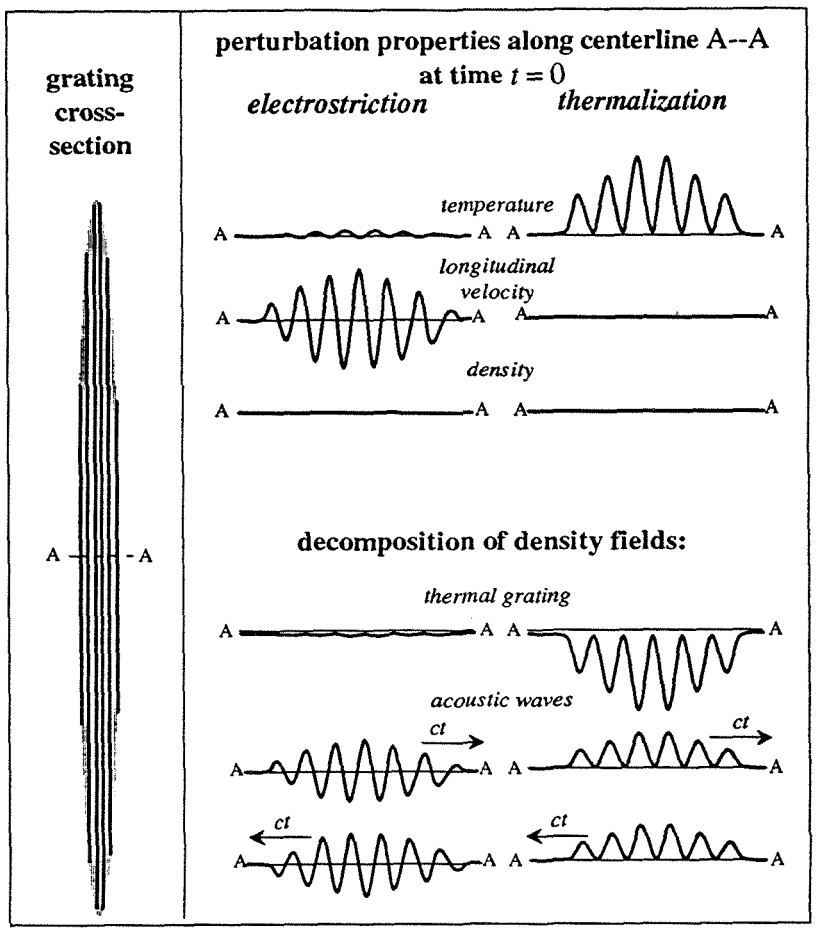

FIG. 6.1. Optoacoustic generation of acoustic wave packets and thermal gratings. At time $t = 0$ the density fields of the acoustic wavepackets and thermal grating sum to zero. Afterward, motion of the waves and damping modulates the density grating amplitude.

gas, creating a velocity grating. The velocity grating induces density gratings. Again the density fields sum to zero at $t = 0$. In electrostriction, the acoustic waves typically dominate over the thermal grating. Furthermore, these acoustic waves are $\pm 90°$ out of phase with the waves generated by thermalization. The temporal modulation of the density field occurs primarily at twice the Brillouin frequency.

When driving time scales are comparable to the hydrodynamic scales, the response is more complicated than in the limiting case presented in Fig. 6.1. First, the temporal behavior of the acoustic gratings is convolved with the driver-laser time history, which effectively smears the acoustic waves and steepens the thermal grating (over the freely diffusing profile). Second, thermalization introduces another temporal convolution. In the current model, the convolution kernel is a simple exponential decay. For more

realistic models, the convolution is over a more complicated kernel. Convolution over the thermalization also smears the acoustic waves. For efficient wave formation, driver-laser durations and thermalization times must be short compared to the inverse of the Brillouin frequency. If thermalization rates are sufficiently fast, the acoustic and thermal structures become independent of the details of the thermalization behavior, simplifying the analysis of LITA signals.

At atmospheric pressure, collision rates per molecule are $\sim 10^9$ - 10^{10}/s. If the ambient gas quenches the excited state of the target species reasonably well, the smallest expected thermalization times are ~1 - 20 ns. The largest practical grating spacings are ~30 μm, yielding a period of motion across a grating wavelength of ~100 ns in room-temperature air. Thus at STP, finite thermalization rates may be important contributors to the LITA signal and must be treated. The finite-thermalization-rate model in Sec. 5.2 used in this analysis has been adequate for quantifying the experimental data presented in Chapter 11, although multi-rate thermalization behavior was observed at low pressures. In some situations, more realistic modeling is required (Paul et al., 1995).

The modeling of the response of the fluid to the driver beams is tractable because approximations have been made regarding the molecular and intramolecular gas behavior. Several of these approximations have already been discussed, e.g., simplified thermalization modeling. There is an additional series of approximations that is applied when the equations of hydrodynamics are used to treat a mixture of pure gases or a pure gas whose molecules are in a mixture of energy states. Diffusivities of a class of molecules have temperature, collision-partner, and energy-state dependence. The use of an average diffusivity for a mixture of gases in predicting the macroscopic behavior of gases generally ignores these details. In many situations, this degree of approximation is warranted. In the analysis of LITA signals, such details may need to be examined. For example, the molecular diffusivity of the excited-state of the resonant species appears in Eq. 5.7, which describes the evolution of the excited-state energy through the gas. In gas mixtures, thermal gradients can induce species concentration gradients and vice versa through the Soret and Dufour effects, respectively. These effects are enhanced when there are large differences in the molecular masses of the

component species and are often ignored even in the analysis of combustion, which can depend sensitively on such effects. The effects on the LITA signal and the evolution of the laser-induced gratings may be important. A Soret-effect (thermophoretically) induced concentration grating of a species that is resonant with the source laser can directly modify the LITA signal, since such gratings can produce enhanced acousto-optical effects (discussed in the next chapter). In the tests that were conducted at GALCIT, the concentration of resonant species was low enough that the effect on the signals was always negligible. However, this effect may be important in tests using relatively large concentrations of resonant species (e.g., ~parts-per-thousand), gases with weak nonresonant susceptibility, and resonant species with molecular mass that is vastly different from that of the buffer gas. The effect on nonresonant species may also be important, since it may influence the diffusion process and indirectly modify the LITA signal. If thermophoresis is suspected to have an important effect on the LITA signal, the equations of species diffusion must be included in the analysis of the laser-induced grating behavior.

CHAPTER 7

Modeling of Linear Acousto-Optical Scattering

Light is scattered by nonuniformities of a gas. Rayleigh and Brillouin scattering arise from statistical isobaric and isentropic fluctuations of the gas density, respectively, as discussed in Chapter 2. These scattering processes are weak because the fluctuations are incoherent. The acousto-optic effects that create the LITA signal beam are the same as those of the linear scattering phenomena (except for scattering caused by species concentration gratings). However, LITA scattering may be many orders of magnitude stronger than Rayleigh or Brillouin scattering because the "fluctuations" are coherent (Cummings, 1992, 1994). This coherent enhancement of the LITA signal over classical linear scattering techniques does not change the *spectrum* of the scattered light, but only the *intensity*. The spectrum of the LITA signal scattered from a broadband laser off a density grating is the same as the Rayleigh/Brillouin spectrum of the gas in the sample volume (except with extremely broadband source lasers, for which phase-matching becomes a concern). Hence the LITA reflectivity spectrum is far less complicated than those of most other nonlinear optical techniques. The simple reflectivity spectrum motivates the use of LITA for multiplex spectral measurements.

Acousto-optics used in LITA may be treated using the linearized equation of light scattering. In the far-field, the optical electric field E_s scattered by a small disturbance in the (isotropic) susceptibility $\chi_1(\mathbf{r},t;\omega)$ from a narrowband source beam $E_o(\mathbf{r},t)\cos(\omega_o t)$, with a slowly varying envelope, is (from Appendix A)

$$E_s(\mathbf{R},t;\mathbf{q}) = -\frac{k_s^2}{4\pi R}\cos(\mathbf{k}_s\cdot\mathbf{R}-\omega_o t)\mu_s(\mathbf{q},t), \tag{7.1a}$$

where $\mathbf{q}$ is the change in wave vector from the source to the scattered beam, $\mathbf{k}_s$ is the wave vector of the scattered beam ($|k_s|\simeq|k_o|$), $\mathbf{R}$ is the position vector relative to the scatterer, and $\mu_s(\mathbf{q},t)$ is the spatial Fourier transform of the scattering dipole moment density, $\mu_s(\mathbf{r},t)$, of the susceptibility grating and the source laser field, i.e.,

$$\mu_s(\mathbf{r},t) = \chi_1(\mathbf{r},t;\omega_o)E_o(\mathbf{r},t). \tag{7.1b}$$

The change in gas susceptibility caused by the opto-acoustic effects comes from a combination of the change in density, temperature, and species concentration. The dependence of the susceptibility on density changes is usually the strongest acousto-optic effect treated for gases and is the only effect treated in this analysis. The gas susceptibility is roughly linear with density for small density perturbations, $\chi_1 \simeq \chi\rho_1/\rho$. Thus, the scattered field E_s is known in terms of the density perturbation field, the source laser profile, and the linear susceptibility at the source laser frequency.

For this simple analysis, consider a narrowband, Gaussian source beam with half-width σ, negligible divergence, and center frequency ω_o, coplanar with the driver lasers and incident on the sample volume at the phase-matched angle, ϕ. Furthermore, assume the source beam is perfectly centered on the sample volume, as shown in Fig. 3.2. Denote $\sigma_x \equiv \sigma/\sin\phi$ and $\sigma_y \equiv \sigma/\cos\phi$. The electric field of the source beam is then $E_o(\mathbf{r},t) = P_o(t)I_o(\mathbf{r})\cos(\omega_o t)$, where

$$I_o = \sqrt{\frac{2}{\pi\sigma^2}}\exp\left[-\left(\frac{y}{\sigma_y}-\frac{x}{\sigma_x}\right)^2-\frac{z}{\sigma}\right]. \tag{7.2}$$

I_o is normalized so that the instantaneous power of the source laser is $P_o^2(t)$. Define $\Phi^{(d,o)}_{\{P,T,D\}}(\mathbf{r},t) \equiv I_o(\mathbf{r})\Phi^{(d)}_{\{P,T,D\}}(\mathbf{r},t)$, the field of the overlap of the source beam and the subscripted acoustic structures. The Fourier transforms of $\Phi^{(d,o)}_{\{P,T,D\}}$ dictate the LITA scattering lobe shapes and time dependence. The component of the scattering vector q_x is assumed to be zero for all scattered light. The Fourier transform in x becomes the integral of $\Phi^{(d,o)}_{\{P,T,D\}}(\mathbf{r},t)$ over x. The overlap length of the source beam and grating in the x-direction is typically $\sim 10-30$ times that in the y- and z- directions. Hence the finite-size effects in the x-direction may be safely ignored. This is accomplished by letting $\sigma_x \to \infty$. Performing the integration and the transforms over y and z, in this limit, and ignoring the contribution from the lobe at $q_y = -q_\phi$, one obtains

$$\Phi_P^{(d,o)}(\mathbf{q}) = N_P\Psi_P(\mathbf{q})\Sigma_P(t); \qquad \Phi_T^{(d,o)} = N_T\Psi_T(\mathbf{q})\Sigma_T(t); \qquad \Phi_D^{(d,o)} = N_D\Psi_D(\mathbf{q})\Sigma_D(t); \tag{7.3a}$$

where

$$N_P \equiv \frac{\sqrt{\pi\xi_P\zeta_P}\ell h}{w\sigma \mathrm{H}_P\Omega_P}; \qquad N_T \equiv \frac{\sqrt{\pi\xi_T\zeta_T}\ell h}{w\sigma \mathrm{H}_T\Omega_T}; \qquad N_D \equiv \frac{\sqrt{\pi\xi_D\zeta_D}\ell h}{w\sigma \mathrm{H}_D\Omega_D}; \tag{7.3b}$$

$$\Psi_P \equiv \sqrt{\frac{\xi_P\zeta_P}{4\pi}}\exp\left(-\frac{\xi_P^2 q'^2_{yP}}{8}-\frac{\zeta_P^2 q_z^2}{8}+\frac{\xi_P^2}{\mathrm{H}_P^2}ic_s q'_{yP}t\right);$$

$$\Psi_T \equiv \sqrt{\frac{\xi_T \zeta_T}{8\pi}} \exp\left(-\frac{\xi_T^2 q'^2_{yT}}{8} - \frac{\zeta_T^2 q_z^2}{8}\right); \tag{7.3c}$$

$$\Psi_D \equiv \sqrt{\frac{\xi_D \zeta_D}{8\pi}} \exp\left(-\frac{\xi_D^2 q'^2_{yD}}{8} - \frac{\zeta_D^2 q_z^2}{8}\right);$$

$$\Sigma_P \equiv \exp\left(-\frac{2c_s^2 t^2}{H_P^2 + 2\sigma_y^2} - \Gamma q_\phi^2 t \eta_P^2 + i q_\phi c_s t \eta_P^2\right); \qquad \Sigma_T \equiv \exp\left(-D_T q_\phi^2 t \eta_T^2\right);$$

$$\Sigma_D \equiv \exp\left(-D_s q_\phi^2 t \eta_D^2 - (\gamma_\theta + \gamma_{n\theta})t\right); \tag{7.3d}$$

where $q'_{y\{P,T,D\}} \equiv q_y - q_\phi \eta^2_{\{P,T,D\}}$ and

$$\xi_{\{P,T,D\}} \equiv \left(\frac{1}{H^2_{\{P,T,D\}}} + \frac{1}{2\sigma_y^2}\right)^{-\frac{1}{2}}; \qquad \zeta_{\{P,T,D\}} \equiv \left(\frac{1}{\Omega^2_{\{P,T,D\}}} + \frac{1}{2\sigma^2}\right)^{-\frac{1}{2}} \tag{7.3e}$$

are overlap length scales in the y- and z-directions.

Substituting these expressions into Eq. 7.1a provides the scattered field of the LITA signal, i.e.,

$$\frac{E_s(\mathbf{q}, R, t)}{P_o(t)} = -\frac{k_s^2 w^2}{4\pi R} \chi(\omega_o) \exp i(\mathbf{k}_s \cdot \mathbf{R} - \omega_o t) P_d(t)$$
$$\circ \Big[2\mathrm{Re}\{\Phi_P^{(d,o)}(\mathbf{q}, t)[\mathcal{U}_\theta H_{\theta P} + \mathcal{U}_e H_{eP}]\}$$
$$+ \Phi_T^{(d,o)}(\mathbf{q}, t)[\mathcal{U}_\theta H_{\theta T} + \mathcal{U}_e H_{eT}] + \Phi_D^{(d,o)}(\mathbf{q}, t)\mathcal{U}_\theta H_{\theta D}\Big]. \tag{7.4}$$

CHAPTER 8

Integration to Obtain the LITA Signal

The LITA signal obtained using heterodyne detection is equal to the integral of the field (Eq. 7.4) over the detection angle (a range of q_y' and q_z centered on zero). If this range is infinitesimal, the detected signal is given by Eq. 7.4. If the detection angle is larger than the lobe size (large detector limit), these integrals may be approximated by infinite integrals, giving the result for $\mathcal{L}_{het}$, the heterodyne LITA signal

$$\begin{aligned}\frac{\mathcal{L}_{het}}{P_o(t)} =& \sqrt{\pi}\frac{\ell h}{w\sigma}\chi(\omega_o)\frac{k_o^2 w^2}{4\pi}\exp(-i\omega_o t)P_d(t) \\ & \circ\left[\mathrm{Re}\left\{\frac{\sqrt{\xi_P\zeta_P}}{\mathrm{H}_P\Omega_P}\exp\left(-\frac{2c_s^2t^2}{\mathrm{H}_P^2}-\Gamma q_\phi^2 t\eta_P^2+iq_\phi c_s t\eta_P^2\right)\left[\mathcal{U}_\theta H_{\theta P}+\mathcal{U}_e H_{eP}\right]\right\}\right. \\ & +\frac{\sqrt{\xi_T\zeta_T}}{\mathrm{H}_T\Omega_T}\exp\left(-D_T q_\phi^2 t\eta_T^2\right)\left[\mathcal{U}_\theta H_{\theta T}+\mathcal{U}_e H_{eT}\right] \\ & \left.+\frac{\sqrt{\xi_D\zeta_D}}{\mathrm{H}_D\Omega_D}\exp\left[-D_s q_\phi^2 t\eta_D^2-(\gamma_\theta+\gamma_{n\theta})t\right]\mathcal{U}_\theta H_{\theta D}\right], \end{aligned} \tag{8.1}$$

where k_s has been assumed equal to k_o. Note the interesting result that the signal from the acoustic waves drops as $\exp(-(c_s t/\mathrm{H}_P)^2)$ as the waves propagate. The waves behave as if they scatter light onto the large, phase-sensitive detector only while they overlap. A physical interpretation is that light scattered by the waves is out of phase when they do not overlap, canceling the signal observed on the detector. When the detector size is small in comparison to the scattering lobe size, the light scattered by the waves adds up in phase over the entire source beam, regardless of whether the waves overlap. The physical picture that provides the most insight into the signal scattered by the acoustic waves is different in both limits. In the large-detector limit, the notion that the waves scatter light only when they overlap, thus creating an oscillatory standing-wave pattern, leads to the proper conclusions about the envelope of the signal. In the small-detector limit, the envelope of the signal scattered by the waves appears to be Doppler beats between light scattered by independent moving gratings. Because many of the potential applications of LITA involve interpreting the time-resolved signal, it is important to be aware of these detector effects.

In homodyne experiments, the detected signal is the integral of the square of the modulus of the scattered field over the detection angle. Define the amplitudes of the acoustic waves, thermal grating, and the finite-driving-time terms

$$A_P \equiv \mathcal{U}_\theta H_{\theta P} + \mathcal{U}_e H_{eP}; \qquad A_T \equiv \mathcal{U}_\theta H_{\theta T} + \mathcal{U}_e H_{eT}; \qquad A_D \equiv \mathcal{U}_\theta H_{\theta D}. \tag{8.2}$$

If the detector is larger than the signal beam size, these integrals may be approximated by infinite integrals over q_y' and q_z. The element of area of the detector is $dy\,dz = (R^2/(k_o \cos\phi)^2 dq_y\, dq_z$. The result of this integration appears in Appendix B.

The complete expression for the LITA signal, Eq. B.1 in Appendix B, involves a two-dimensional convolution over the driver laser temporal profile. In many situations, the duration of the driver beams is short enough that the effect of the finite driving can be treated approximately, significantly speeding the calculation of the signal. If $P_d(t)$ is short compared to the inverse of the Brillouin frequency, then $P_d(t) \sim \delta(t)$, where $\delta(t)$ is the Dirac delta function. This approximation may be used to eliminate one or both temporal convolutions. Most of the experimental data that appears in Chapter 11 was fit be the use of the approximate expression with one integration eliminated rather than Eq. B.1, i.e.,

$$\begin{aligned}
\frac{\mathcal{L}_{hom}}{P_o^2(t)} = {} & \frac{k_o^2 w^4}{16\pi^2 \cos^2\phi} |\chi(\omega_o)|^2 \int_0^\infty P_d(t-\tau) \\
\times \Bigg[\mathrm{Re} \Bigg\{ & 2A_P^2 N_P(\tau) N_P(t) \sqrt{\frac{4\zeta_P(\tau)\xi_P(\tau)\zeta_P(t)\xi_P(t)}{(\xi_P^2(\tau)+\xi_P^2(t))\,(\zeta_P^2(\tau)+\zeta_P^2(t))}} \\
& \times \exp\left(-2c_s^2 \left[\frac{\tau^2 \xi_P^2(\tau)}{\mathbf{H}_P^4(\tau)} + \frac{t^2 \xi_P^2(t)}{\mathbf{H}_P^4(t)}\right]\right) \Sigma_P(\tau)\Sigma_P(t) \\
& + 4A_P A_T N_P(\tau) N_T(t) \sqrt{\frac{4\zeta_P(\tau)\xi_P(\tau)\zeta_T(t)\xi_T(t)}{(\xi_P^2(\tau)+\xi_T^2(t))\,(\zeta_P^2(\tau)+\zeta_T^2(t))}} \\
& \times \exp\left(\frac{-2\xi_P^4(\tau) c_s^2 \tau^2}{\mathbf{H}_P^4(\tau)(\xi_P^2(\tau)+\xi_T^2(t))}\right) \Sigma_P(\tau)\Sigma_T(t) \\
& + 4A_P A_D N_P(\tau) N_D(t) \sqrt{\frac{4\zeta_P(\tau)\xi_P(\tau)\zeta_D(t)\xi_D(t)}{(\xi_P^2(\tau)+\xi_D^2(t))\,(\zeta_P^2(\tau)+\zeta_D^2(t))}} \\
& \times \exp\left(\frac{-2\xi_P^4(\tau) c_s^2 \tau^2}{\mathbf{H}_P^4(\tau)(\xi_P^2(\tau)+\xi_D^2(t))}\right) \Sigma_P(\tau)\Sigma_D(t) \Bigg\} \\
& + 2A_P A_P^* N_P(\tau) N_P^*(t) \sqrt{\frac{4\zeta_P(\tau)\xi_P(\tau)\zeta_P(t)\xi_P(t)}{(\xi_P^2(\tau)+\xi_P^2(t))\,(\zeta_P^2(\tau)+\zeta_P^2(t))}} \Sigma_P(\tau)\Sigma_P^*(t)
\end{aligned}$$

$$+2A_TA_DN_T(\tau)N_D(t)\sqrt{\frac{4\zeta_T(\tau)\xi_T(\tau)\zeta_D(t)\xi_D(t)}{(\xi_T^2(\tau)+\xi_D^2(t))\,(\zeta_T^2(\tau)+\zeta_D^2(t))}}\Sigma_T(\tau)\Sigma_D(t)$$

$$+A_T^2N_T(\tau)N_T(t)\sqrt{\frac{4\zeta_T(\tau)\xi_T(\tau)\zeta_T(t)\xi_T(t)}{(\xi_T^2(\tau)+\xi_T^2(t))\,(\zeta_T^2(\tau)+\zeta_T^2(t))}}\Sigma_T(\tau)\Sigma_T(t)$$

$$+A_D^2N_D(\tau)N_D(t)\sqrt{\frac{4\zeta_D(\tau)\xi_D(\tau)\zeta_D(t)\xi_D(t)}{(\xi_D^2(\tau)+\xi_D^2(t))\,(\zeta_D^2(\tau)+\zeta_D^2(t))}}\Sigma_D(\tau)\Sigma_D(t)\Bigg]\,d\tau \qquad (8.3)$$

The complete result may be simplified in most instances by ignoring the change in length scales due to diffusion, but not wave motion. For notational convenience, the driver laser is regarded as a delta function in time, eliminating both convolutions. The complete expression, Eq. B.1, simplifies to

$$\frac{\mathcal{L}_{hom}}{P_o^2(t)} = \frac{\pi}{4}\frac{\ell^2}{\lambda_o^2}|\chi(\omega_o)|^2\frac{\xi\zeta}{\sigma^2\cos^2\phi\cos^2\theta}$$

$$\Bigg[\mathrm{Re}\Bigg\{2A_P^2\left(\frac{w^2\zeta_P}{\Omega_P^2\zeta}\right)\exp\left(-\frac{4c_s^2t^2}{h^2+2\sigma_y^2}-2\Gamma q_\phi^2t+2iq_\phi c_st\right)\exp\left(\frac{-4\xi^2c_s^2t^2}{h^4}\right)$$

$$+4A_PA_T\sqrt{\left(\frac{2\zeta_P^2}{\zeta_P^2+\zeta^2}\right)}\frac{w}{\Omega_P}\exp\left(-\frac{2c_s^2t^2}{h^2+2\sigma_y^2}-(D_T+\Gamma)q_\phi^2t+iq_\phi c_st\right)\exp\left(\frac{-\xi^2c_s^2t^2}{h^4}\right)$$

$$+4A_PA_D\sqrt{\left(\frac{2\zeta_P^2}{\zeta_P^2+\zeta^2}\right)}\frac{w}{\Omega_P}\exp\left(-\frac{2c_s^2t^2}{h^2+2\sigma_y^2}-(D_s+\Gamma)q_\phi^2t+iq_\phi c_st-(\gamma_\theta+\gamma_{n\theta})t\right)\exp\left(\frac{-\xi^2c_s^2t^2}{h^4}\right)\Bigg\}$$

$$+2A_PA_P^*\left(\frac{w^2\zeta_P}{\Omega_P^2\zeta}\right)\exp\left(-\frac{4c_s^2t^2}{h^2+2\sigma_y^2}-2\Gamma q_\phi^2t\right)$$

$$+2A_TA_D\exp\left[-(D_T+D_s)q_\phi^2t-(\gamma_\theta+\gamma_{n\theta})t\right]$$

$$+A_T^2\exp\left(-2D_Tq_\phi^2t\right)$$

$$+A_D^2\exp\left[-2D_sq_\phi^2t-2(\gamma_\theta+\gamma_{n\theta})t\right]\Bigg], \qquad (8.4a)$$

where λ_o is the source laser wavelength and

$$\xi \equiv \left(\frac{1}{h^2}+\frac{1}{2\sigma_y^2}\right)^{-\frac{1}{2}} \qquad \zeta \equiv \left(\frac{1}{w^2}+\frac{1}{2\sigma^2}\right)^{-\frac{1}{2}}. \qquad (8.4b)$$

Because beam-crossing angles are usually small, the distinction between ξ and ζ can usually be ignored.

When the source beam is large compared to all other LITA length-scales, and the beam-crossing angle is small, Eq. 8.4a may be simplified further,

$$\frac{\mathcal{L}_{hom}}{P_o^2(t)} = \frac{\pi}{4}\left(\frac{\ell}{\lambda_o}\right)^2|\chi(\omega_o)|^2\left(\frac{w}{\sigma}\right)^2\Bigg[\mathrm{Re}\Bigg\{2A_P^2\exp\left(-2\Gamma q_\phi^2t+2iq_\phi c_st-\frac{4c_s^2t^2}{w^2}\right)$$

$$+4A_P A_T \exp\left(-(D_T+\Gamma)q_\phi^2 t + iq_\phi c_s t - \frac{c_s^2 t^2}{w^2}\right)$$
$$+4A_P A_D \exp\left(-(D_s+\Gamma)q_\phi^2 t + iq_\phi c_s t - (\gamma_\theta+\gamma_{n\theta})t - \frac{\xi^2 c_s^2 t^2}{h^4}\right)\Bigg\}$$
$$+2A_P A_P^* \exp\left(-2\Gamma q_\phi^2 t\right) + 2A_T A_D \exp\left[-(D_T+D_s)q_\phi^2 t - (\gamma_\theta+\gamma_{n\theta})t\right]$$
$$+A_T^2 \exp\left(-2D_T q_\phi^2 t\right) + A_D^2 \exp\left[-2D_s q_\phi^2 t - 2(\gamma_\theta+\gamma_{n\theta})t\right]\Bigg]. \qquad (8.5)$$

Recall that diffraction of the sound waves is not treated exactly, however. Eq. 8.5 will fail when the acoustic waves have traveled multiple grating widths.

Eqs. 8.1, B.1, 8.3, 8.4a and 8.5 are equalities valid in their respective limits and thus may predict absolute signal levels from assumed grating modulation depths ($\mathcal{U}_\theta$ and $\mathcal{U}_e$). They provide estimates of the absolute signal strength given a known susceptibility spectrum. These estimates are only approximate because the modeling to obtain $\mathcal{U}_\theta$ and $\mathcal{U}_e$ in terms of the gas susceptibility assumes a monochromatic driver laser.

The time history of the homodyne-detected signal depends upon the detection angle. The effect is different from that in heterodyne detection. Because the detection is not phase-sensitive, the signals scattered by the acoustic waves after they travel away from each other do not cancel. However, the Doppler beating between the signals scattered by the acoustic waves is a heterodyne effect. Thus, when the detection angle is large, the amplitude of the Doppler beats falls as the waves travel away from each other. The homodyne signal drops as the waves move away from the source beam. As happens in heterodyne detection of LITA signals, when the detection angle is small, the Doppler beats fade by motion of the waves away from the source beam.

The behavior of Doppler beats in the LITA signal, a classical interference, is entirely analogous to those of quantum interferences. For example, quantum mechanical scattering interferences arise from *in principle* indeterminacy in the path of the scattered particle. In LITA, the interference arises because of uncertainty in the origin of the scattered light while the acoustic waves overlap. As the waves move away from each other, the uncertainty and the Doppler beats fade. A small detector has inadequate spatial resolution *in principle* to determine the origin of the scattered light and

therefore sees Doppler beats even after the waves have moved away from each other.†

The LITA signal reflectivity has a $|\chi(\omega_o)|^2$ spectrum resembling linear scattering, considerably simpler than those of other nonlinear multiplex techniques, such as DFWM (Cooper, 1985, 1989). Broadband source beams with intensities low enough to prevent saturation may be used to measure these linear spectra in a single laser shot.

† Of course, the acoustic waves discussed in this analysis, like all acoustic waves, are coherent superpositions of phonons. A natural language of discussion of the results of the scattering analysis is the language of quantum-mechanical wave-particles, i.e., phonons and photons. An affinity to admit this vocabulary has been squelched in favor of avoiding thorny issues of dual wave/particle interpretations of the acoustic waves and thermal gratings.

Part III. Experiments, Data Analysis, and Results

CHAPTER 9

Experimental Apparatus

The LITA experiments performed at GALCIT reflect several design principles dictated by the requirements of the application of LITA to flows in the T5 free-piston shock tunnel. The first principle is that LITA experiments *must* be able to be performed in a single laser pulse. This requirement automatically excludes time-delay and laser frequency scanning experiments (although driver-laser frequency-scanning experiments were performed to demonstrate tuning effects). Thus, the source laser is either a CW or long-pulse laser whose scattered signal beam is time-resolved, or a broadband laser whose scattered signal beam is frequency-resolved. The second principle reflects a concern that the expense of certain laser diagnostics is prohibitive for many laboratories, including T5. Efforts were made to use the least expensive, most common, and most readily available equipment for the tests. Thus, a commercial-grade pulsed Nd:YAG laser, an argon-ion laser, and an inexpensive flashlamp-pumped dye laser are used. The most "exotic" laser used in the tests is a narrow-bandwidth, pulsed dye laser that was designed using the design recommendations of Duarte (1991) and built in-house for an order of magnitude savings in price over commercial models. The high-resolution spectrometer was also designed and built in-house at similar savings in cost. A sample startup cost for an unequipped laboratory interested in performing narrowband LITA is summarized in Table 9.1. The total cost to a start-up laboratory is an *order of magnitude* lower than that of comparable techniques appearing in the literature. The third design principle is that the experiments must be rugged enough to operate in the harsh, sooty, luminous conditions of the T5 test section and the quaking laboratory surrounding T5 during a test. The geometry of the beams has been chosen to minimize beam-steering effects. High f-number-detection optics reduce the sensitivity to luminosity and incoherent scattering. Experiments in T5 will ultimately judge whether this principle is satisfied.

Equipment	*Approximate Cost $\$ \cdot 10^3$ [1995]*
Pulsed, Frequency Doubled Nd:YAG Laser	25
In-house Manufactured Narrowband Dye Laser	5 *(+ 3 student-months labor)*
Ar Ion Laser or Flashlamp-Pumped Dye Laser	20
Ancillary Laser Equip (Heat-exchangers, etc.)	10
Optical Table or Bench	5
Optics (Mirrors, Lenses, Mounts)	5
Detectors	1
Digital Storage Oscilloscope	10
Total	81

TABLE 9.1 Startup equipment and cost of a narrowband LITA System.

9.1 Optical Apparatus: Narrow-Bandwidth LITA

Fig. 9.1 shows a schematic diagram of the experimental apparatus used in narrowband and multiplex LITA experiments. The driver laser is a pulsed dye laser with a noise bandwidth of about 2 GHz. In most experiments, this laser was pumped by a Q-switched, frequency-doubled Nd:YAG laser (Continuum, model YG-660) at 150 mJ/pulse. In later experiments, a similar, but more powerful (300 mJ/pulse) Nd:YAG laser was used (Continuum, Surelite 2). The dye laser emits excessive amplified spontaneous emission when pumped by the full energy of the more powerful laser, thus the pulse energy of the pumping laser is adjusted so the dye laser emits ~40 mJ of light. The pulse temporal profile is a slightly skewed Gaussian with an intensity full-width-at-half-maximum of ~5 ns. Optically nonlinear KDP crystals could have been used to convert light from the Nd:YAG and dye lasers to ultraviolet light for the probing of species such as NO and OH. Experiments to date, however, have been conducted with the driver laser wavelength in the visible 587-594 nm range, the bright amber color of sodium lamps. The polarization of the driver beam is vertical (into the page). A 50% beamsplitter (bs) evenly splits the driver laser emission. The split beams are synchronized in time and made parallel using mirrors $m2$, $m3$, and $m4$ in kinematic mounts on micrometer-driven translation stages. The driver beams intersect at the focus of the 500 mm lens $\ell 1$ where they approximate finite plane waves about 270 μm in diameter with a propagation vector tilted ~0.15° upward. The beam-crossing angle is set by the distance between the parallel beams. The plane of bisection of the driver beams is normal to the windows of a high-pressure test cell and approxi-

mately centered on the windows. This arrangement effectively eliminates changes in the magnitude of the grating vector with changes in the refractive index of the gas in the bomb and minimizes the effect on the driver beams of the deformation of the windows under pressure loading. Detection of the driver beam pulse by a silicon PIN photodiode, *d1* (Thor labs, model DET-2SI), with a rise time <1 ns, triggers the acquisition of the LITA signal. In frequency scanning experiments, the high-resolution spectrometer monitors the driver laser frequency.

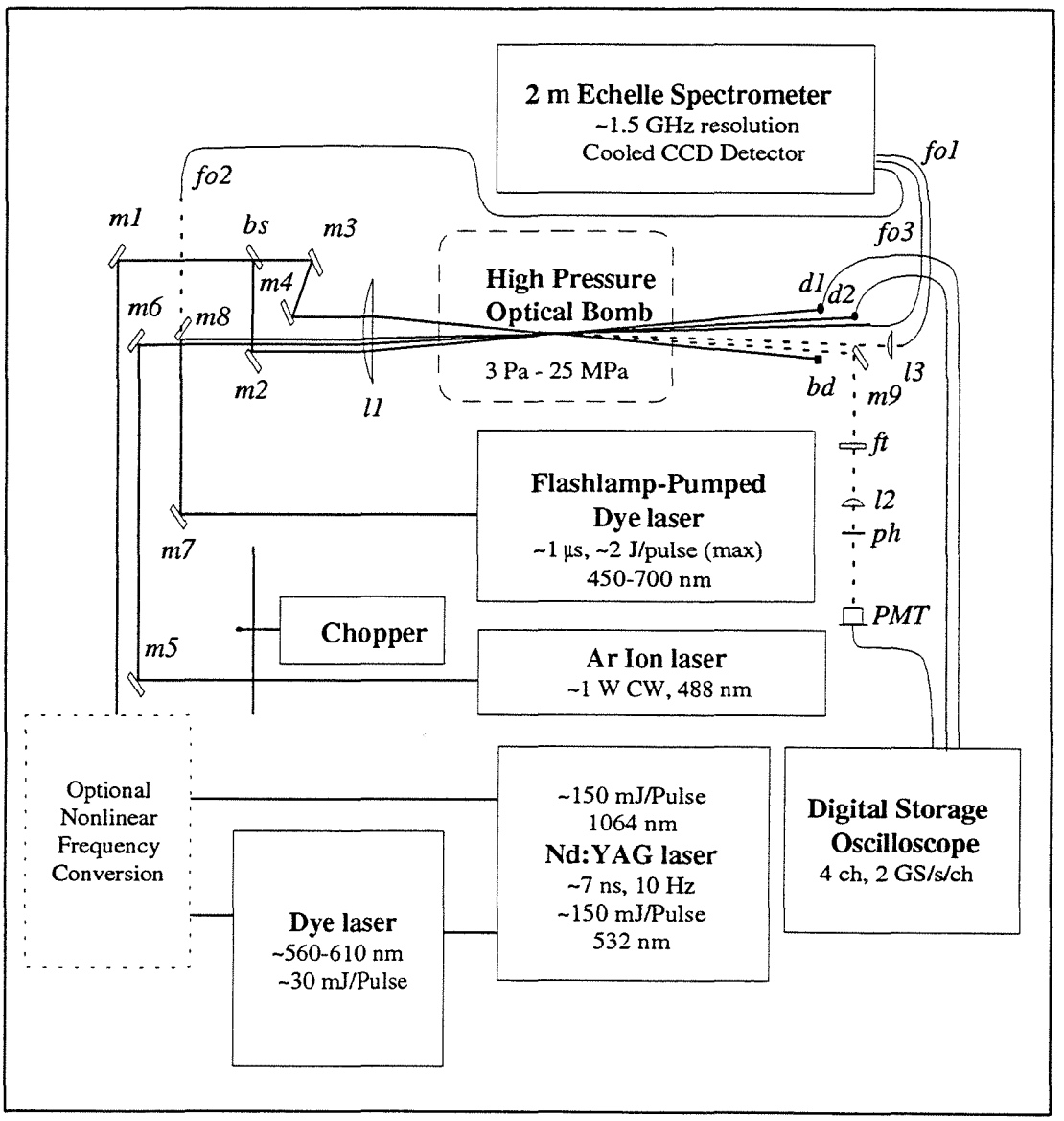

FIG. 9.1. Schematic diagram of narrowband and multiplex LITA experimental arrangement.

The source laser used in narrowband LITA experiments is a CW argon-ion laser producing ~1.3 W at 488 nm (Spectra Physics Model 165). A chopper wheel passes ~1 ms pulses from the CW beam at 10 Hz, synchronized with the driver laser pulses. Pulsing minimizes the perturbation in the gas caused by the source laser, which can otherwise be sizable in stationary, high-pressure gases. Pulsing also reduces the time-integral of incoherently scattered light on the PMT, extending detector life. The source beam is carefully adjusted using mirrors $m5$ and $m6$ in kinematic mounts so that lens $\ell 1$ focuses the beam onto the same volume as the driver beams, with a propagation vector parallel to the table. Phase-matching adjustments are made using a micrometer-driven translation stage under $m4$. This beam geometry is called folded-BOXCARS forward phase-matching (Eckbreth, 1988) and is useful for separating weak signal beams from strong pump beams. Because the finite beam analysis treats in-plane beams, the out-of-plane component was limited to ~one-tenth of the in-plane beam-crossing angle, which ranged between 1.0° to 2.3° in these experiments. The source laser was directed parallel to the table to minimize source and signal beam offsets which would otherwise arise when the bomb is pressurized. A silicon PIN photodiode, $d2$, (Thor labs, DET-2SI) monitors the intensity of the source beam.

The narrowband LITA detection system consists of a fast photomultiplier tube (PMT) (Hammamatsu model OPTO-8) with at least a 500 MHz signal bandwidth and optical filters to prevent signal contamination, including a 10 nm interference filter $f1$ at 488 nm and a 40 mm lens, $\ell 2$ and 20 μm pinhole spatial filter, ph. The LITA signal path-length to the detector is about 2.5 m. Data are recorded using a 2 GS/s/channel, eight-bit, four-channel 500 MHz digital storage oscilloscope (DSO) (TEK 640A). This records 2000-sample time histories of signals from the PMT and photodetectors. The DSO is connected to a Sun Sparc 2 workstation over a GPIB link which permits remote computer control and data storage. The DSO can record the driver laser, source laser, and signal beam temporal profiles each driver-laser shot, a practice which is important for analyzing single-shot measurements. Often, however, noise is eliminated from signals by recording multiple-shot driver-laser and signal averages, since a principal goal of the research is to check the validity of the model, not merely the capability to perform single-shot measurement. Averaging the signal reduces shot noise and the effect of plasma noise and mode-noise of the source

laser which has a frequency of ~150 MHz and a modulation depth of ~10%. There is also a component of the signal noise from the DSO of ~500 μV rms which can be reduced to ~20 μV by averaging and background subtraction.

9.2 Optical Apparatus: Multiplex LITA

The multiplex LITA apparatus employs the same driver laser as the narrowband apparatus (Fig. 9.1). Multiplex and narrowband LITA may be performed using the same laser-induced gratings (further multiplexion). The source laser for multiplex LITA is a flashlamp-pumped dye laser (Cynosure, model SLL-500) with a pulse energy of ~1 J and a pulse duration of ~700 ns. The laser temporal profile features a rapidly rising leading edge and a long decay tail. The dye laser was modified to remove mode structure resulting from etalon effects of on-axis windows of the dye cell. Brewster-angle windows replaced the on-axis windows of the dye cell and dielectric-coated Littrow prisms replaced the total reflector and output coupler. Whispering-gallery modes of the dye cell are suppressed using a stainless steel wire wrapped helically around the inside of the dye cell (Tasjian, 1994) and stainless steel apertures at both ends of the dye cell. The modified laser emission line spectrum is nominally ~0.5 nm wide, coarsely tunable by tilting the Littrow prisms. The cavity length is ~1 m.

Mirrors $m7$ and $m8$ direct this source laser beam through lens $\ell 1$ and into the sample volume at the phase-matched angle. The weak transmitted beam from mirror $m8$ serves as a reference beam which is focused on a 50 μm optical fiber $fo2$. This source-beam propagation vector is tilted upward by about twice the amount of the driver beams, thus avoiding interference with the narrowband LITA source laser. The unscattered source beam, bearing a line-integrated absorption signal, is incident on a 50 μm optical fiber. The signal beam is focused by lens $\ell 3$ into a similar optical fiber. The optical fibers feed a high-resolution 2.5 m echelle spectrometer with a frequency resolution of about 1.2 GHz at the dye-laser frequencies (about 1 frequency part in 400,000). The output of the spectrometer is imaged onto a Thomson 578×384-pixel, thermoelectrically cooled CCD array (Princeton Instruments, model LC/ICCD). The CCD camera signal is digitized with a 14-bit analog-to-digital converter (Princeton

Instruments, model ST130). A PC-clone computer (Gateway 2000, model 486/33C) records and processes the digitized signals.

9.3 Optical Apparatus: Heterodyne LITA Velocimetry

The heterodyne LITA velocimetry apparatus uses the same driver and source beam positioning equipment as the narrowband LITA apparatus. The difference between the heterodyne LITA and the regular narrowband LITA experimental arrangement is in the signal detection scheme, illustrated in Fig. 9.2. In heterodyne LITA, the interference of the signal beam and a reference beam modulates the intensity of the light on the detector. The Doppler shift of the signal beam from scattering off a convecting grating causes frequency beating with the reference beam at the frequency of the Doppler shift. The velocity of the grating in the direction of the grating vector may thus be measured. Phase-sensitive heterodyne detection is the most accurate way to measure velocity using LITA. Three difficulties are associated with optical heterodyne techniques. First, the signal and reference beam should be time-synchronized well within the decoherence time of the source laser. This is achieved using an adjustable prism delay line in the reference-beam path, shown in Fig. 9.2. The second difficulty is that the signal beam and reference beam must be combined and should copropagate well within the angular beam divergences. The time-synchronization and angular alignment are necessary for efficient interference of the signal and reference beams. This is achieved with the aid of kinematic mounts and translation stages on the signal mirror and the beam-combiner. The third and most difficult requirement is that the reference beam should be only slightly more intense than the signal beam to limit the exposure of the PMT to damaging levels of light. This is accomplished by using uncoated glass prisms in the delay line and an uncoated glass wedge to combine the signal and reference. The reflectance of uncoated glass at 45° incidence is approximately 10% for light polarized normal to the plane of tilt (s-polarized light) and approximately 1% for light polarized in the plane of tilt (p-polarized light). Because the emission of the argon-ion laser is vertically polarized, two surface reflections off the uncoated prism (and two total-internal reflections) leave between 1% and 0.01% of the incident light in the reference beam, depending on the direction of rotation of

the prism pair. The surface reflection off the wedge beam combiner reduces the reference intensity by another factor of ten, providing a range of adjustment of reference beam power suitable for signals with reflectivities of 10^{-3}–10^{-5}.

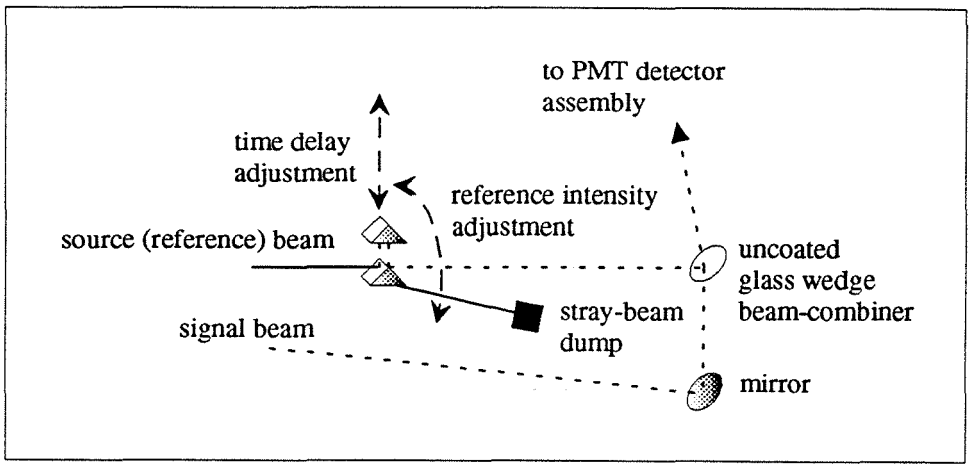

FIG. 9.2. Diagram of LITA velocimetry heterodyne-detection scheme.

9.4 Bomb with Optical Access and Gas-Handling Apparatus

After the first series of experiments using laboratory air, it was decided to test the analysis of LITA signals from gases of carefully controlled composition, temperature, and pressure. A bomb with optical access was designed and built for the purposes of this study. The design parameters of the bomb are summarized in Table 9.1. Photographs of the bomb appear in Figs. 9.3 and 9.4. A 152 mm (6 inch) cube of mild steel with 51 mm (2 inch) diameter through-holes centered on each face comprises the body of the bomb. Window holders, transducer ports, and plumbing is attached via six circular flanges, each connected using four 16 mm (0.625 inch) bolts. The bomb is fastened to an optical table on a four-post stand which raises the windows to the desired height. A steel frame towers over the bomb, supporting 32 mm (1.25 inch) vacuum/vent pipes.

Parameter	*Description*
Design Working Pressure Range	3 Pa - 40 MPa (at room temperature)
Current Hydraulic Test Pressure Limit	25 MPa
Temperature Range	Resistance heating to 600 K. Optional flat-flame or bunsen burner with gas purge
Optical Access	Four 25.4 mm diameter viewports in orthogonal directions
Optical Windows	Four fused-silica windows $\lambda/10$ flatness High-power broad-band anti-reflection coating 38.1 mm diameter, 25.4 mm thickness
Accessories	Internal mixing fan Window mount extensions for up to 900 mm optical path length Eventual use as test section of Combustion-Driven Shock Tube, described in Belanger (1993)

TABLE 9.2 Design parameters of the High-Pressure Optical Bomb.

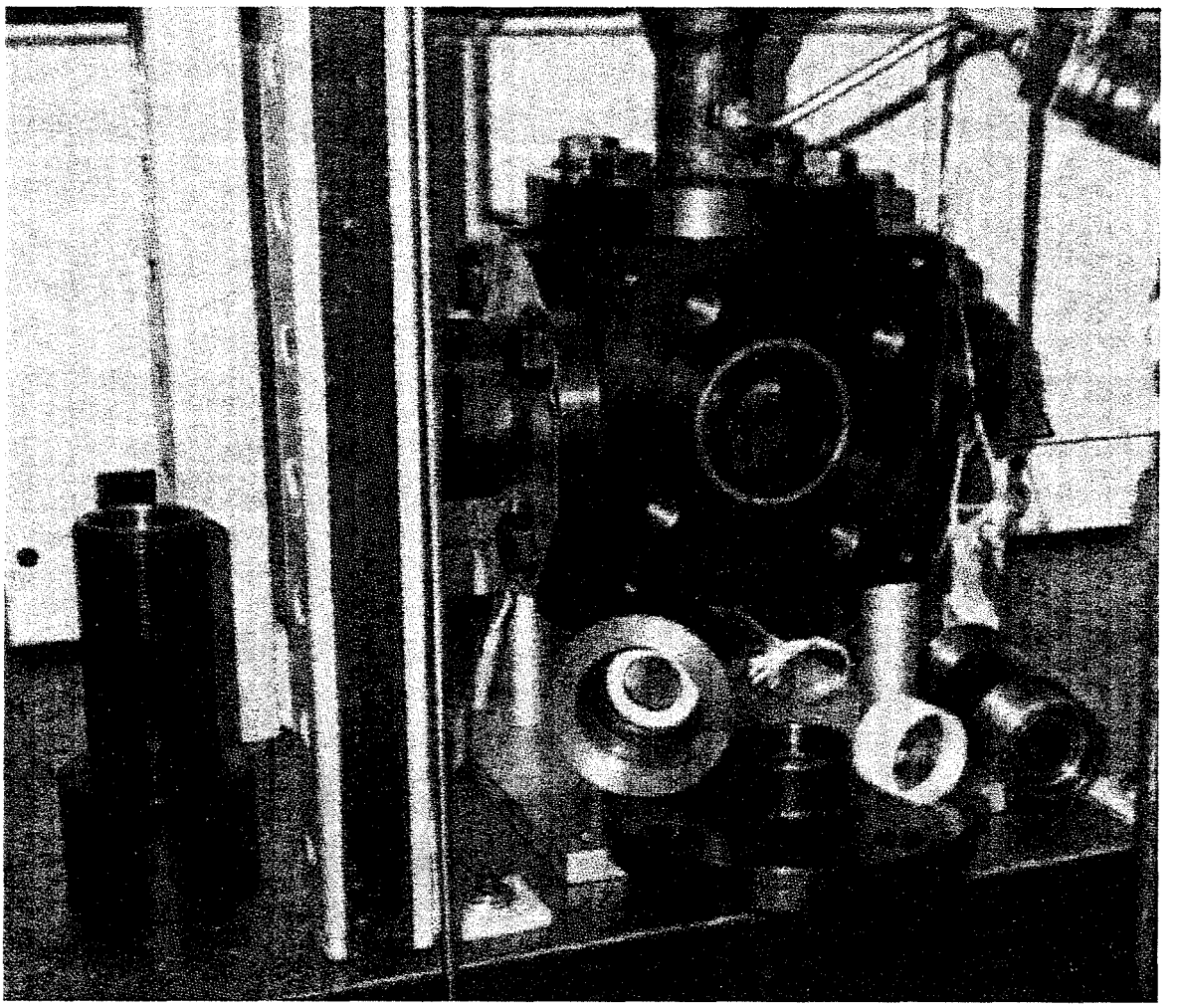

FIG. 9.3. Photograph of High-Pressure Optical Bomb. The window-holder flange on the facing side has been removed. A window holder, window, and several extension tubes surround the bomb. The hole spacing of the table is 25.4 mm (1 inch).

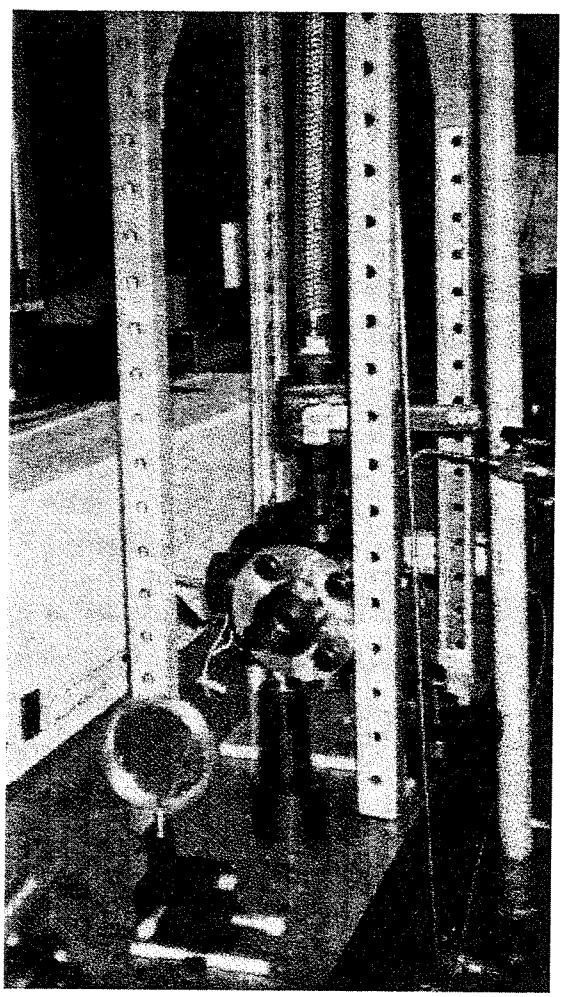

FIG. 9.4. Photograph of High-Pressure Optical Bomb, steel tower, and vacuum pipe. The lens in the foreground is lens $\ell 1$ in Fig. 9.1.

The gas-handling system has been designed to permit careful control and monitoring of the gas composition and condition in the bomb. A thermocouple monitors the temperature of the gas near the sample volume to 0.1° C. A Pirani vacuum gauge and a capacitance manometer provide accurate absolute pressure readings from 3 Pa (30 mtorr) to 1000 torr. A logarithmic series of four gauges enables 0.25% pressure measurement from 100 kPa to 40 MPa. All of the gauges and plumbing serving the bomb can be vented or evacuated to the outside independently. High-pressure gas cylinders may feed the bomb directly or through a regulator. A separate system kept below atmospheric pressure is used to handle toxic gases such as NO and NO_2. The filling, venting, and evacuation of the bomb may be controlled precisely through a needle valve, or performed rapidly through the 32 mm pipe leading vertically from the bomb. The gas-handling system and bomb are evacuated using a "wet" vacuum pump (Leybold, model D8A) capable of pulling a vacuum of ~3 Pa (23 mtorr).

CHAPTER 10

Processing of LITA Signals

This chapter discusses the scheme that is used for the interpretation of LITA signals. Signal processing is a sequence of operations and filters applied to a noisy signal to extract signal parameters. Often, processing involves the use of various linear frequency filters to reject noise with frequency components outside the anticipated signal spectrum. If the signal spectrum is well known, the so-called optimal linear filter or Wiener filter may be used. The Wiener filter extracts a best estimate of the pure signal given the noisy signal and knowledge of the signal and noise power spectra. This filter excels over simple band-pass and cutoff filters because it incorporates some basic knowledge about the nature of the signal.

If the nature of the signal is known precisely in terms of a finite number of signal parameters, a truly optimum *nonlinear* filter can be constructed. This filter extracts a best estimate of the pure signal and values of the signal parameters by adjusting the values of the signal parameters to obtain the global minimum of a deviation function. The deviation function measures in some way, for example in the χ-squared sense, the deviation of the theoretical and noisy signal. The optimal nonlinear filter exploits the vastly reduced dimensionality of the space of possible signals, a "trick" often used in the field of digital communications.

10.1 Optimal Nonlinear Filtering

There are some complications associated with these filters. The determination of the global minimum of the deviation function can be very difficult. Also, the optimum parameter values may depend upon the definition of the deviation function. The problems of minimizing the deviation function of a signal of two parameters may be understood by analogy. Consider trying to locate the minimum altitude of a group of hills or mountain range by overhead observation. The problem is exacerbated by the presence of trees and undergrowth (noise). If the trees are uniform and evenly distributed or if they are much smaller than the hill-height, a good estimate of the minimum can be made. However, if the trees are tall and unevenly distributed, false minima may be found. These false minima may not even be local to the true minimum if the landscape is ill-conditioned. Thus, the uncertainty in the measurement is not a simple function of the tree height, aerial viewing resolution, or even the statistics of the altitude distribution of the landscape. For global minimization of a many-parameter deviation function, this "aerial view" method for global deviation minimization is impractically computationally intensive. What is usually done computationally is somewhat analogous to dropping a large semi-elastic ball with an altimeter down the mountain and finding the altitude at which it settles. Clearly this method is fraught with pitfalls, but there are few practical alternatives. Obviously this technique can be improved by dropping the ball near where the minimum is expected. A knowledge of the general trends of the terrain may be used to decide where to drop the ball. At worst, independent measurements of the coordinates of the minimum could be used, etc., but these could also lead to false minima and an unhealthy dependence on independent measurements! Thus, global minimization is an inherent difficulty that is exacerbated by noise.

The second complication of the technique is that real signals are imperfectly modeled by functions of practical dimensionality. The effect of modeling errors on extracted parameter values is impossible to quantify in a general manner. A modeler may elect to reduce modeling uncertainty either by increasing the dimensionality of the parameter set or by modeling the signal more realistically using the existing parameters. However, the addition of new parameters complicates global minimization

and may lead to less accurate parameter estimation by worsening the conditioning of the deviation function. Improving the fidelity of the model using a limited set of unknown parameters is the best way to minimize modeling uncertainty. Unfortunately, this technique can become computationally intensive. Thus modeling uncertainty is another inherent problem with optimal nonlinear filtering.

10.2 Nonlinear Filtering of LITA Data

An optimal nonlinear filter is used to extract parameters from the time-resolved, narrowband LITA signals. The filter is a nonlinear least-squares fit of the data to the model for LITA signals from finite beams. The independent parameters of this model are c_s, D_T, Γ, γ_θ, D_s, θ, σ, and w, whose definitions are given in the derivation. Three additional parameters were fit: τ, the time delay between oscilloscope triggering and the arrival of the signal beam, and $\mathcal{U}_\theta$ and $\mathcal{U}_e$, coefficients proportional to the amplitude of the thermalization and electrostriction driving terms, respectively. No attempt was made in the nonlinear filtering to extract parameters based on the *absolute* signal intensity. The beam-geometrical parameters may be independently measured, thereby eliminating extraneous degrees of freedom in the model and speeding the numerical filtering. Table 10.1 summarizes the fitting parameters, lists the equations in which these parameters appear explicitly (the parameters also appear implicitly in other equations), and comments on how the parameters were fit or determined.

Parameter	*Description*	*Explicit Usage*	*Comments*
c_s	sound speed	5.14d, 5.14g, 5.15a-e, 7.3c-d, 8.3, B.1	most precisely determined gas property
D_T	thermal diffusivity	5.14d, 5.15c, 5.15e, 7.3d	most precisely determined diffusivity (if signals arise from thermalization.)
γ_θ	thermalization rate	5.12, 5.14d, 5.14g, 7.3d	effectively infinite at high pressure
Γ	acoustic damping coefficient	5.14d, 5.15a-b	sensitive to beam misalignment, usually assumed prop. to thermal diffusivity
D_s	excited-state diffusivity	5.12, 5.14d, 5.14g, 5.15d, 7.3d	very weak signal dependence, assumed proportional to thermal diffusivity
$\mathcal{U}_\theta$	thermal grating relative amplitude	5.12, 8.2	relative measurement only
$\mathcal{U}_e$	electrostriction grating relative amplitude	5.12, 8.2	relative measurement only, not fit when electrostriction is negligible
τ	time of driver pulse	subtract from t in 8.3 and B.1	trigger delay depends on DSO time-base setting, precisely determined
θ	driver-beam crossing angle	5.2a-b	precisely determined in calibration, not fit otherwise
w	driver-beam half-width	5.2b, 5.12, 5.15e, 7.3b, 8.3, B.1	determined in calibration, not fit otherwise
σ	source-beam half-width	7.3b, 7.3e	determined in calibration, not fit otherwise

TABLE 10.1 Summary of LITA signal fitting parameters.

A computer program based upon the Levenberg-Marquardt method locates a minimum of the χ-squared deviation between experimental data and the theoretical model. This technique, also known as the Marquardt method, is described in detail in *Numerical Recipes* (Press et al., 1986) and elsewhere. The minimization subroutines used to fit LITA data are adapted from examples in this text. The principal adaptations are the use of 16-byte complex and 8-byte real numbers in the calculations and modifications in function calls to optimize execution speed. The derivatives of the modeled signal with respect to the fitting parameters are obtained using a two-point forward-difference scheme. The fitting routine reads initial guesses for parameters either from a default parameter file or a saved, data-set-specific parameter file.

The minimization subroutines serve a data analysis program which can fit multiple data sets automatically or interactively. The program tracks the number-density of up to ten gaseous constituents, temperature, and experimental parameters such as PMT voltage, laser intensity levels and histories, background measurements, number of signal averages, etc. These parameters are parsed from an ASCII preamble to each data set written by the operator at the time of data collection. The operator load is minimized by requiring only the recording of changes in experimental parameters.

The data analysis program writes the gas-composition, experimental, and fit-signal parameters to an ASCII file formatted for spread-sheet post-processing. This file also includes computer-estimated uncertainties of the fit signal parameters.

Equation B.1 from Appendix B was first used to fit data sets. Later, Eq. 8.3, in which the two-dimensional convolution over the relatively short laser pulse is approximated by a one-dimensional convolution was found to be adequate for fitting purposes. This approximation speeds execution by approximately a factor of ten, allowing 240 sequentially acquired data sets to be fit in 2–3 hours on a SUN Sparc 5, and is used in the fits that appear in Chapter 11. The optimization of execution speed and model fidelity is a continuing endeavor.

The Levenberg-Marquardt method is robust in extracting reasonable values of LITA signal parameters even when initial guesses are poor. The data analysis program requires manual selection of the initial parameters. In automatic mode, after the initial fit, the program uses parameters from the previous data set for initial guesses for the next. Because sequential data sets are often acquired with small changes in the laser tuning or gas properties (i.e., small fractional pressure increase or decrease), this method works well. In early versions, however, when the signal changed significantly between data sets (for example, the gain of the PMT was changed by a factor of 20), parameter values left the region of the global minimum. This problem was mitigated by placing limits on the permissible range of parameters (e.g., if the sound speed should be 350 m/s, the permissible range of variation of the parameter is 275 m/s – 450 m/s to prevent locking to harmonics and subharmonics). Furthermore, the time integrals of the signal calculated using initial guesses and the experimental signal were matched. Originally, the various diffusivities of the gas were fit entirely independently. The diffusivities vary over several orders of magnitude during a sequence of experiments. There are apparently secondary minima in the deviation function corresponding to erroneous values of the diffusivities. The current version of the filtering program essentially fits the thermal conductivity and ratios of diffusion rates, which change only slightly in consecutive measurements, with significant improvement in fitting performance and speed. The successful automation of the nonlinear filtering speeds the reduction of data. At approximately one-minute per data set, the data reduction rate is comparable to the rate at which data can be recorded (allowing settling time).

Gas-property measurements appearing in Chapter 11 were extracted from LITA signals by a sequence of filtering operations. First, the nonlinear filter was applied to all data sets in an experimental run with fitting parameters of the time delay, thermalization amplitude, electrostriction amplitude, thermal diffusivity, acoustic damping rate, thermalization rate, beam sizes, and driver beam-crossing angle.‡ The sound speed was held constant at its correct value at atmospheric pressure and 300 K. This initial filtering operation enabled best estimates of the beam-sizes and crossing angles to be "calibrated" from the data. Next, the data sets were filtered using the gas properties as fitting parameters and holding the beam parameters constant at their calibration values. This second filtering operation was usually performed several times, using a variety of beam sizes, since there was usually a range of sizes indicated by the calibration filtering. The results of the second set of filtering operations that appear in Chapter 11 used the combination of beam sizes that provided the best fits over the range of experimental conditions. The repeated filtering of the data sets was necessitated by the difficulties of finding the global minimum of the deviation function.

There are several additional notes about the filtering procedure. Measurements of acoustic-damping rate were compromised by finite-beam-size effects. At high pressure, this parameter was set to an estimated value in order to avoid fitting complications. At high pressures, beam self-focusing and self-defocusing effects (described in more detail in Chapter 11) create uncertainties in the beam sizes, possibly invalidating the calibrations. With this caveat, the calibration procedure would be improved by directly measuring the beam parameters. At low pressures, finite-thermalization-rate effects were not accurately treated by the single-rate model used in the analysis, particularly in tests using helium as the buffer gas. Beam misalignment effects were not treated in the analysis. These modeling errors introduced systematic deviations of the theoretical and experimental signals. In obtaining a best fit of the flawed model to the experiment, the filter often skewed the extracted gas properties. These problems are discussed in more detail in Chapter 11.

---

‡ In many tests, electrostriction produced a negligible signal and thermalization rates were practically infinite, thus the set of fitting parameters was reduced accordingly.

CHAPTER 11

Selected Results of LITA Experiments

LITA enables measurement of a broad and diverse range of thermophysical and chemical properties of fluids. Possible experimental arrangements of LITA are likewise diverse. Practical concerns necessarily limit the scope of the studies and the results presented in this section. The study employs only focused beams, useful for obtaining strong signals and good spatial resolution, but harmful to the measurement accuracy of acoustic damping rates and sound speeds. The use of focused beams assists in the goal of verifying the integrity of the finite-beams analysis presented in Chapters 4 through 8. A beam at 488 nm from an argon ion laser served as the source beam in the narrowband LITA measurements. Thus, source laser tuning was not possible, although multiplex LITA provided information about such effects. In these experiments, the grating wavelength ranged from ~10 μm–30 μm. The Knudsen number of the grating varied over five orders of magnitude as the absolute pressure of the test gas ranged from ~100 Pa to 14 MPa. Most experiments were conducted at room temperature. A series of tests addressed the issues of fluid motion and turbulence. LITA experiments were successfully conducted near the region of the liquid-vapor critical point of CO_2, where incoherent light scattering and beam steering effects complicate measurement. The opto-acoustic effects that contributed significantly to the detected signals were thermalization and electrostriction. Secondary effects, such as thermophoresis, were unimportant at the seed-gas concentrations that were used. Photolysis was not evident or expected at the driver-laser photon energies that were used.

Although limited in scope compared to the remarkable diversity of possible applications, this research explores a broad range of effects and conditions. Experimental technique improved over the course of the tests. Repeating and refining early experiments could be done only at the expense of the scope of the studies. In most cases, the author chose to move onward, in the spirit of exploration. Earlier work will eventually be refined after the broad survey reveals the strengths and weaknesses

of the various implementations of LITA. The data appearing in this section are all flawed to some extent from signal-recording infidelities, imperfect fluid mixing and concentration uncertainty, temperature uncertainty, laser beam size and profile uncertainty, beam misalignment and steering effects, and perhaps other effects yet to be identified. Each problem has been addressed as it was diagnosed. The author wishes to stress that practical concerns have limited the accuracy of experimental measurements that are presented here, not the physics of LITA. Important signal "flaws" and their causes, notably beam misalignment, are discussed and demonstrated for future researchers who use LITA.

The "flaws" in the signals do not entirely prevent accurate gas property measurement, for example ~0.1% uncertainty could be achieved in the sound speed derived from LITA signals. The predictions of the finite-beam analysis match experimental results with remarkable fidelity. Transport property measurements, most susceptible to signal flaws, achieve reasonable accuracies (~10% for thermal diffusivity). This degree of accuracy, given the relatively unsophisticated nature of these early experiments portends well for applications of LITA in carefully controlled experiments and practical experimental systems, for example, T5.

The finite-beam analytical model derived in Chapters 4 through 8 accurately represents the signals of the narrowband LITA experiments, as illustrated by a series of experimental and modeled LITA signals that covers the studied Knudsen number range. The effect of driver laser tuning on the measured signal is demonstrated by measuring a susceptibility spectrum of the laboratory air at frequencies near that of the sodium D-line. The spectrum bears modulation from NO_2 present in the air in concentrations less than 50 parts-per-billion ($\sim 10^{-15}$ g of NO_2 in the sample volume), demonstrating ultra-sensitive detection capability. The pressure dependence of the peak and integrated signals is explored. Gas property measurements of "pure" and NO_2-seeded air, He, and CO_2 are presented, including measurements approaching the region of the liquid-vapor critical point of CO_2. In a study of the effects on the signal of turbulence in the test gas, homodyne LITA anemometry and heterodyne LITA velocimetry are demonstrated. These experiments provide a glimpse of some potential applications of LITA. Experimental notes describe and illustrate beam misalignment effects, beam self-focusing and defocusing effects, and other considerations associated with LITA diagnostics, particularly those which appear in high pressure gases.

11.1 Comparison of Theoretical and Experimental LITA Signals

The expression for LITA signals from finite-beams faithfully models experimental signals. The nonlinear filter discussed in the data analysis section employs this expression as the signal model. The accuracy of the analysis is judged by the quality of the fit to the experimental signal and the accuracy of the signal parameters derived from the fit. The fidelity of the analysis for reproducing LITA signals taken at low grating Knudsen number is illustrated in Figs. 11.2 through 11.7. The Knudsen number was adjusted by varying the pressure at roughly constant (room) temperature. In these figures, raw LITA signals from thermalization in NO_2-seeded air are overplotted with "filtered" signals—theoretical signals with optimized signal parameters. The filtered signals were obtained using the automated routine described in Chapter 10. The experimental signals are the averages of between 10 and 1,000 laser shots to reduce the noise sufficiently to expose systematic deviations between theory and experiment.

Fig. 11.1 shows the strongly damped signals obtained at large Knudsen number ($\sim$1). At Kn = 1.24, the signal is so strongly damped that there is no evidence of ringing associated with wave motion. Acoustic waves near Kn = 1 are strongly damped and scattered or dephased. The thermalization rate is low, inhibiting coherent-wave formation. The rapid decay of gradients associated with these waves is not diffusive, since the average step size of the "random walk" of the molecules is not negligible on the scale of the gradients. The Navier-Stokes equations used to derive the signal model do not properly describe the fluid in this regime. An improved model based upon the Chapman-Enskog or Boltzmann equations is required. The model is able to reproduce the behavior of the signal superficially, but the signal parameters extracted from the fits are accurate only to $\sim$40%. As the Knudsen number drops below one, the first evidence of "organized" or "coherent" gas behavior appears. This coherence manifests itself in the formation of a tail to the signal peak and changes in curvature of the tail from nascent organized wave motion.

In Fig. 11.2, the Knudsen number of the grating is low enough that coherent waves generated by the driving laser are able to propagate distances comparable to the grating wavelength before being decimated by damping and scattering. Additional signal

maxima appear, vastly improving the precision of sound speed measurement. While the uncertainty of the sound speed drops, there is apparently a trend toward over-predicting the sound speed (an effect of the order 10% at this condition). At these grating Knudsen numbers, the rate of rotational relaxation is comparable to the Brillouin frequency. Thus the effective ratio of specific heats approaches the value for a monatomic gas, increasing the sound speed. Also, since the gas is rarefied, the momentum borne by the waves propagates more freely (with fewer impeding collisions) than that of a "continuous" gas. Thus, the average speed of momentum conduction is weighted slightly toward the mean thermal speed of the gas, $\sqrt{8\mathcal{R}T/(\pi M.W.)}$, which, in air is ~35% higher than the sound speed.

In Fig. 11.3, the ringing from the coherent wave motion becomes the dominant feature of the signals. As the pressure increases, the thermalization rate rises, deepening the modulation of the ringing. The Knudsen number is low enough to validate the treatment of the gas dynamics using the Navier-Stokes equations. Precision and accuracy of the sound speed extracted from the filter is $\sim$ 0.1%, a figure which does not change appreciably as the pressure is increased. The accuracy of the thermal diffusivity measurements in this range is ~10%, limited by inaccuracy in the extracted acoustic damping rates, beam misalignment effects, and finite-thermalization-rate effects. The filtered signal from air at 44 kPa departs systematically from the raw signal for large values of time. This departure arises in part from the beam uncertainties and in part by the difficulty of locating the optimum signal parameters using an automated routine. Small errors in beam positioning and beam refraction effects contribute to a steady beam misalignment in static (no flow tests). In tests on flowing gases, aero-optical effects may contribute a non-steady misalignment.

The trend toward increased depth and duration of the ringing continues in Fig. 11.4, along with the difficulty of locating the optimized parameters and the detrimental effects of (slight) beam misalignment, as evidenced by the poor fit between theory and experiment. Finite-beam-size effects begin to play a significant role in the signal. The minima of the valleys of the signal begin to increase in time, which occurs when the wavepackets begin to travel away from each other. The detector is able to resolve the signals scattered by the waves. The amplitude of the Doppler beating

in the signal—the modulation depth of the ringing—fades faster than by damping processes alone. The growth of this finite-beam-size effect with increasing pressure is evident in Fig. 11.5.

Finite-beam-size effects dominate the modulation of the ringing of the signal in Fig. 11.6. Beam size and alignment effects seriously degrade acoustic damping rate measurements. The filter often attributes the effect of slight misalignment of the source beam to a negative damping rate. Thus, unless beam alignment is precise and beam shapes are nearly Gaussian, acoustic damping rate measurement may be hopelessly compromised. Incorrect acoustic damping rates affect the accuracy of thermal diffusivity measurements around these pressures. Thus, the acoustic damping rate is given only a narrow latitude around being proportional to the thermal diffusivity at and above these pressures, a good first approximation, except possibly in the rarefied limit, in inhomogeneous gases, or near the liquid-vapor critical point. The accuracy of the thermal diffusivity measurements and quality of the signal filtering is underscored by comparison of the extreme tail of the signal with the theoretical tail in the inset of Fig. 11.6. With accurate beam alignment, the tail and the ringing portion of the signal can only be fit simultaneously if the thermal diffusivity is chosen correctly.

Fig. 11.7 shows the raw and filtered signals at yet higher pressure, where two distinct regions emerge, a ringing part and a tail. While the filtered signal appears to fit both sections reasonably accurately, there are systematic deviations in the tail and the transition region (see inset figure). The poor fit in the transition region probably results from non-Gaussian beam shapes and an inaccurate acoustic-damping rate. Fig. 11.8 shows the raw and filtered LITA signals from air at 3.45 MPa. The inset figure shows the fit of the ringing section of the signal. Extra energy in the wings of the beam profiles over the Gaussian ideals causes the deviation between the signal and the model in the transition region between the ringing part and the tail. The good overall fit of experimental and theoretical signals indicates beam alignment was nearly ideal during the acquisition of the signal. Fine alignment of the beams is now performed by finely adjusting the source beam location and direction until the LITA signal at high pressures appears like that in Fig. 11.8.

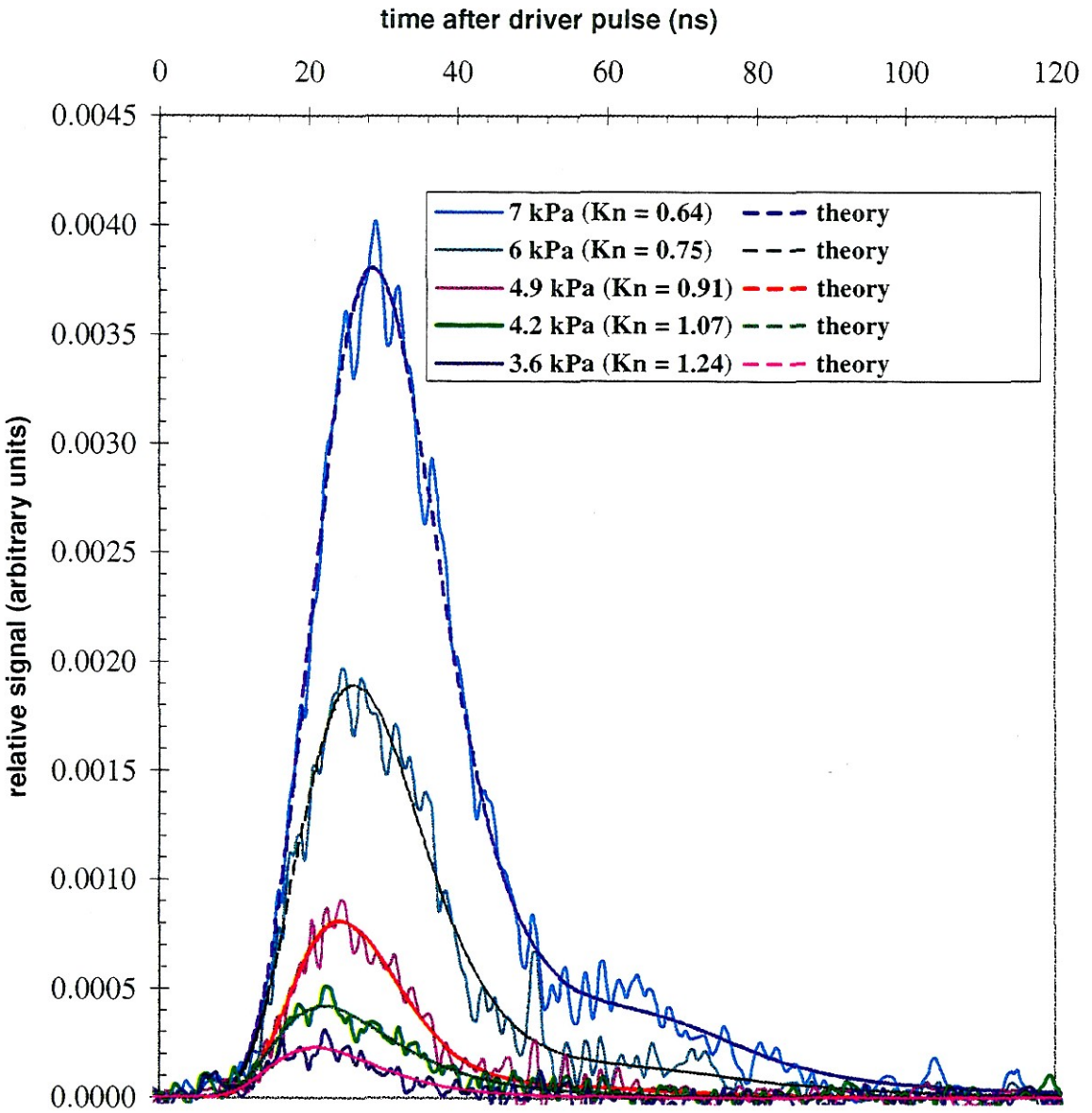

FIG. 11.1. Narrowband LITA signals from rarefied NO_2-seeded air at ~300 K.

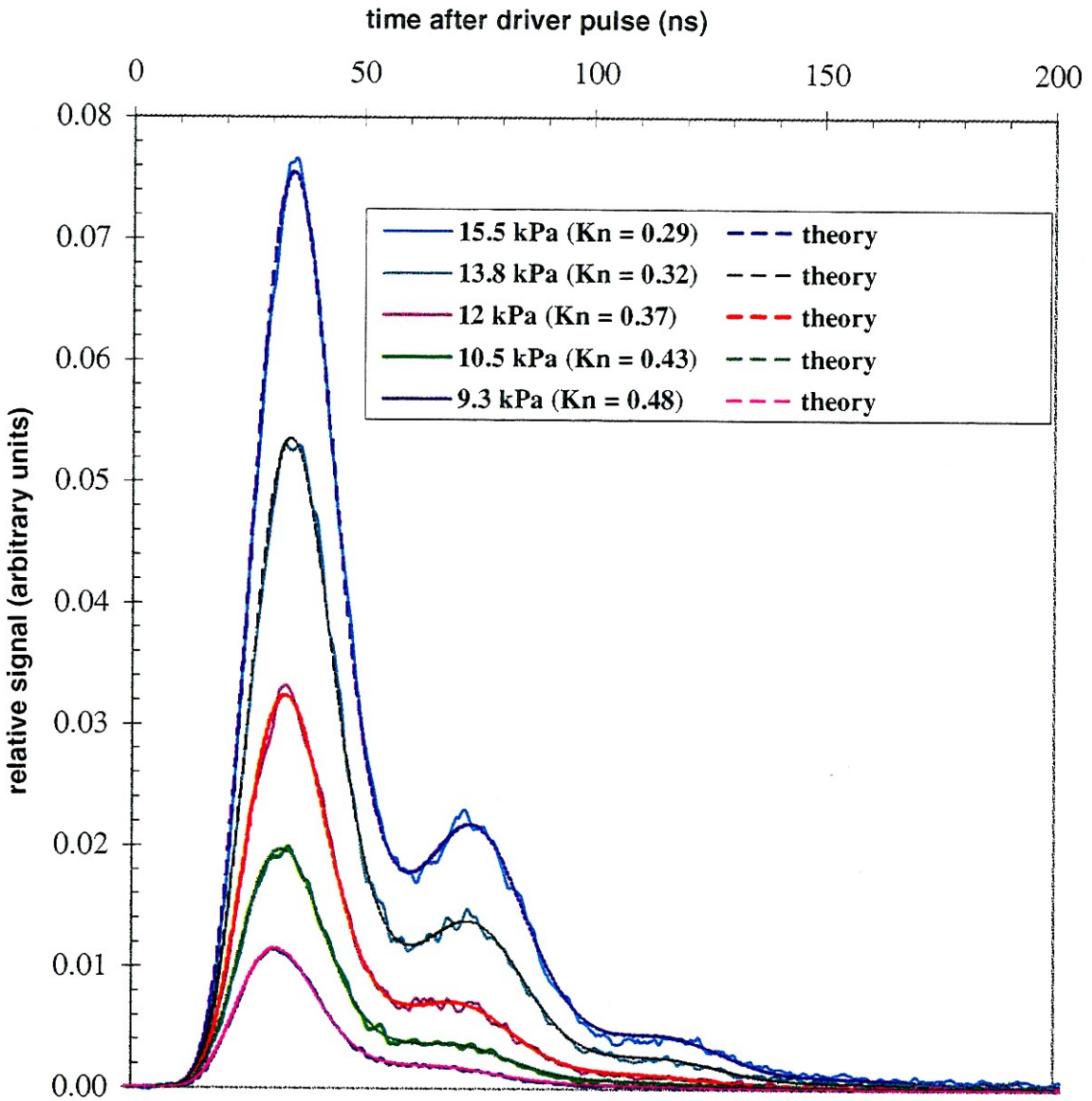

FIG. 11.2. Narrowband LITA signals from low-pressure, NO_2-seeded air at ~300 K.

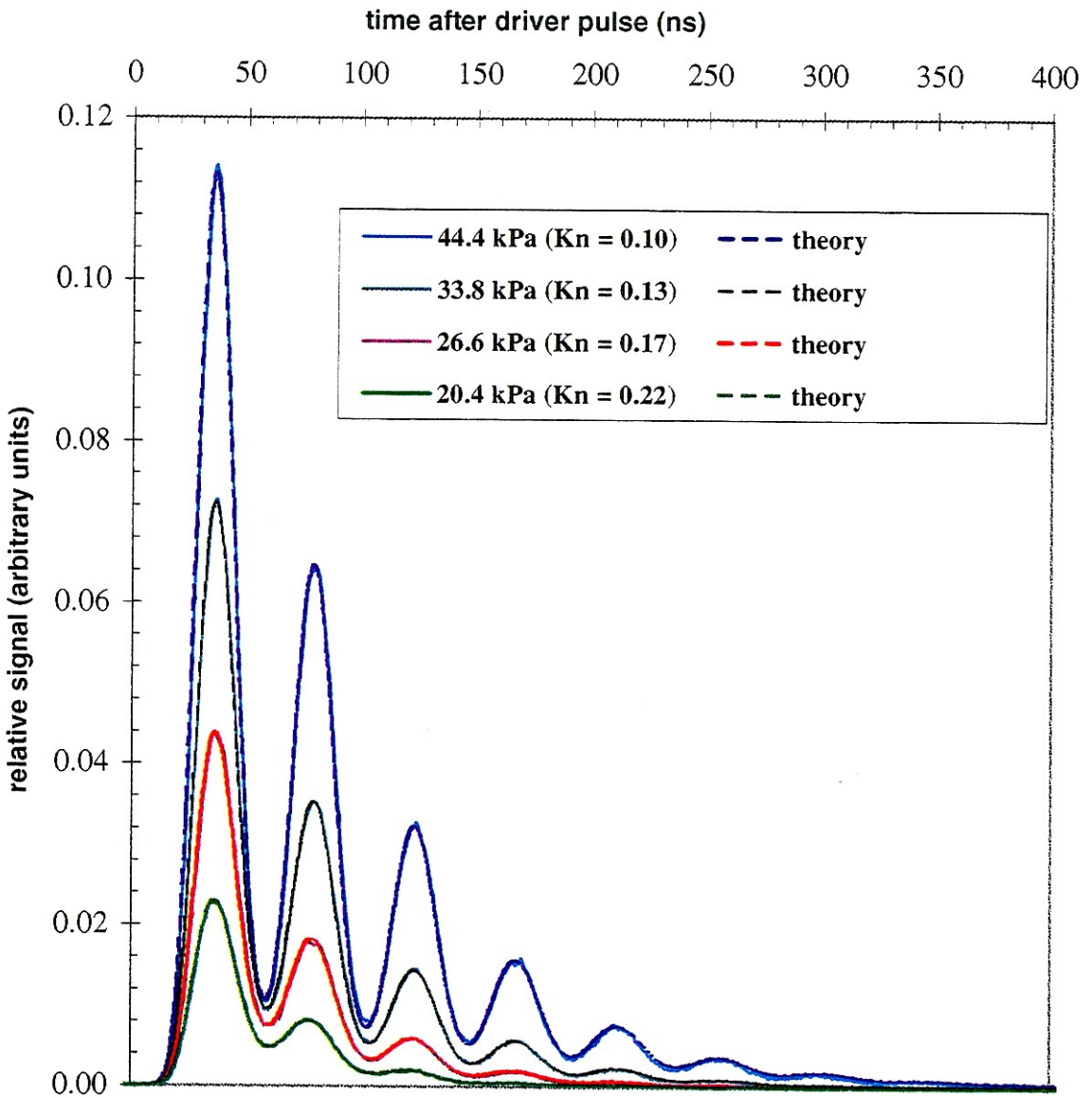

FIG. 11.3. Narrowband LITA signals from NO_2-seeded air near atmospheric pressure and ~300 K.

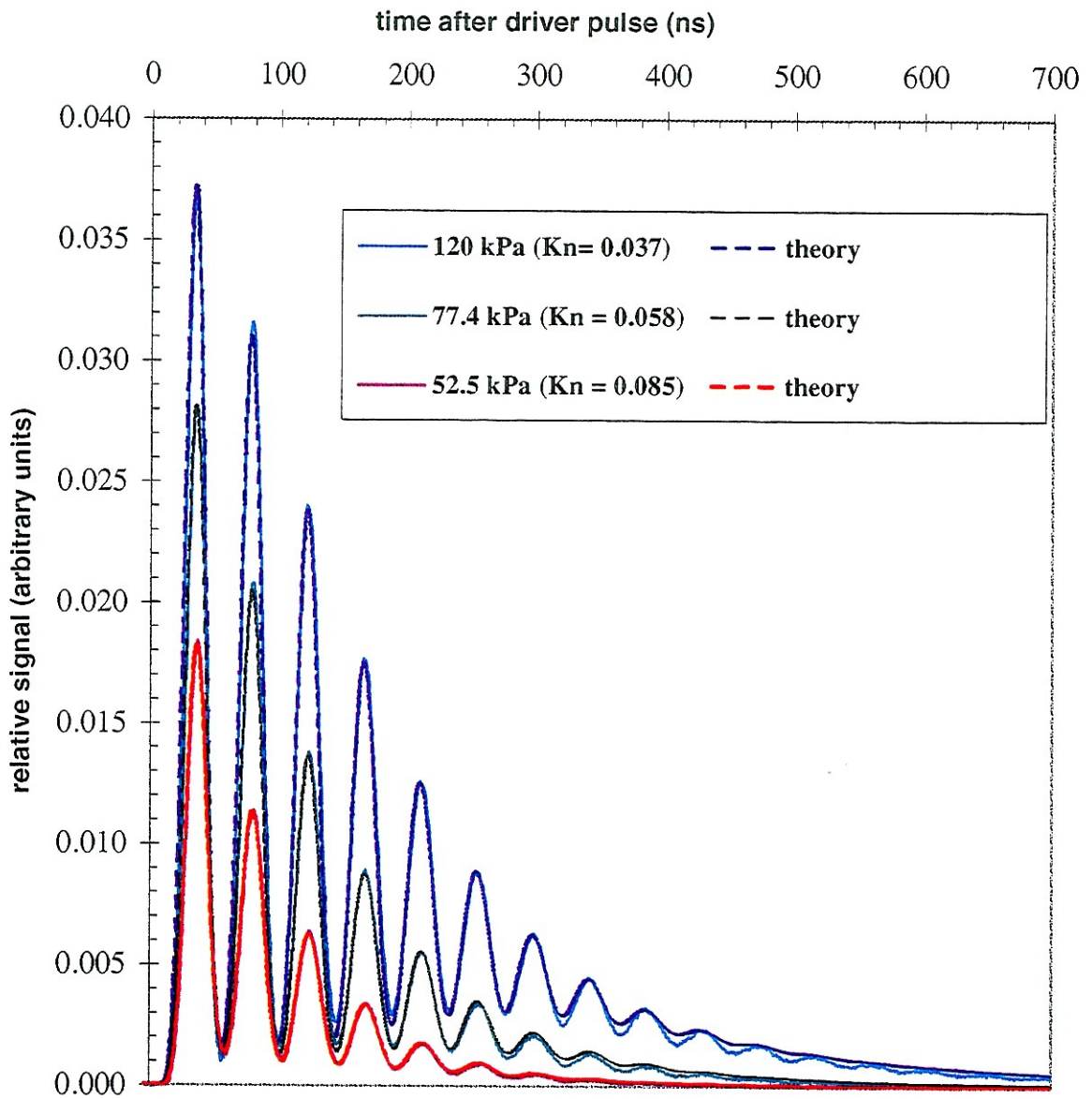

FIG. 11.4. Narrowband LITA signals from NO_2-seeded air above atmospheric pressure, ~300 K.

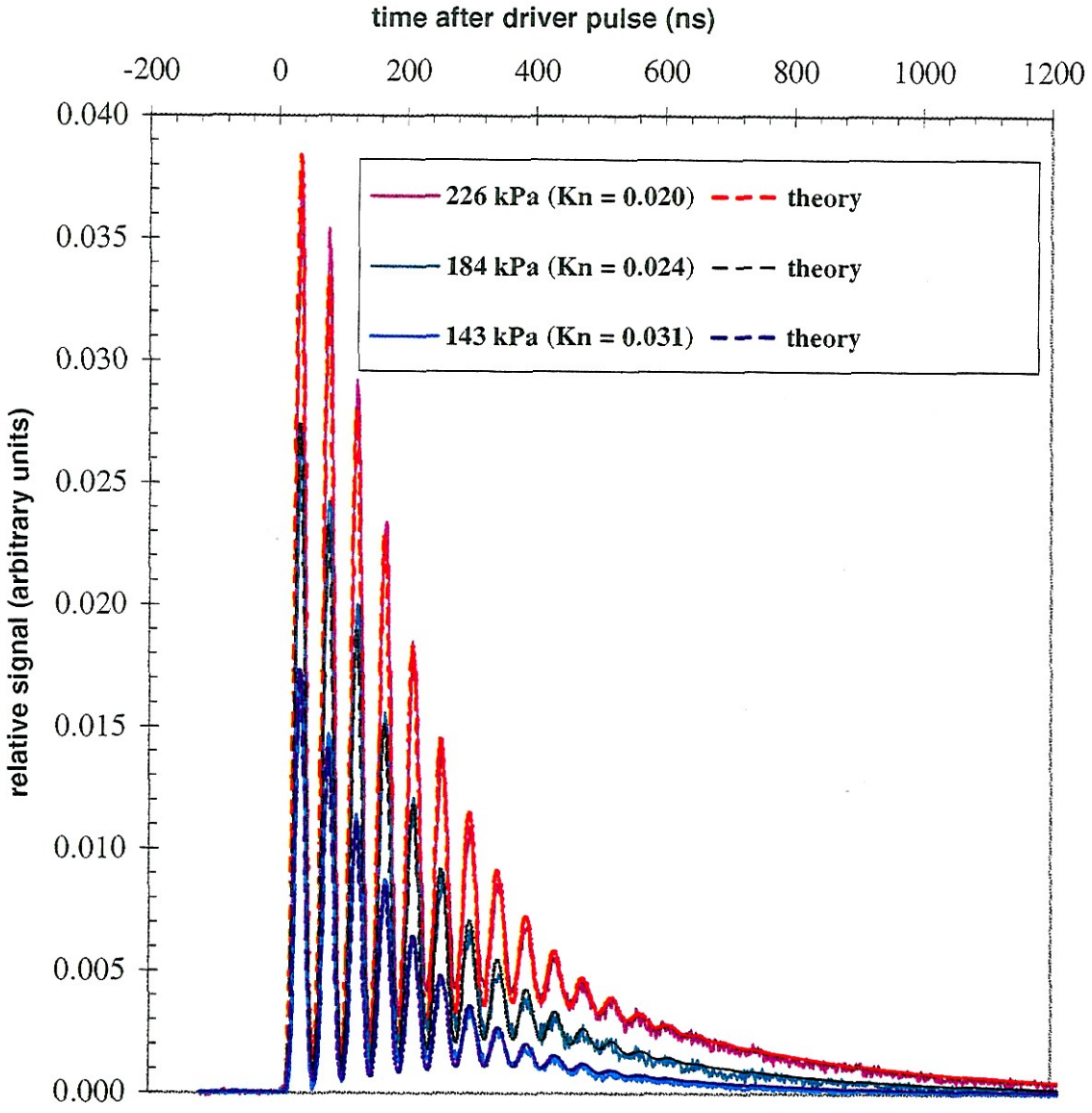

FIG. 11.5. Narrowband LITA signals from NO_2 -seeded air above atmospheric pressure, ~300 K.

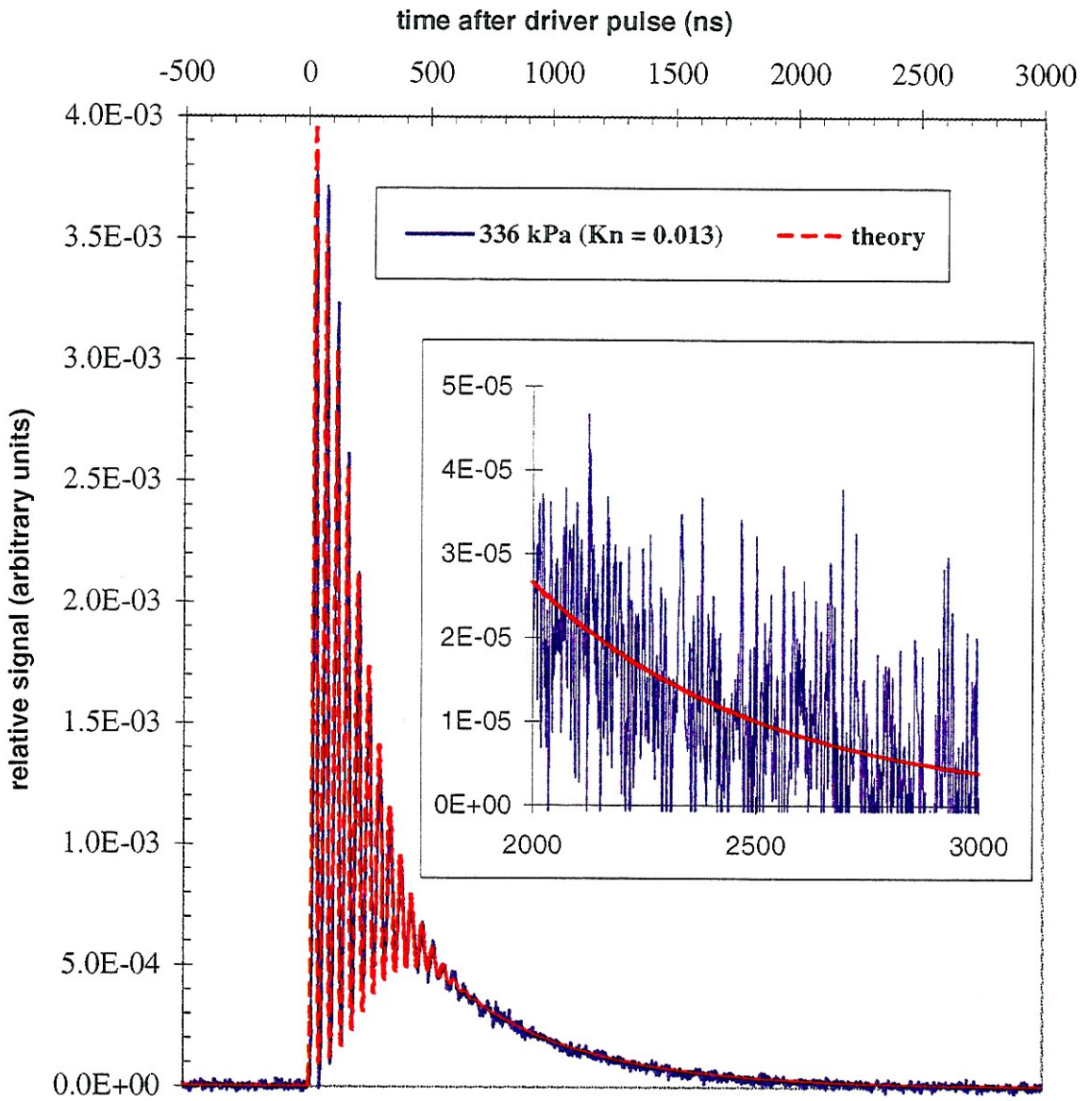

FIG. 11.6. Narrowband LITA signal from NO_2-seeded air at 336 kPa and ~300 K.

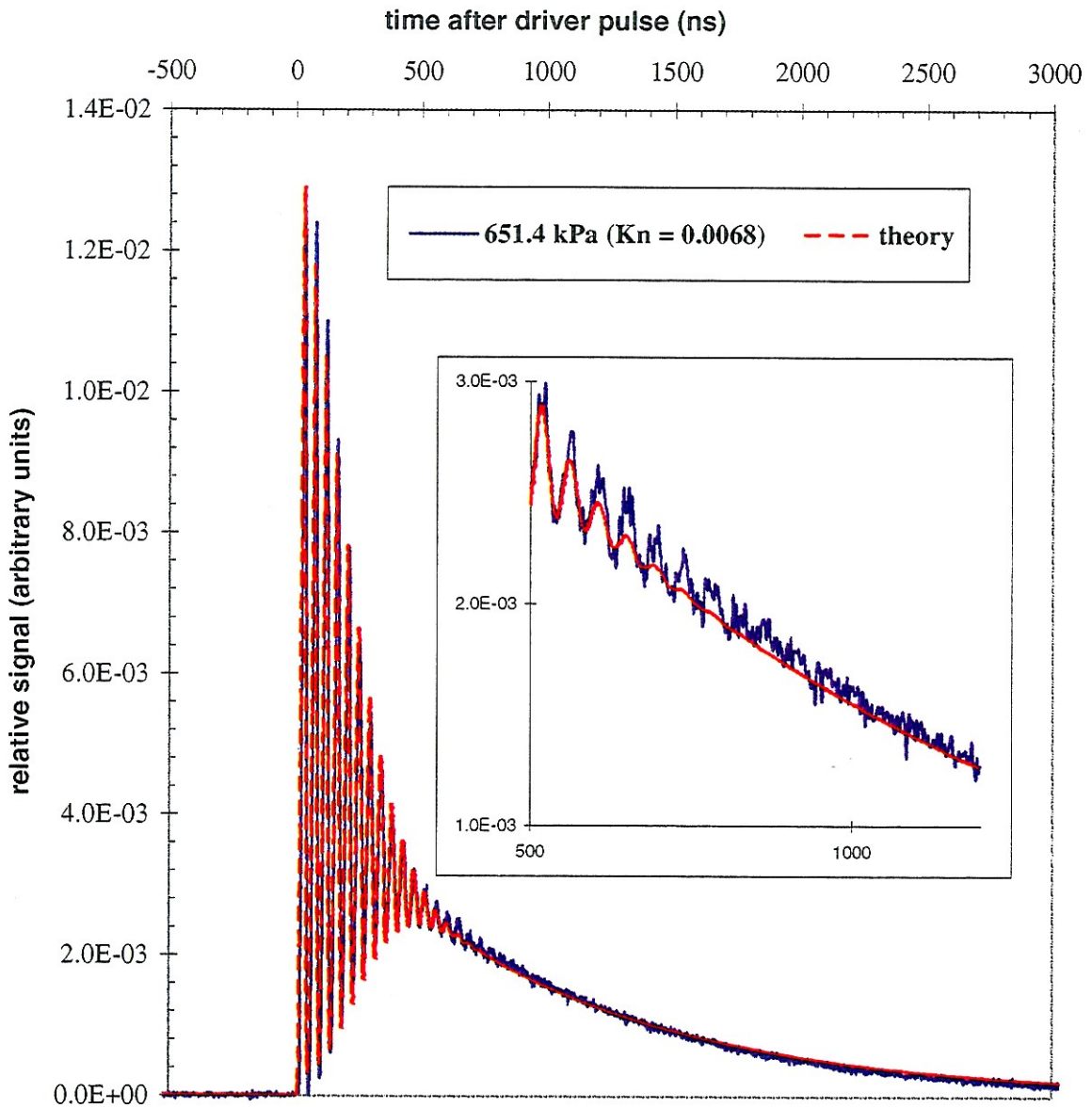

FIG. 11.7. Narrowband LITA signal from NO_2-seeded air at 651.4 kPa and ~300 K.

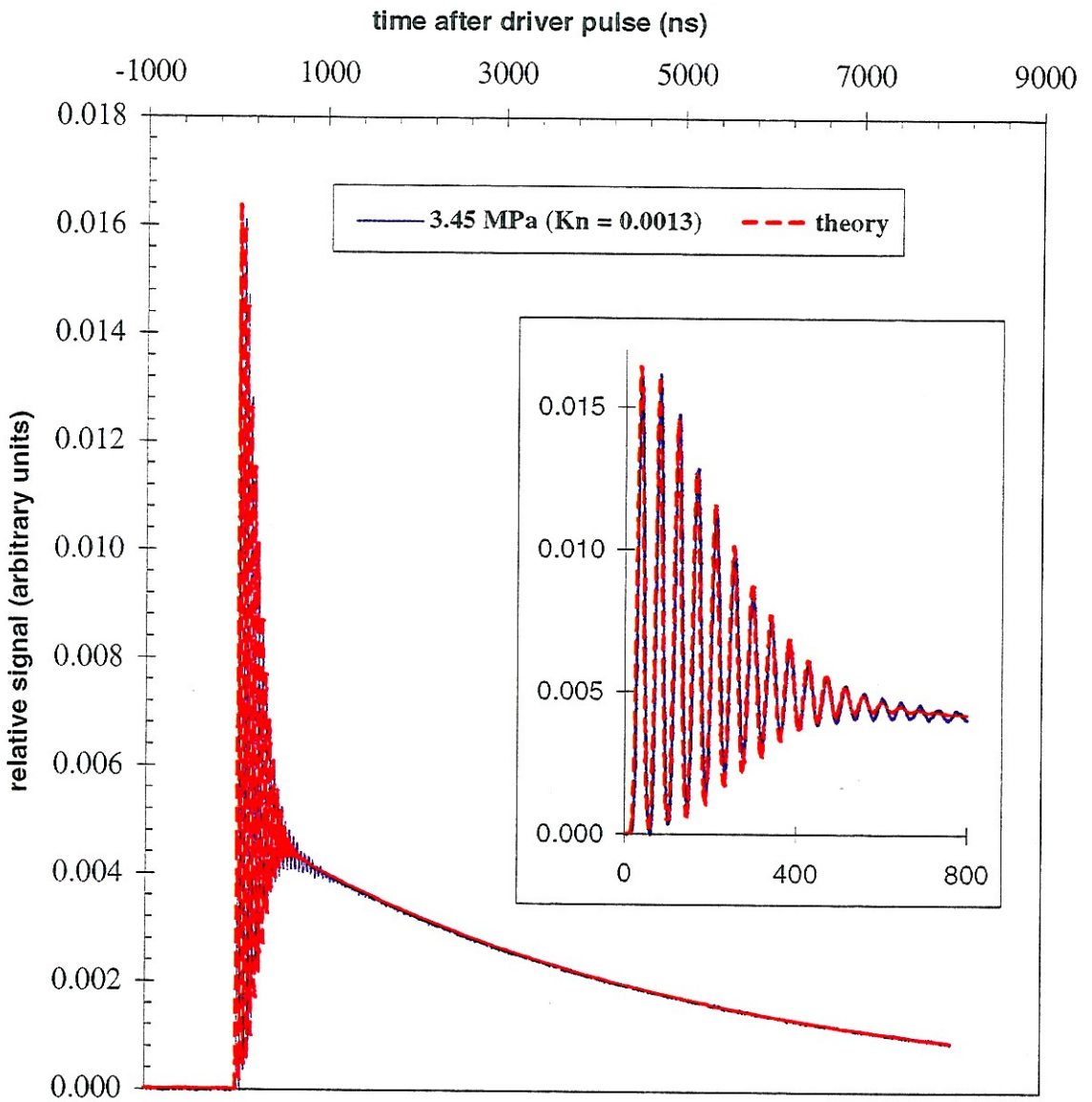

FIG. 11.8. Narrowband LITA signal from NO_2-seeded air at 3.45 MPa and ~300 K.

So far, only thermalization signals have been considered. The model also accurately represents mixed thermalization/electrostriction signals. Electrostriction dominates the signal in Fig. 11.9 taken in NO_2-seeded air at ~14 MPa and 300 K. Unfortunately, the quality of the experimental signal was compromised by an approximately 7% undershoot in the early part of the signal from a signal reflection caused by a faulty cable. This signal defect limits the accuracy of the filtering, but there is clear qualitative agreement between the raw and filtered signal. The same signal defect appears in Fig. 11.10, which features data taken in NO_2-seeded air at ~4.3 MPa and 300 K. This figure shows good agreement in the ringing part (given the signal flaw) and good agreement in the tail shown in the inset figure. Note the scale of the inset figure. The thermal tail in Fig. 11.10 is much weaker than in the purely thermalization-derived signal. Fig. 11.11 shows the signal from CO_2 at atmospheric pressure and ~300 K, with seeding by tank impurities only. Without the undershoot in Fig. 11.9 and Fig. 11.10, the experimental signal agrees much better with the signal filtered using the theoretical model.

The nonlinear filter using the LITA signal model extracts accurate signal parameters and returns reasonable signals, provided systematic experimental error is negligible and the experimental signals have low noise levels. The filter also performs admirably on noisy signals, although with increased uncertainty. Fig. 11.12 shows a single-shot signal taken in room-temperature air and trace NO_2 at 295 kPa. The raw signal is seriously degraded by shot noise and mode/plasma noise of the source laser. The automatically filtered signal appears in red. The extracted values of the thermal diffusivity (accuracy ~20%) and sound speed (accuracy ~1%) were more accurate than the initial guesses (~50% and ~10%, respectively). This result is typical provided the initial guesses are sufficiently accurate. Single-shot signals are not always this noisy, particularly at high pressures and higher seed-gas concentrations. At these conditions, the noise is dominated by source-laser and system noise, which is of much lower amplitude than the shot noise in Fig. 11.12. Fig. 11.13 shows a single-shot signal taken in air at ~14 MPa with trace NO_2. Electrostriction is the dominant opto-acoustic effect in the signal.

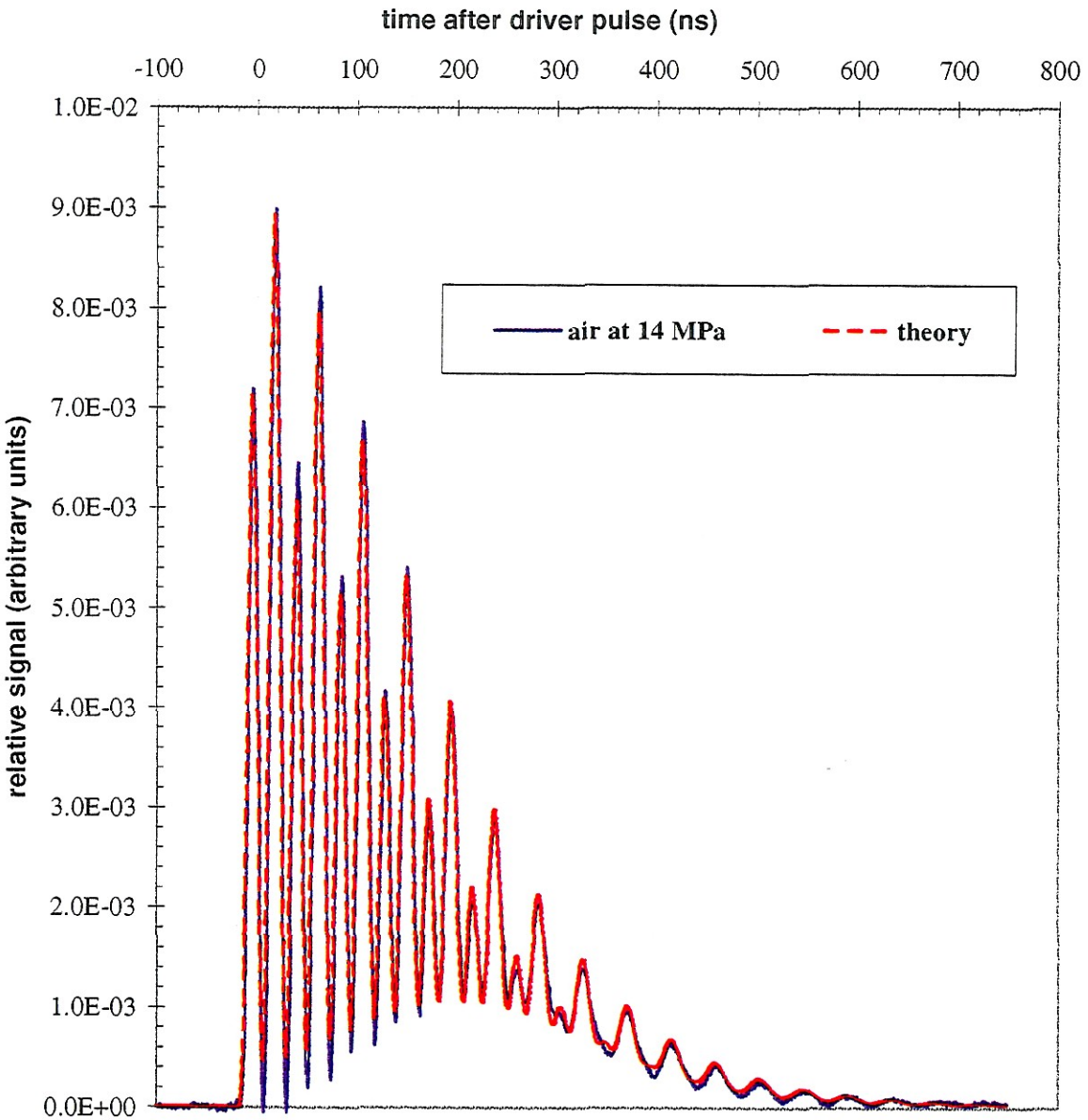

FIG. 11.9. Narrowband LITA signals from electrostriction and thermalization in NO_2-seeded air at ~14 MPa and 300 K.

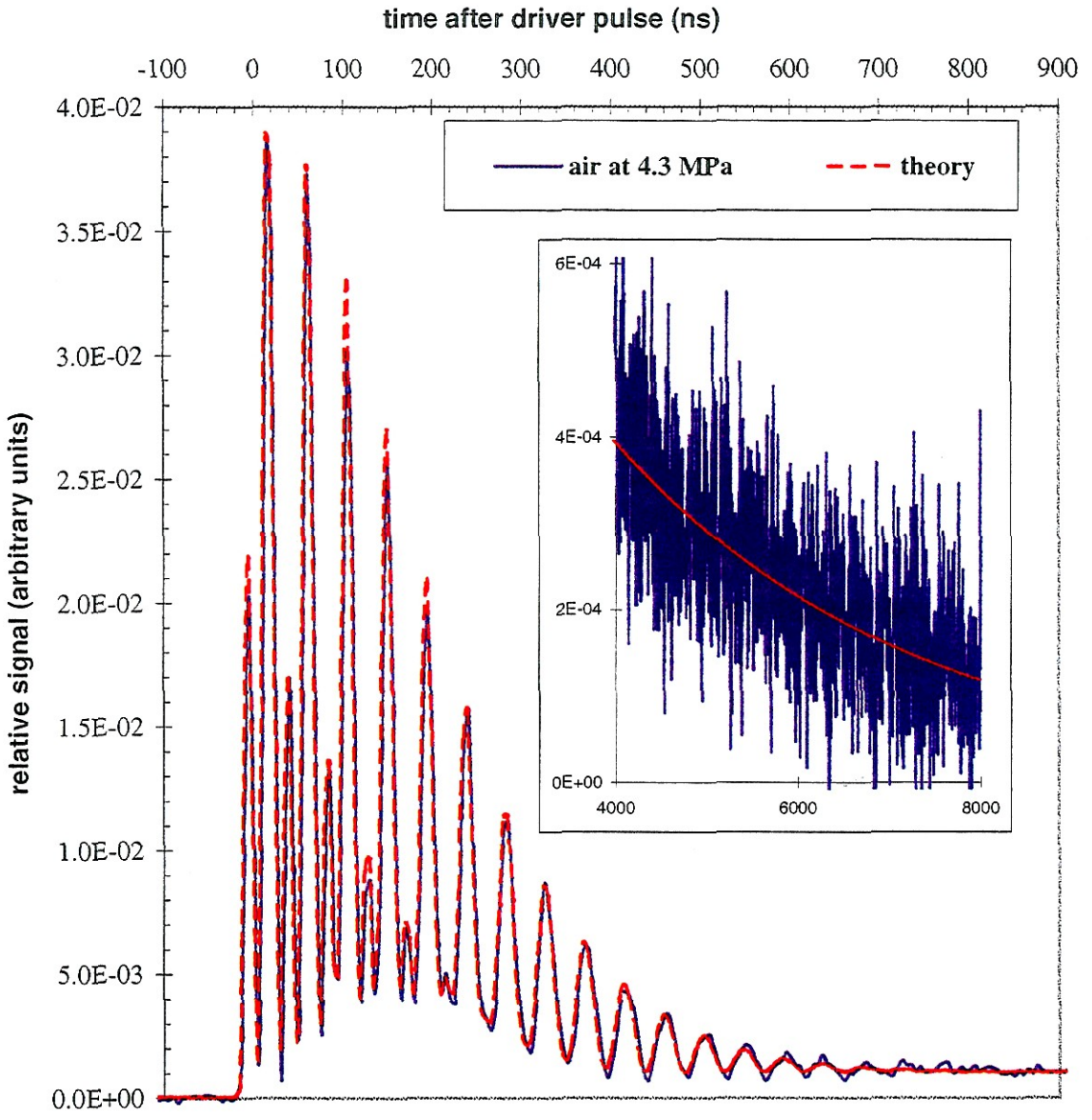

FIG. 11.10. Narrowband LITA signals from electrostriction and thermalization in NO_2-seeded air at ~4.3 MPa and 300 K.

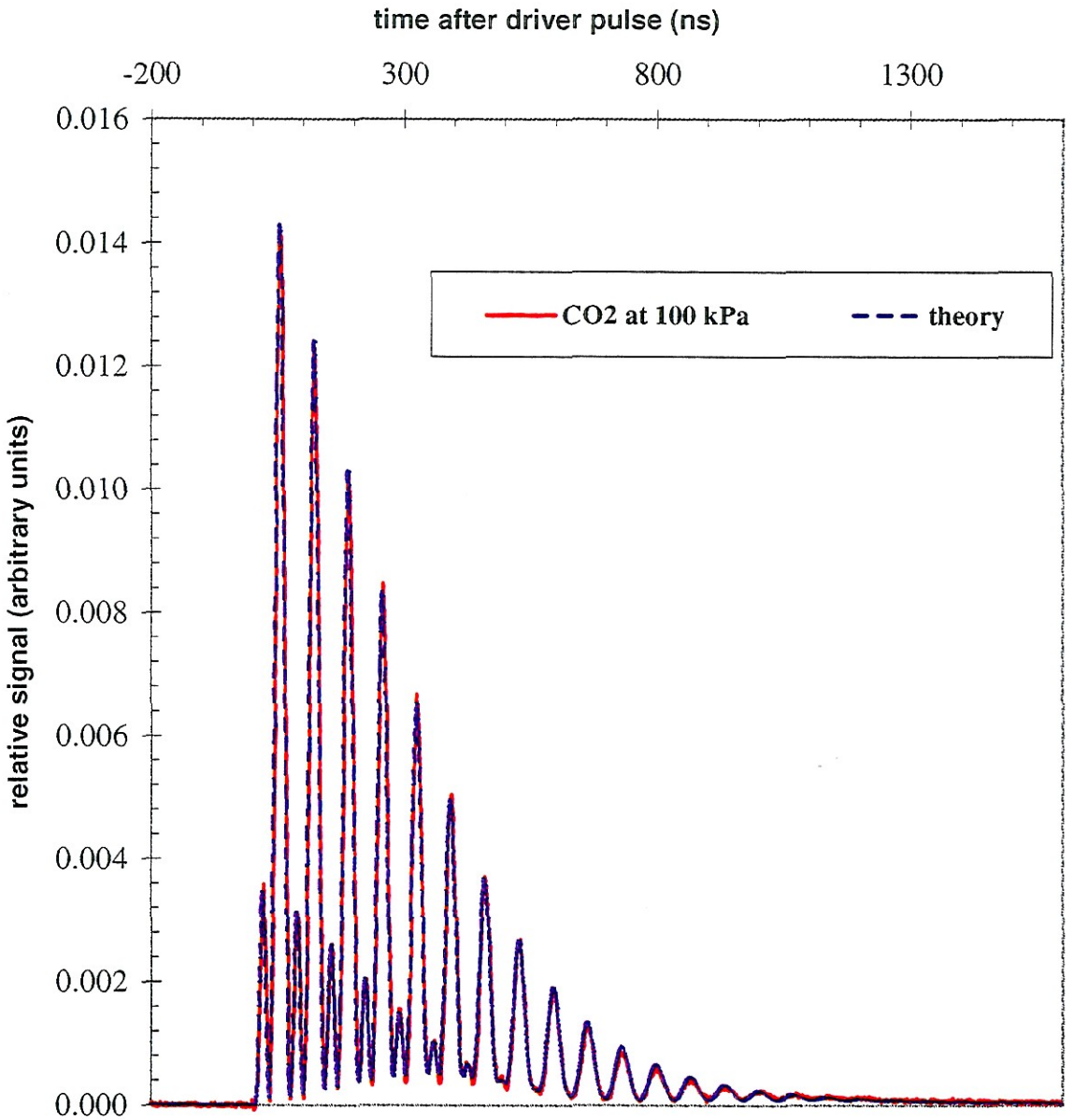

FIG. 11.11. Narrowband LITA signals from electrostriction and thermalization in atmospheric-pressure CO_2 at ~300 K.

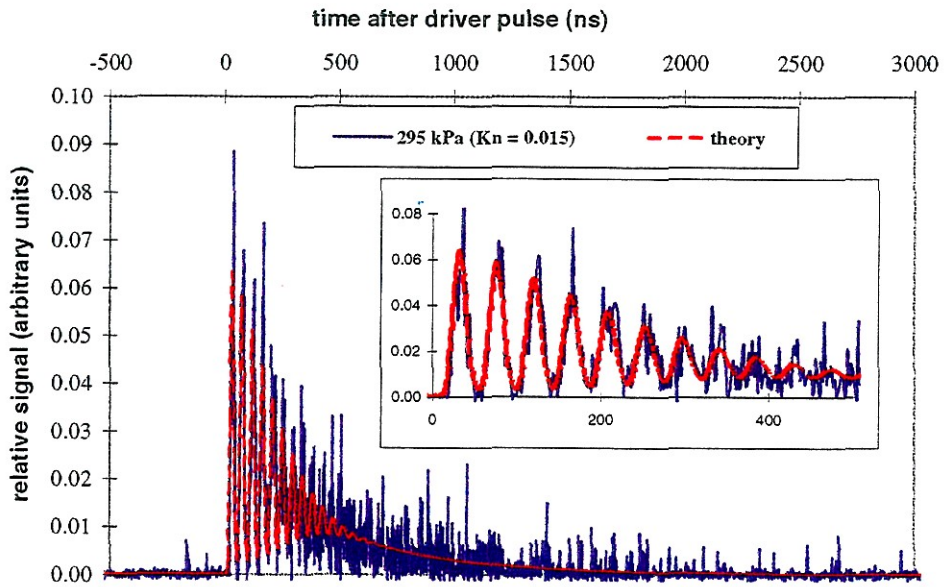

FIG. 11.12. Single-shot narrowband LITA signal from thermalization in NO_2-seeded air at 295 kPa and ~300 K.

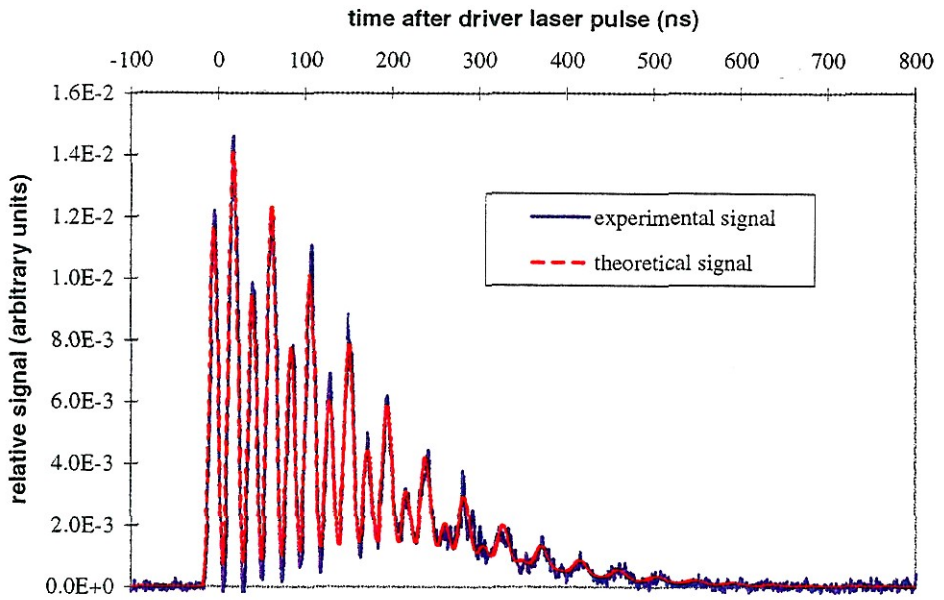

FIG. 11.13. Single-shot narrowband LITA signals from both electrostriction and thermalization in NO_2-seeded air at ~14 MPa and ~300 K.

11.2 The Effects of Driver Laser Tuning

An interesting dependence of the LITA signal on driver-laser frequency was observed in tests performed using laboratory air. The behavior was caused by spectral structure in the gas susceptibility from NO_2 that was present in the air in quantities less than 50 parts-per-billion according to the Southern California Air-Quality Management District, which monitors atmospheric pollutants. Because electrostriction and thermalization depend upon different components of the susceptibility, the relative contribution to the signals from each effect changes as the driver laser frequency is tuned across spectral lines or structure. Fig. 11.14 sketches this effect for a hypothetical isolated transition. When the driver laser frequency is far from the transition (*a*), the signal arises predominantly from nonresonant electrostriction. The signal oscillates at twice the Brillouin frequency because of Doppler beating between light scattered by the counterpropagating acoustic wavepackets. Near the transition frequency the real part of the susceptibility attains a maximum (*b*). The electrostrictive contribution to the signal increases. A "staircase" pattern emerges in which every other peak is enhanced. The increase in these peaks arises from a component of the signal at the Brillouin frequency, caused Doppler beating between signals scattered by the acoustic waves and (stationary) thermal grating. At the peak of the absorption (*c*), the signal arises nearly entirely from thermalization. The electrostrictive peaks return to their nonresonant level. At a slightly higher frequency (*d*), the real part of the susceptibility is nulled. The signal arises entirely from thermalization, as it does at point *f*. At *e*, there is a slight return of electrostriction peaks.

A dependence of the LITA signal on driver laser frequency like that shown in Fig. 11.14 was observed in LITA signals from the laboratory air (Cummings, 1993), evidently caused by spectral lines of the trace pollutant NO_2. Initial tests to record a signal spectrum with driver-laser tuning crudely illustrated the modulation of the signals from resonant and non-resonant electrostriction and thermalization. More recently, tests were performed with much better spectral resolution. The susceptibility spectrum thus measured appears in Fig. 11.15. This spectrum was recorded by manually stepping the driver laser tuning by an average of ~2 GHz (~0.06 cm^{-1}), recording 100-shot averages of the narrowband LITA signal, and extracting signal parameters

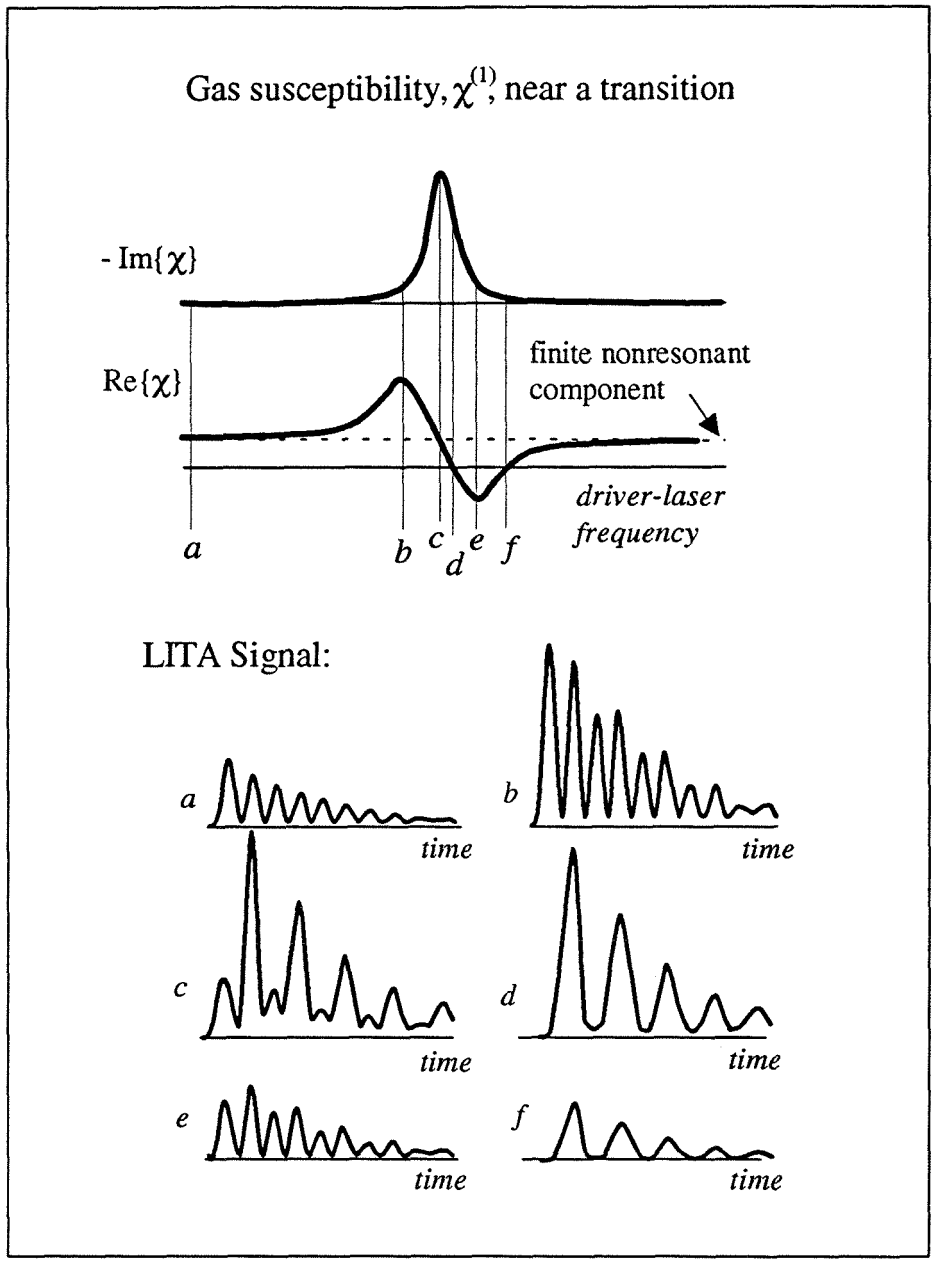

FIG. 11.14. LITA signal (sketch) versus driver laser tuning. Electrostriction, proportional to $\mathrm{Re}\{\chi(\omega_d)\}$, produces a signal modulated at twice the Brillouin frequency. Thermalization, proportional to $-\mathrm{Im}\{\chi(\omega_d)\}$, produces a signal modulated at the Brillouin frequency.

including the relative real and imaginary parts of the susceptibility using the nonlinear filter. The wavelength of the laser was monitored using the high-resolution spectrometer described in Chapter 9. Despite the crudeness of the manual recording technique, the resulting spectrum shows with remarkable fidelity (a signal-to-noise ratio of > 100) weak rotational spectral lines of NO_2. The amount of NO_2 in the sam-

ple volume during these tests was $\sim 10^{-15}$ gram, demonstrating that this technique is certainly among the most sensitive and is perhaps the most sensitive spectroscopic technique in gases at atmospheric-pressure and above. The resonant modulation of the real part of the susceptibility is ~15% of the nonresonant part. This degree of modulation is about one-tenth that observed in the original tests, corresponding to lower levels of NO_2 in the air.[‡] A system for automating the laser scanning, and data recording is being considered so that extended spectral surveys may be taken.

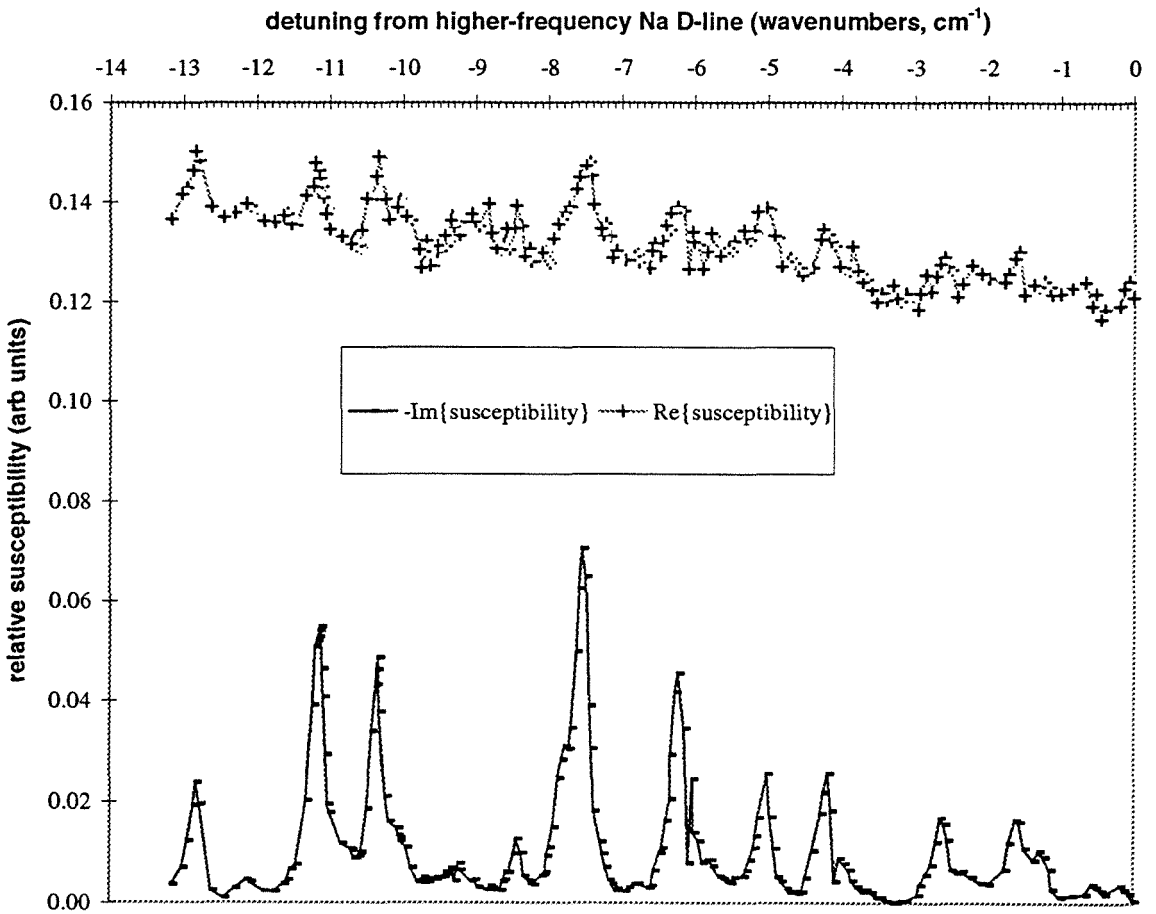

FIG. 11.15. Real and imaginary susceptibility spectra of laboratory air taken using driver-laser frequency scanning. About 400 GHz of the spectral region near the lower-frequency sodium D-line is covered in these spectra. Trace NO_2 pollutants cause the line structure.

Fig. 11.15 shows a peculiarity that has not yet been resolved. The spectral structure of the real part of the susceptibility follows that of the imaginary part, not as

[‡] The rain shortly before the tests may be to blame (!).

shown in Fig. 11.14. The reason for this is not yet clear. It is possible that the structure is genuine, given the complicated nature of the overlapping spectral lines that are evident. If the structure is not genuine, it could be the result of the finite bandwidth of the driver laser beam. Electrostriction and thermalization are respectively proportional to the real and imaginary parts of the susceptibility only for driving with monochromatic, degenerate beams. The dependence of the optoacoustic effects on susceptibility is more complicated when the driver-beams have finite bandwidths.

11.3 Pressure Dependence of Signals

Knowledge of the pressure and resonant-species concentration dependence of the magnitude of LITA signals can assist in the analysis of experimental feasibility. In addition, this knowledge may permit the estimation of pressure and species concentration from absolute and relative signal intensity measurements. The LITA-signal model predicts the absolute signals and therefore any such dependence on pressure and concentration, given knowledge of the susceptibility spectrum. However, experiments presented here used gas mixtures whose resonant species is NO_2, whose spectral properties are not well established. The reasons for using NO_2 include its abundance of visible-frequency transitions and its status as a major pollutant (the brown color in smog). Because of its health risks, atmospheric NO_2 concentrations are independently measured by the Southern California Air-Quality Management District. These independent measurements and the trace levels in atmospheric air in Pasadena obviate the use of successive dilution, a technique fraught with error, to obtain low NO_2 concentrations. Unfortunately, the spectroscopy of NO_2 is complicated. The details of the spectrum of NO_2 are not readily calculated. Eq. B.1 therefore is not a good predictor of absolute signal intensities with current knowledge of the properties of NO_2. The abundance of spectral lines of NO_2 may actually simplify the prediction of the pressure exponents of LITA signals at elevated pressures. At high pressures, collisions reduce the lifetime of excited states of NO_2 so much that the homogeneous width of the spectral lines, i.e., that caused by the finite lifetimes of the upper states, exceeds the spacing of the lines. The spectrum is "smoothed" out and does not change appreciably as the pressure is increased. The pressure at which this smoothing begins depends upon the buffer gas and the spectral location. In the spectral region studied in these experiments, this "smoothing" evidently occurred near atmospheric pressure, although it is clear from Fig. 11.15 that this conclusion is not generally valid.

The gas susceptibility is approximately proportional to the density above the "smoothing" pressure and at constant seed-gas concentration. If thermalization rates are fast compared to other LITA time-scales, the intensity of the signals at constant NO_2 concentration is therefore proportional to the square of the density of the gas. At constant temperature, this corresponds to signals with a square dependence on

pressure of the peak signal intensity. Fig. 11.16 through Fig. 11.19 demonstrate this trend in air, He, and CO_2.

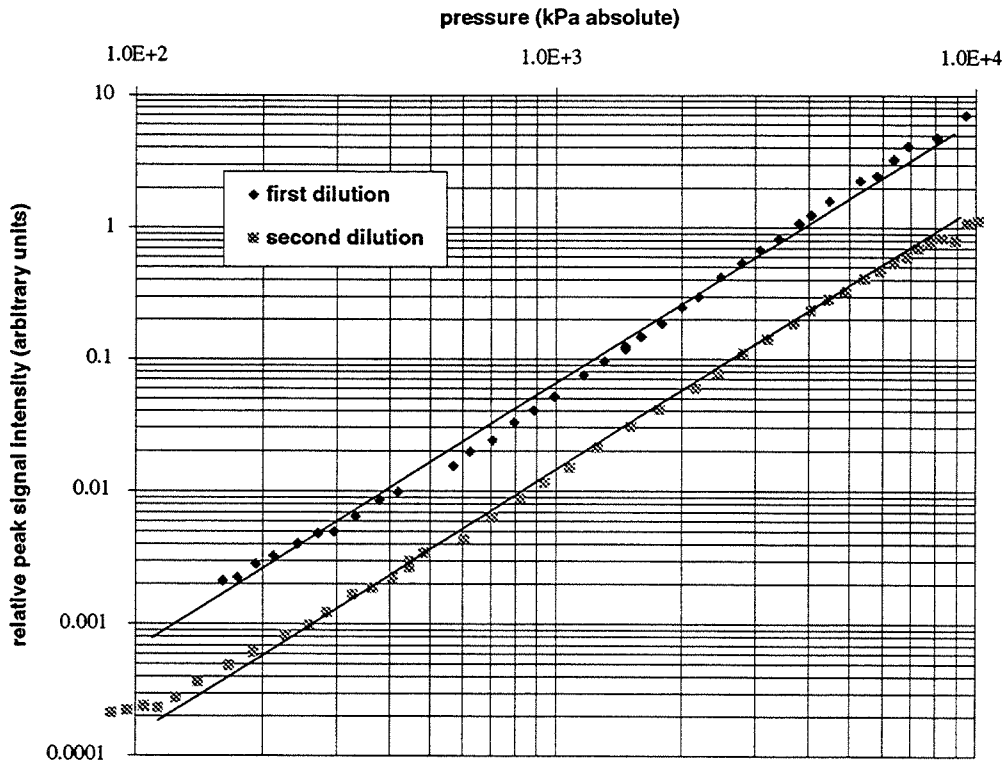

FIG. 11.16. Peak narrowband LITA signal from thermalization as a function of air pressure at constant trace NO_2 concentration. The signal level between curves drops because of successive dilution of the NO_2. The solid lines represent quadratic pressure dependence.

The species concentration dependence of LITA signal intensities depends upon the experimental arrangement. The analysis predicts the intensity of the signal to vary according to the relation

$$\mathcal{L} \propto |\chi^{(1)}(\omega_d)|^2 |\chi^{(1)}(\omega_o)|^2,$$

ignoring the details of thermalization and electrostriction. By tuning the driver and source laser independently, quartic and quadratic dependence of signal intensity on species concentration of abundant species may be obtained. A signal contribution that is linear in species concentration may be achieved for trace species in the presence of a nonresonant background. A low-order dependence on species concentration is the key to the sensitivity of LITA for trace species. A high-order dependence on species

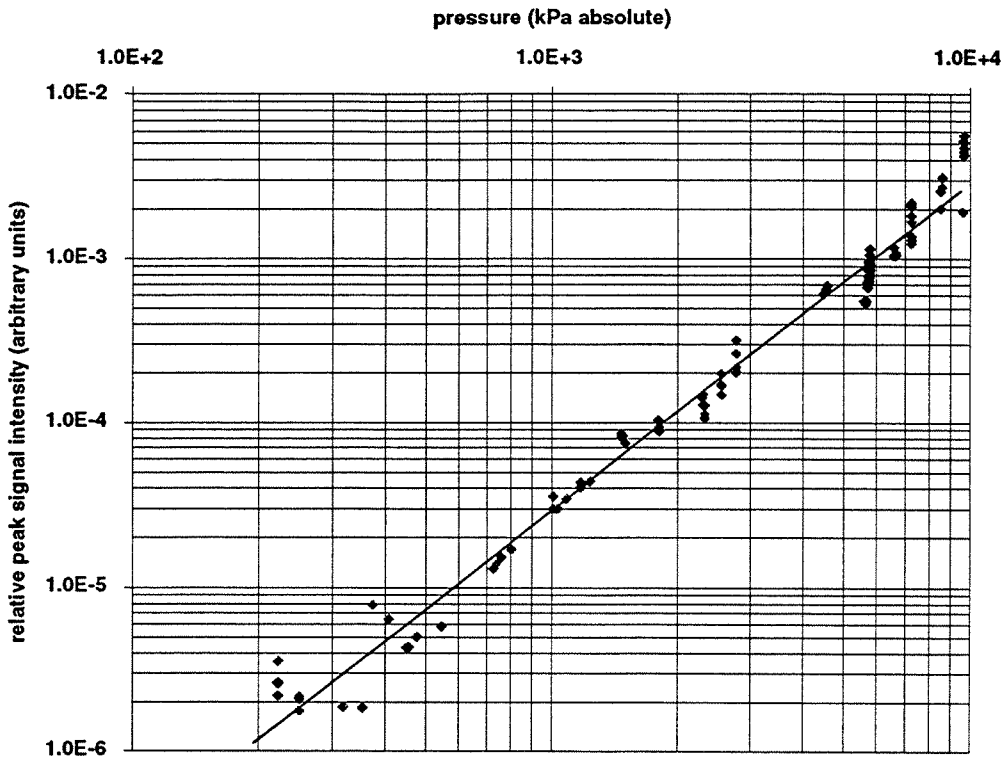

FIG. 11.17. Peak narrowband LITA signal from electrostriction as a function of (unseeded) air pressure. The solid line represents quadratic pressure dependence.

concentration is the key to obtaining strong signals in heavily-seeded gases or gases with high levels of indigenous target species. However, the high number densities of resonant species required to observe quartic signal dependence on concentration in a gas with a high nonresonant susceptibility may cause excessive absorption of the source and signal beams. Thus the quartic signal dependence may not be observable in general.

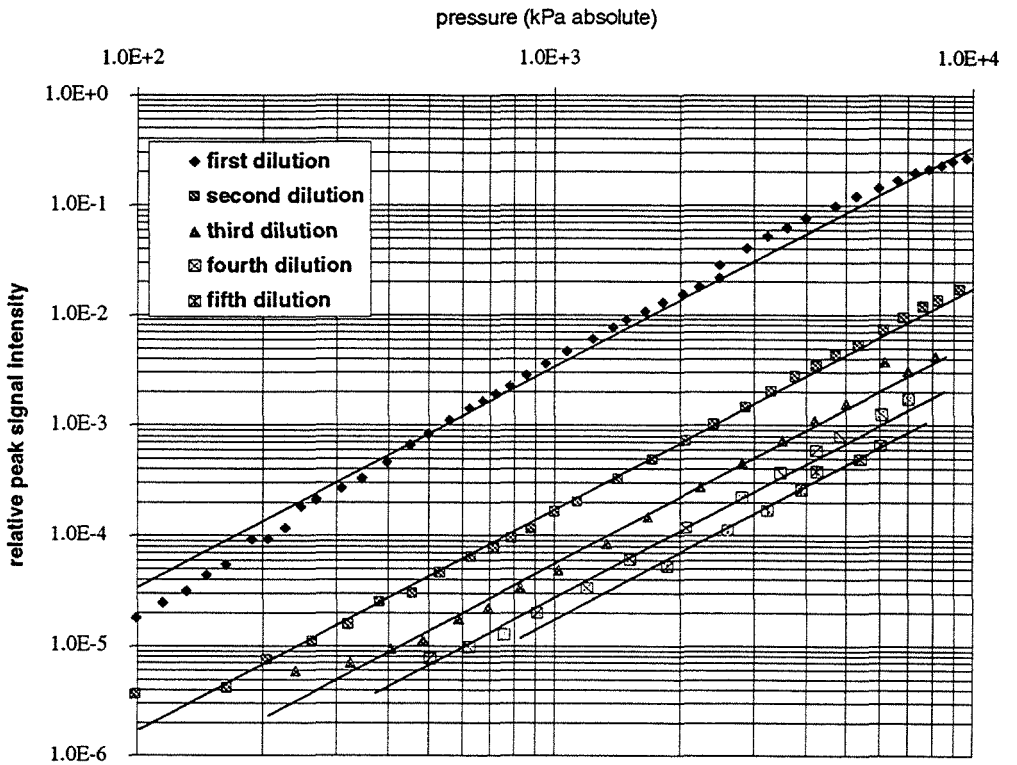

FIG. 11.18. Peak narrowband LITA signal from thermalization as a function of helium pressure at constant NO_2 concentration. The signal level between curves drops because of successive dilution of the NO_2. The solid lines represent quadratic pressure dependence.

11.4 Gas Property Measurements

Narrowband LITA is expected to become a tool for the measurement of gas properties. A series of narrowband experiments evaluated the potential accuracy and practicality of LITA for these measurements. From low-noise signals, sound-speed measurements were typically of the order 0.1% uncertain.* When beam alignment was precise, thermal diffusivity measurements were ~1% uncertain. However, even slight beam misalignment (displacement by small fractions of the beam diameters) seriously degraded these transport property measurements. This degradation arises because the nonlinear filter treats the signal globally, which is of tremendous advantage when the filter model is correct, as in the case of well-aligned beams. However, slight beam misalignment changes the envelope of the signal subtly. The filter responds by skewing the signal parameters until the theoretical "pure" signal matches

* This uncertainty may well have been caused by temperature uncertainty in the test gas. The uncertainty estimates from the filtering routine, which assumed a normal distribution of errors, were typically two or three orders of magnitude lower.

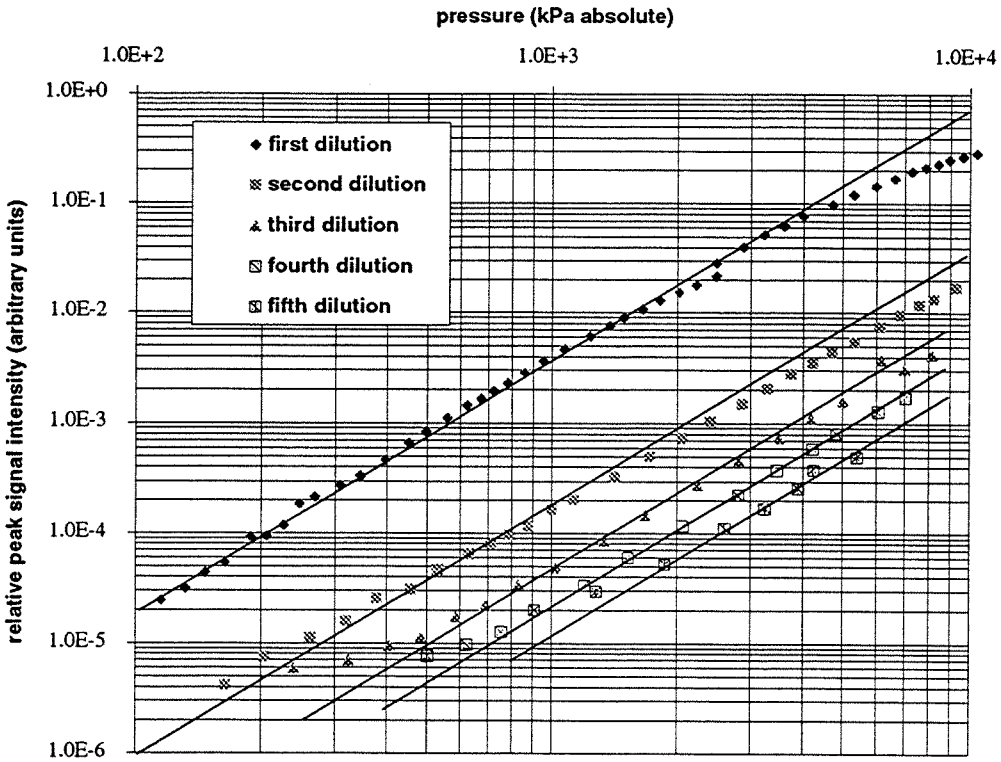

FIG. 11.19. Peak narrowband LITA signal from thermalization as a function of CO_2 pressure at constant NO_2 concentration. The signal level between curves drops because of successive dilution of the NO_2. The solid lines represent quadratic pressure dependence.

the experimental "flawed" signal in an average sense. The skewing of the thermal diffusivity can be ~30% in particularly bad cases. The average uncertainty in thermal diffusivity measurements caused by beam misalignment was ~10–20% in these tests. This problem may be addressed in several ways that are discussed later. Acoustic damping rate measurements were sensitive to beam misalignment and severely degraded by finite-beam-size effects at high pressure. The practicality of the technique for single-shot measurement hinges upon mitigating the effects of beam misalignment, discussed in Sec. 11.7.1, and obtaining sufficiently strong signals.

In the discussion of the results of LITA measurements, the term accuracy is used to describe agreement of the *calibrated* experimental measurements with published, independent experimental values. The term precision is used as a measure of the uncertainty in the measured values, usually estimated by comparing separate measurements taken at similar conditions.

11.4.1 Air

LITA has been performed on atmospheric air, "pure" air from a dry-air bottle, and NO_2-seeded air up to NO_2 partial pressures of ~10 torr. Above this partial pressure of NO_2, absorption of the source and signal beams is severe enough to impede measurement. LITA data from atmospheric air has been taken using NO_2 concentrations less than 50 parts-per-billion. Sound-speed measurement in air using LITA has been performed with ~0.1% accuracy at pressures above ~100 kPa. The accuracy of the measurements below atmospheric pressure is reduced because of finite Knudsen number effects. The precision of these measurements is also degraded by noise and high acoustic damping rates. Fig. 11.21 shows the sound speed extracted from the filtered signals from 0.1–100 atmospheres of air pressure, with NO_2 seeding in the 10 parts-per-million range. Each vertical division is 0.1%. The (systematic) deviation of the sound speed at the lower pressures is ~5% at 20 kPa (Kn ~ 0.22), while the precision is evidently of the order 1%. The measurements are normalized to their values at atmospheric pressure since the determination of *absolute* sound speeds either requires impractically accurate measurement of the beam-crossing angle (0.1% accuracy requires 12 μrad accuracy) or calibration using a gas of known sound speed. Because the system is calibrated using gas properties at atmospheric pressure,** no information is lost in the normalization. The measurements cited in Hilsenrath et al., (1955), are plotted as solid circles. There is agreement generally within 0.1% between these results. It is questionable whether the data of Hilsenrath et al., is more accurate than the LITA data. Disagreement may in part be caused by by differences in the gas composition. Fig. 11.20 shows data from successive pressure surveys conducted by alternately filling the bomb at constant NO_2 partial pressure and draining the bomb at constant NO_2 concentration. The strength of the signals varies over approximately seven orders of magnitude over the range of pressures/seed concentrations. The inaccuracy of the measurements at lower NO_2 concentrations is caused by noise.

Fig. 11.22 shows the variation of the measured thermal diffusivity of air with pressure. The thermal diffusivity is roughly inversely proportional to pressure. The

** More precisely, the system is calibrated by extrapolating an estimate of the sound speed at one atmosphere from data at higher pressure, since, even at atmospheric pressure, finite Knudsen number effects artificially increase the sound speed above the precision of the measurements.

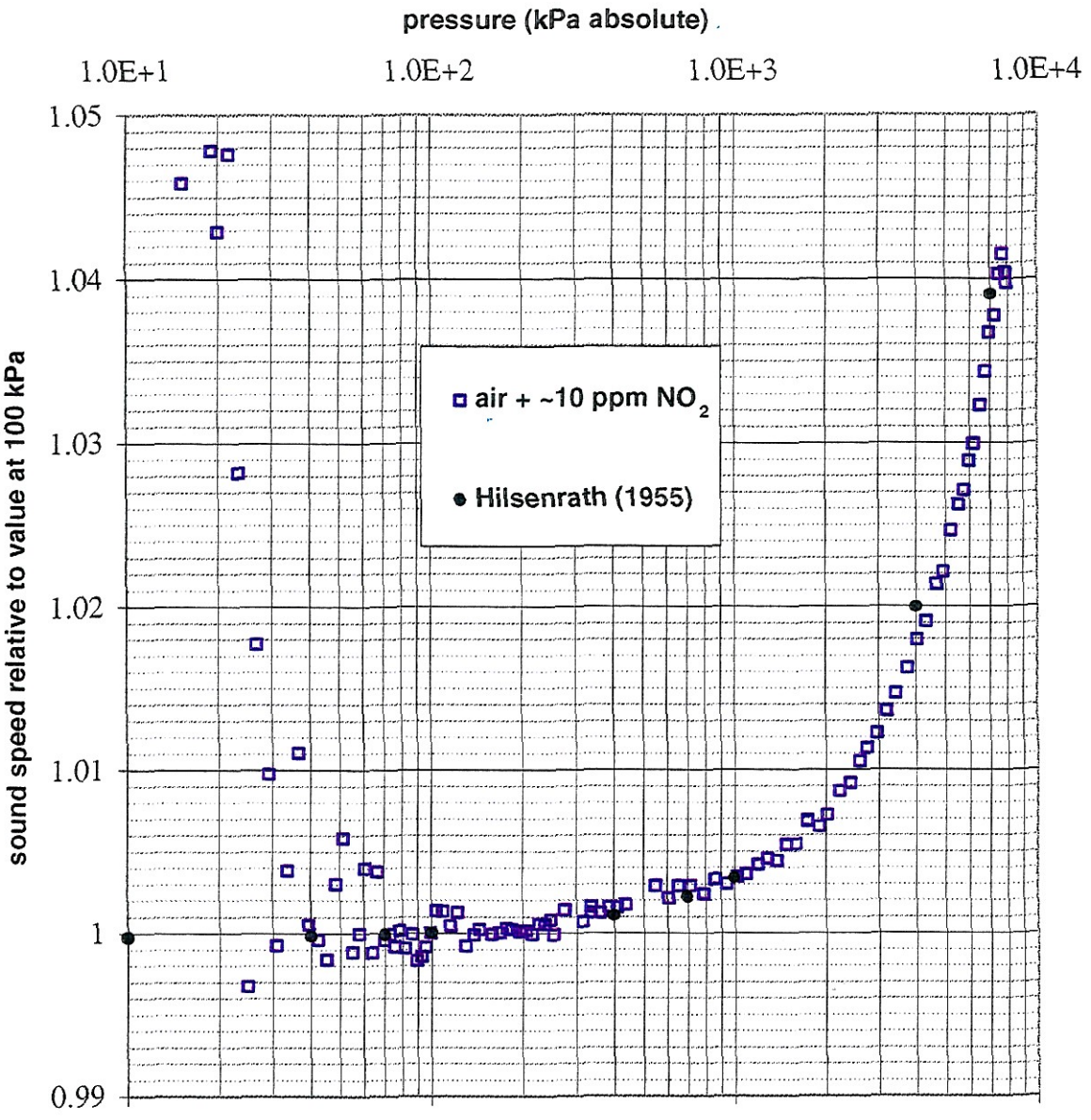

FIG. 11.20. Variation of the measured sound speed of air with pressure. The solid circles are independent published measurements from the National Bureau of Standards. The systematic increase in the measured sound speed at low pressures is a finite Knudsen number effect.

thermal conductivity, a quantity derived from the thermal diffusivity is roughly constant with pressure, slightly increasing at high pressures. Measurements of thermal conductivity taken in two separate tests are over-plotted in Fig. 11.23. Independent measurements from Vargaftik et al., (1994) are over-plotted as solid circles. The internal inconsistency of the extracted properties is of the order 25%, much higher than is explained by experimental uncertainty. The nonlinear filtering skewed the extracted

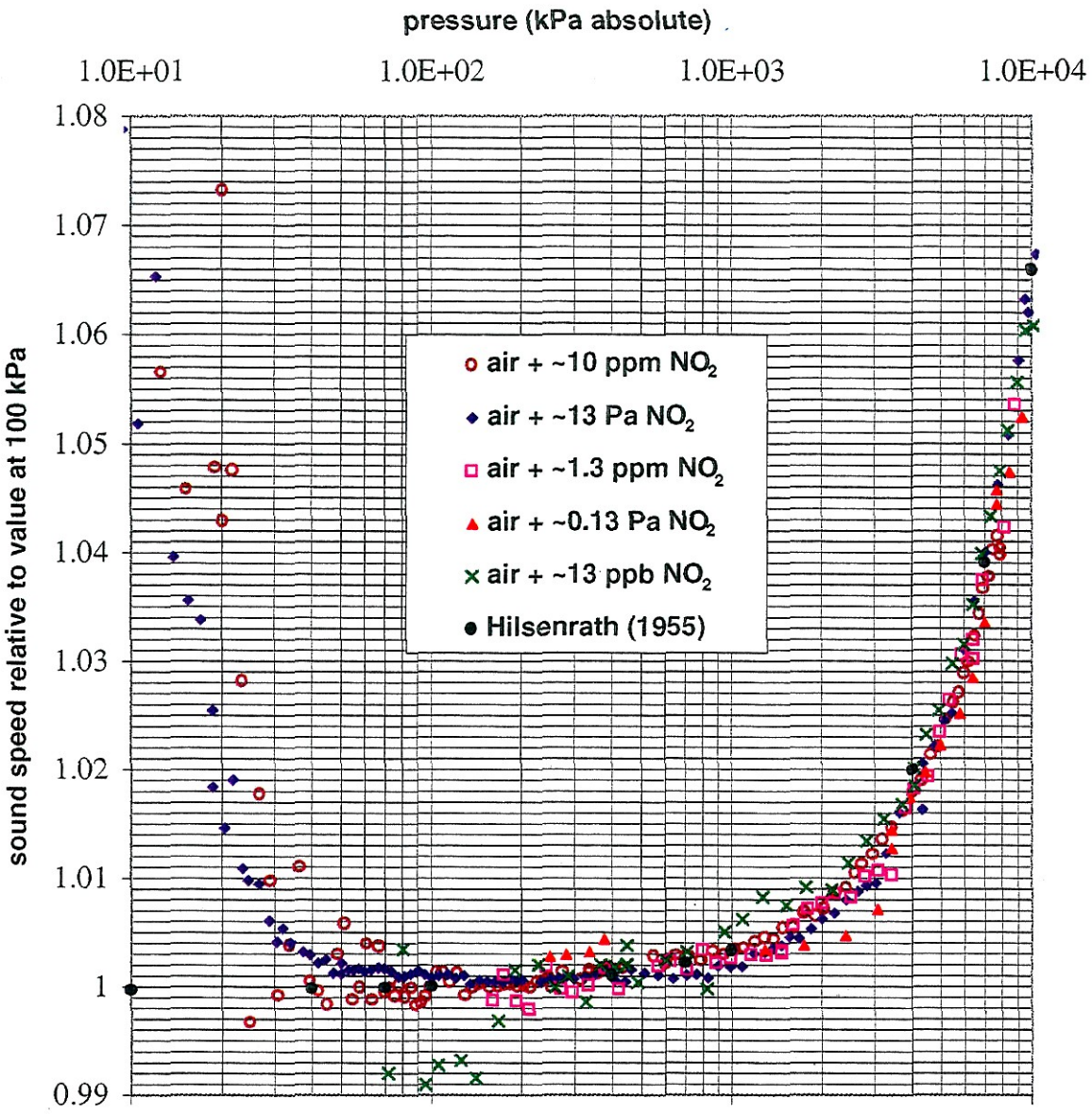

FIG. 11.21. Variation of measured sound speed of air with pressure (corrected for 300 K). The magnitude of the signals taken in constant seed gas partial pressure and constant concentration surveys varies over seven orders of magnitude.

values of the thermal diffusivity evidently to compensate for beam misalignment. The data marked by "x"-s shows clearly where the source laser beam was "tweaked" into alignment at high pressures by a 20% increase in the measured conductivity. Even the values obtained after beams were carefully aligned at high pressure depart significantly from the published measurements after the pressure is significantly reduced. The origin of this problem is probably misalignment from differential refraction of

the (blue) source beam and (yellow) driver beams. Another possible explanation is that beam self-focusing and self-defocusing effects which were observed during the experiments changed the dimensions of the beams over the large range of pressure excursion enough to affect the accuracy of the model which assumed constant beam diameters. Both problems can be mitigated by using unfocused beams. Finally, it is likely that multi-rate finite thermalization effects contribute to the problem at the lower end of the pressure range. The origins of these problems must be diagnosed and addressed before transport-property measurements using LITA approach their limiting accuracy.

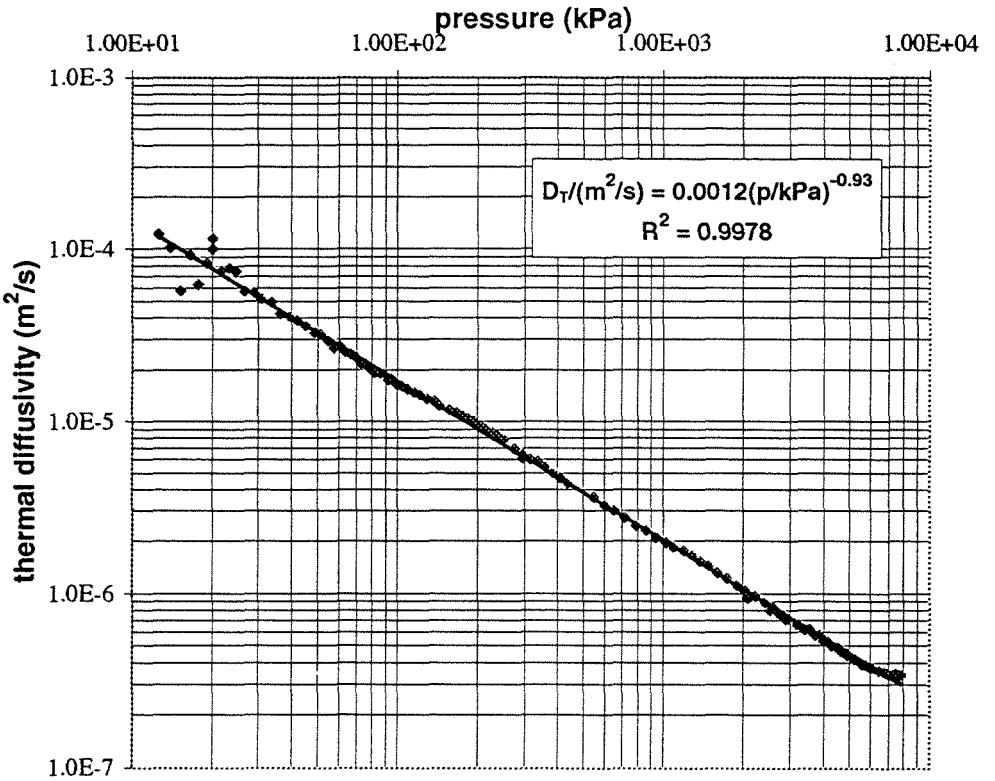

FIG. 11.22. Variation of thermal diffusivity measurements in air with ~10 parts-per-million NO_2 and best power-law fit.

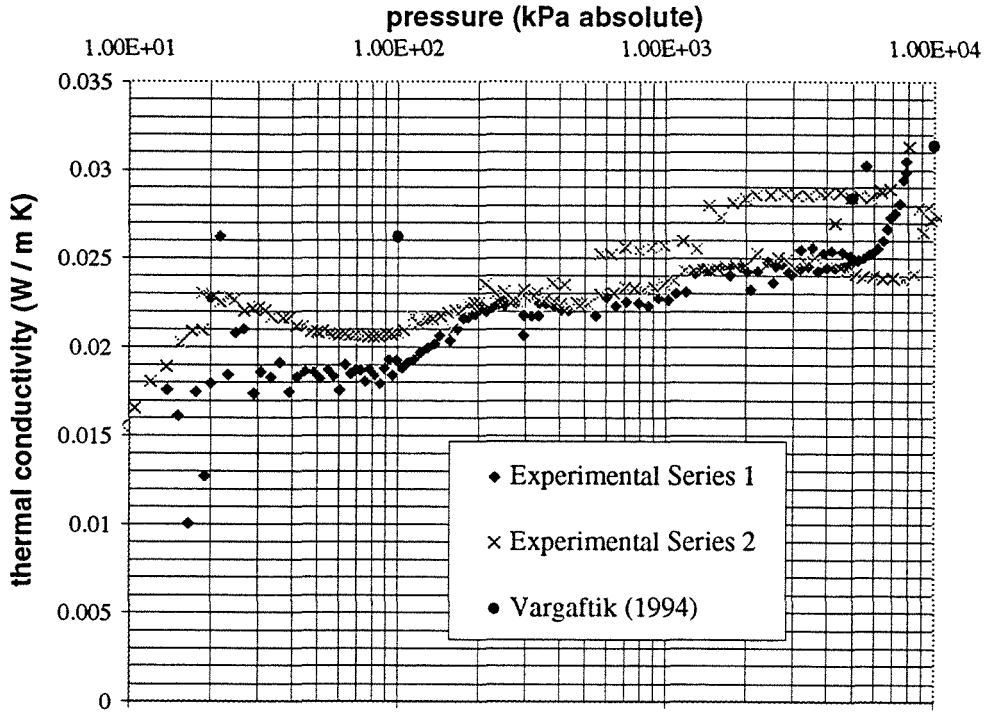

FIG. 11.23. Variation of thermal conductivity derived from measurements in NO_2-seeded air. Independent published data appear as solid circles. Beam parameter uncertainties and misalignment apparently limited the accuracy of the measurements.

11.4.2 Helium

Because of its low susceptibility at visible frequencies, helium provided LITA signals that were much weaker than those from air. No electrostrictive element to the signals was observed in the tests which covered room-temperature-helium pressures up to 14 MPa. The LITA signals detected in helium arose from thermalization from tank impurities (most likely NO_2) and seeded NO_2. The test gas formed by successive dilution, contained parts-per-million levels of NO_2. The actual concentration of NO_2 in the mixture at these low levels is uncertain since NO_2 tends to adhere to the surfaces of the gas-handling equipment and the bomb, to be convected into the cell during filling. Also, the tank gas apparently contains trace quantities of an impurity which generates a LITA signal, most likely NO_2.

As evidenced by the shapes of the signals and the poor quality of the agreement with theory, the helium data was taken with relatively poor beam alignment. This signal flaw seriously degrades transport-property measurement, such as the thermal

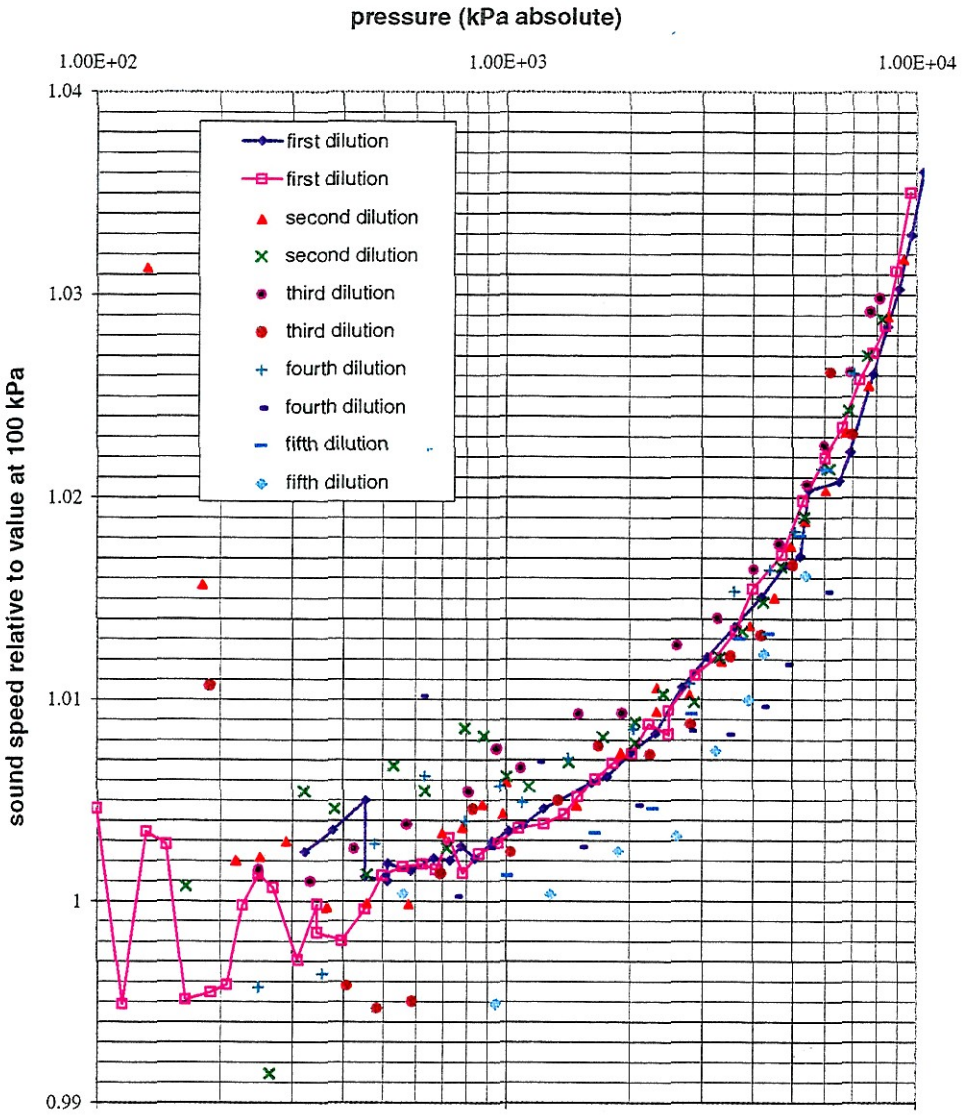

FIG. 11.24. Sound speed of helium as a function of pressure normalized to the sound speed at atmospheric pressure. The signal-to-noise ratio declined as the NO_2 seed gas was successively diluted.

conductivity shown in Fig. 11.25. The thermal conductivity measurements improved with pressure since the signal's "tail," which is dominated by the thermal grating signal, becomes a dominant feature of the signal at high pressures. The filter compensates for beam misalignment by artificially lowering the thermalization rate and thermal diffusivity to minimize the least-square deviation. It is possible to statistically weight portions of the curve, for example the ringing part or the tail in order to improve estimation of a particular gas property, but that was not attempted. The sound-speed measurements, appearing in Fig. 11.24, were likewise degraded, but are

still accurate within 1%, except for those extracted from particularly noisy signals. There was no independent temperature measurement in these tests, thus temperature effects could not be corrected.

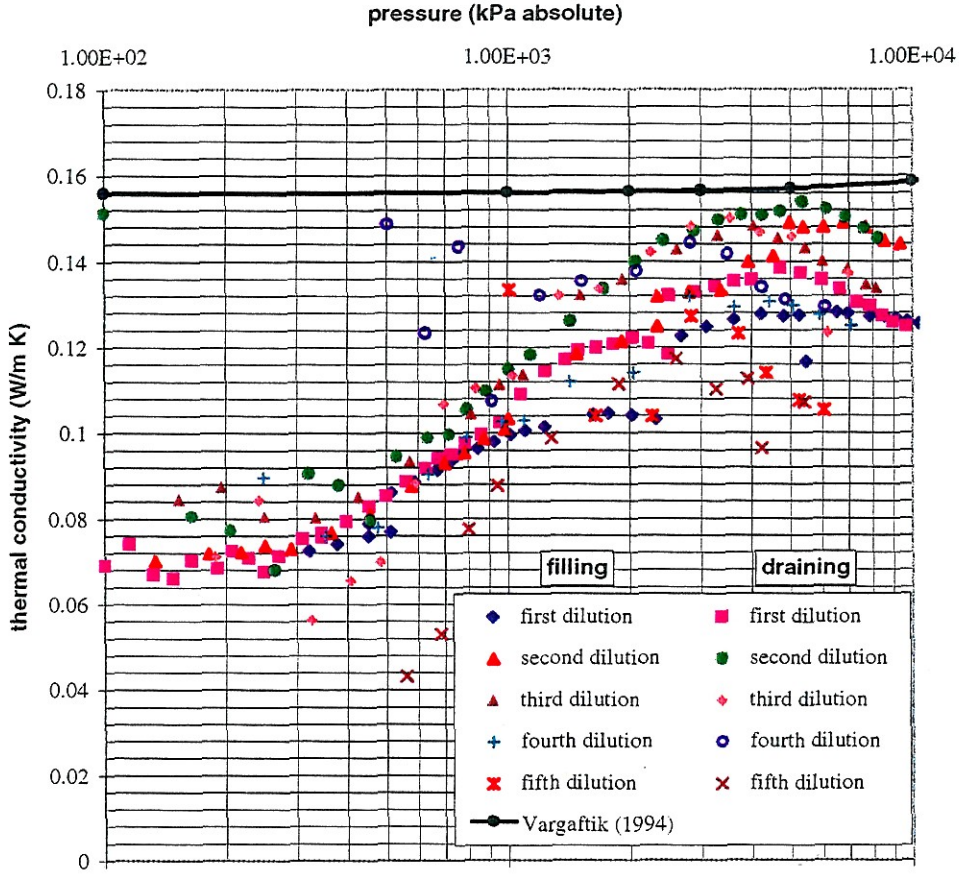

FIG. 11.25. Measured thermal conductivity of helium as a function of pressure. The signal-to-noise ratio declined as the NO_2 seed gas was successively diluted. Beam misalignment seriously degraded the accuracy of these measurements.

11.4.3 Carbon Dioxide

Carbon dioxide provided the largest signal levels of any of the gases that were tested because of its large non-resonant susceptibility. Signal levels were high enough for single-shot measurement at atmospheric pressure using no seeding other than tank impurities. Beam-steering, self-focusing, and self-defocusing were also proportionally larger than in other gases. The liquid-vapor critical point of CO_2 is only a few degrees above room temperature (~31 C) and within the working pressure range of the bomb. Tests were performed to observe critical point phenomena. To date, the critical point has not been approached closely enough to observe some of the major effects, e.g., critical opalescence, tremendous reduction in sound speed, etc. The difficulty in making measurements near the critical point has been dominated by the difficulty to achieve critical conditions, since the CO_2 liquefies in the relatively cool gas-filling system and gauges. Work is underway to solve this problem. Nevertheless, sizable reductions in the sound speed ~30% were observed near the liquid-vapor transition about 400 kPa below the critical point. The sound speed of CO_2 near 300 K as a function of pressure appears in Fig. 11.26. Several experimental surveys are over-plotted. The spread in the results of the surveys arises from small temperature differences between surveys. The sound speed relative to that at atmospheric pressure and 302 K is plotted in Fig. 11.27 as a function of temperature at constant density. On the same plot, the data are scaled by $\sqrt{T/300\text{K}}$, which would produce a horizontal line if the gas behaved thermally and calorically perfectly. The magnitude of the temperature effect is much larger than that predicted for a perfect gas, particularly at the lowest temperatures on the plot which are only slightly above the boiling point of CO_2. The nature of this temperature dependence of the sound speed is consistent with the results of calculations using the Bendict-Webb-Rubin model (Perry et al., 1984) for the equation of state of CO_2. The scatter evident in the sound speeds is most likely caused by temperature uncertainty and inhomogeneities in the gas, since the nonlinear filter estimated an uncertainty in the extracted sound speed of ~3 mm/s†. Nonlinear hydrodynamic and beam-propagation effects were mitigated by

† This estimation assumes a normal distribution of errors and is only valid to the extent that the distribution is normal. There are techniques to improve this estimation of uncertainty (Press et al., 1986). This estimate should be correct within several orders of magnitude, which is sufficient to validate the inference about the source of the error.

taking the data in Fig. 11.27 with ~1 mJ driver-laser pulse energy and ~50 mW source laser power. Data taken at higher powers do not conform well to predictions of the analysis, apparently as a result of these effects. Signals recorded at these lower power levels match the theoretical predictions much more closely. Studies of the critical region of carbon dioxide will provide an excellent test of the capabilities of LITA in challenging environments.

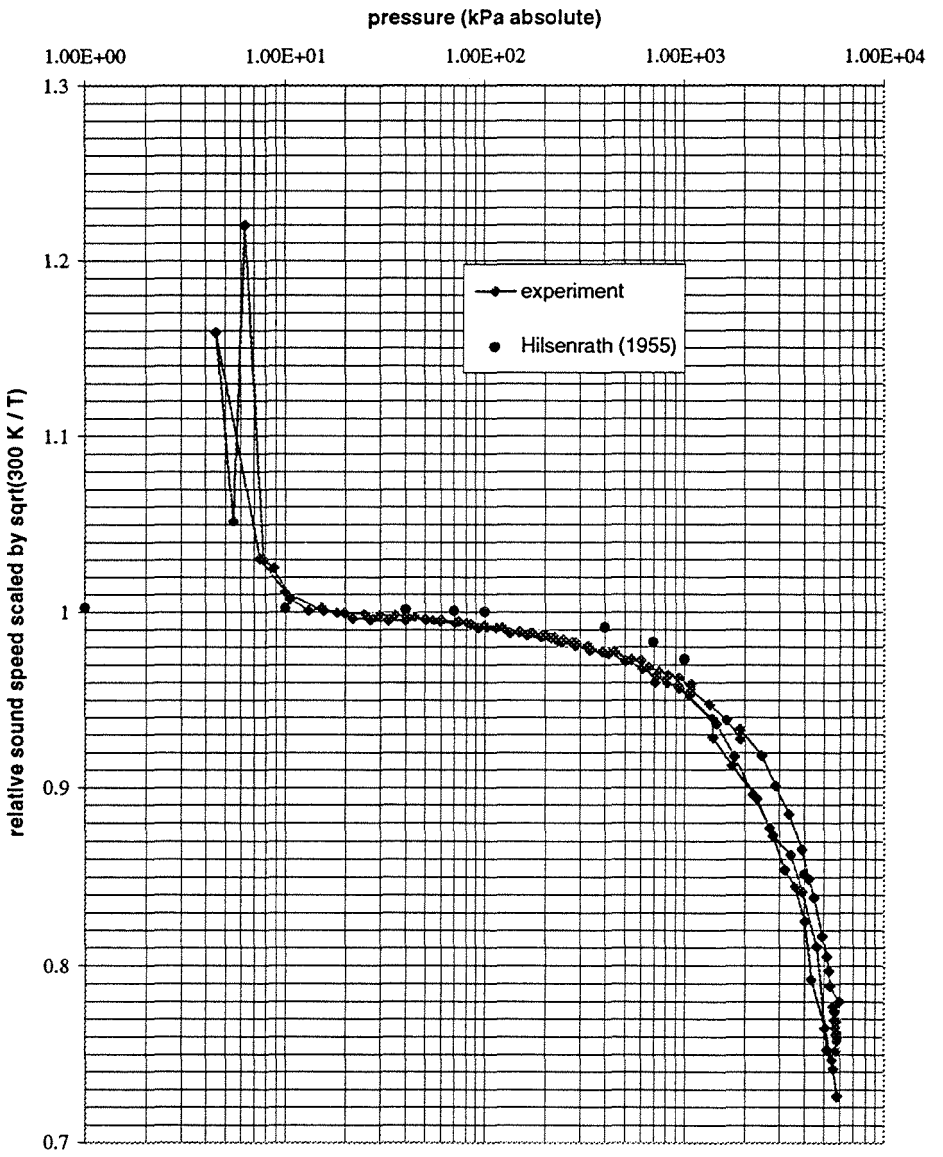

FIG. 11.26. Sound speed of CO_2 as a function of pressure at ~300 K. Several experimental surveys are over-plotted. The spread in the data is evidently caused by small differences in the gas temperature between surveys. The uppermost pressure is near the vapor pressure of the CO_2.

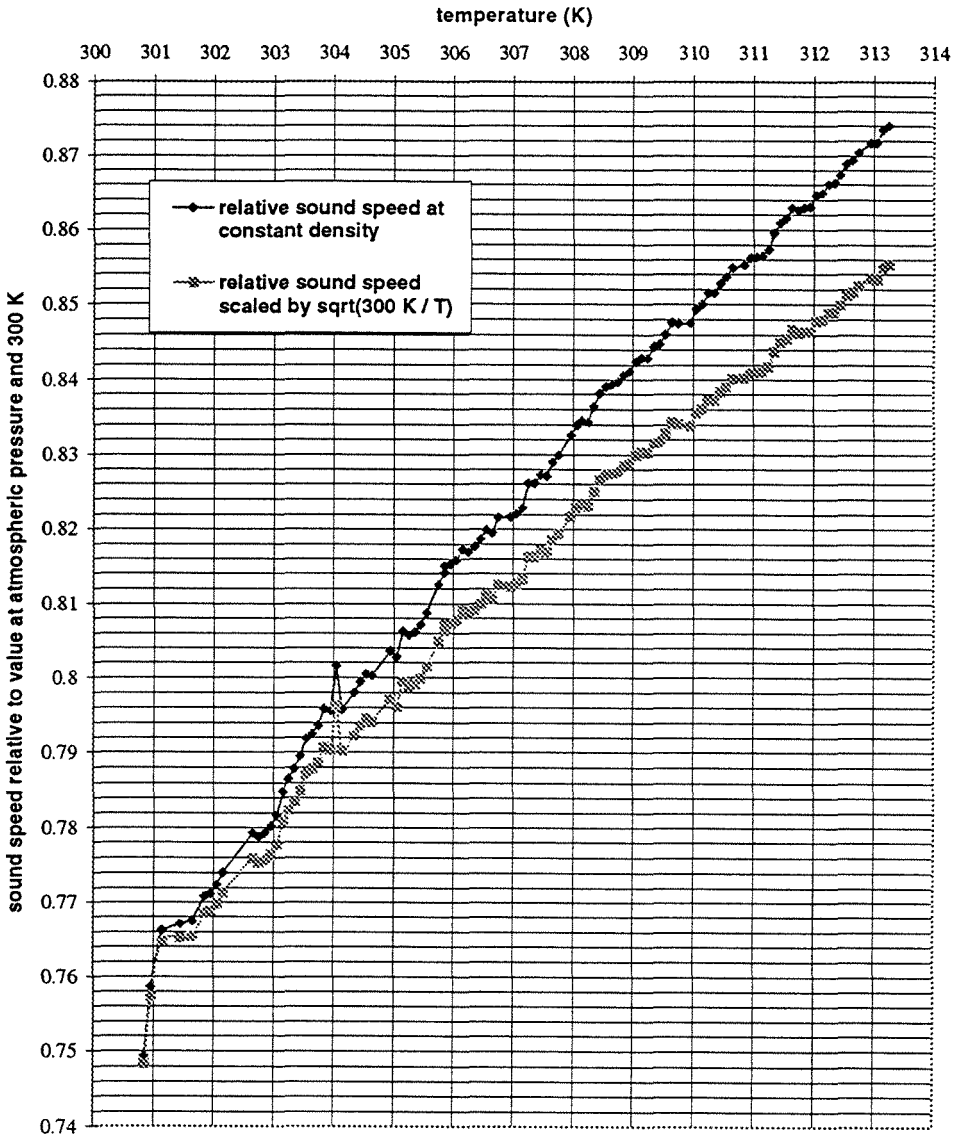

FIG. 11.27. Sound speed of CO_2 as a function of temperature at constant density. The low temperature limit of the plot approaches the boiling point of CO_2. The non-ideal gas behavior of the CO_2 is demonstrated in the curve obtained by scaling the sound speed by $\sqrt{T/300\text{K}}$. For a perfect gas, this curve would be a horizontal line.

11.5 Effects of Turbulence and Convection on LITA Signals

In most LITA tests conducted in the high-pressure bomb, the effects of convection of the gratings and turbulence of the gas on the signals is negligible. In many practical applications however, these effects may be important. Fluid motion causes a Doppler shift in the frequencies of the beams in the fluid frame. The effect of this Doppler shift on the acousto-optical driving is discussed in Chapter 5. Fluid motion also convects the laser-induced gratings relative to the source beam. The scattered field bears a Doppler shift from this motion, as discussed in Chapter 7. If the displacement of the grating across the source beam by convection is comparable to or larger than the signal beam radius over the life of the grating, the decay of the envelope of the signal is faster than that of the quiescent fluid. In the study that was conducted, it was convenient to create flow in the cell using the stirring fan. Because of the relatively low flow velocities generated by the fan, long-lived thermal gratings in CO_2 near its room-temperature vapor pressure (half-life ~40 μs) were used to study this effect. Thirty-shot averages of LITA signals were taken at various stirring-fan power settings. These data appear in Fig. 11.28. The ringing part of the LITA signal is not resolved on the time-scale in Fig. 11.28. The signal taken with no stirring is lower in intensity than those in which the gas is stirred because of thermal blooming effects.

The displacement by uniform convection Vt of a Gaussian thermal grating from a Gaussian source beam modulates the signal by the envelope

$$\mathcal{L}(t) \sim \mathcal{L}_0(t) \exp\left(-2\frac{V^2t^2}{\sigma^2 + w^2}\right), \tag{11.1}$$

where $\mathcal{L}_0(t)$ is the LITA signal without flow, and w and σ are the grating and source beam radii, respectively. The effect of a uniform shear on the signal is likewise Gaussian in time. Thus the negative logarithm of the ratio of the signal with flow and the signal without flow should be positive and quadratic in time, with zero slope at $t = 0$. The signals thus processed appear in Fig. 11.29. Note the curves appear to be mostly linear with slight positive curvature, indicating that the enhanced decay rate has more of an exponential than Gaussian nature. The exponential decay is caused by turbulent decohering of the gratings.

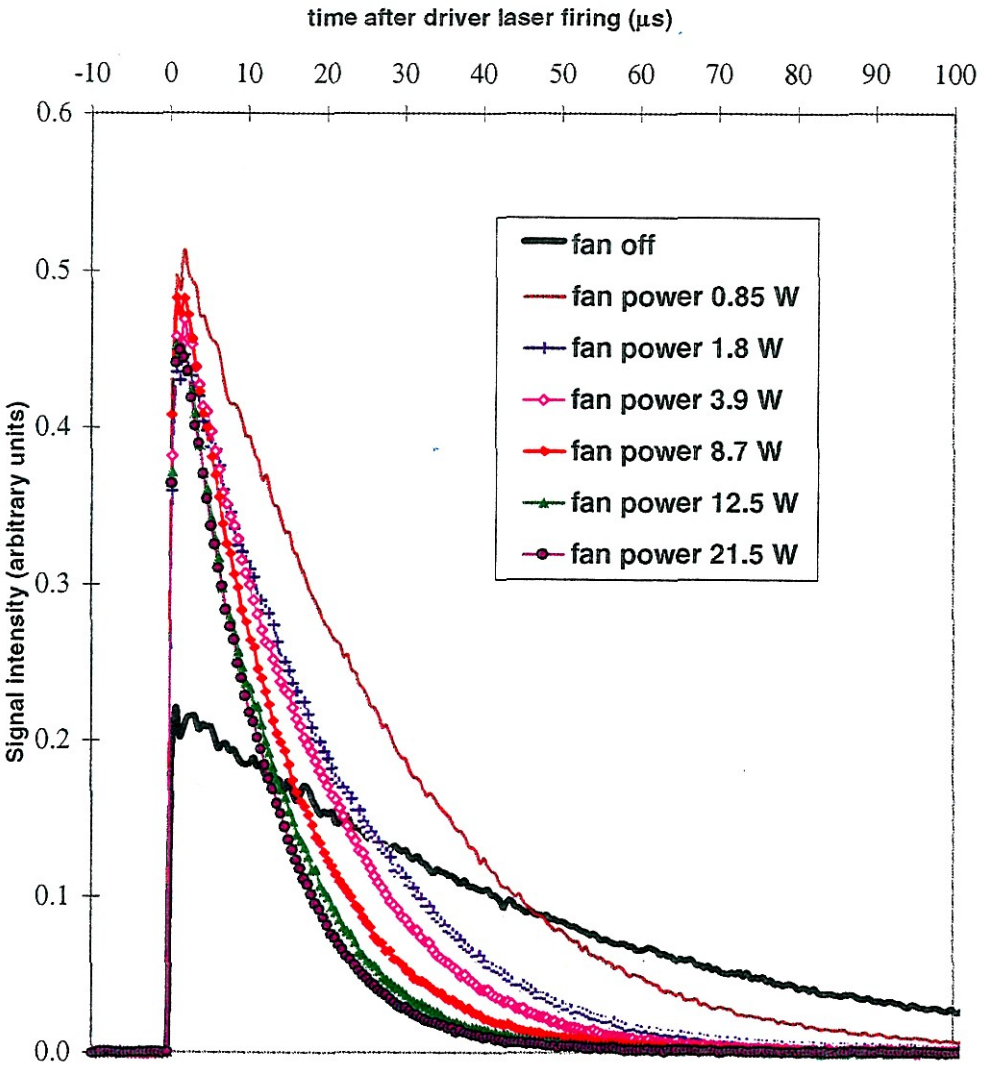

FIG. 11.28. LITA signals from CO_2 at 5.59 MPa and 299 K. The effect on the signal lifetime of gas motion generated by a stirring fan is evident. The reduced intensity of the no-flow signal is caused by thermal blooming effects.

Table 11.1 lists estimated turbulence properties of the flow in the cell. These estimates are based upon a balance between fan power and turbulent energy dissipation rate.

$$P_{fan} \sim \rho V^3 b, \tag{11.2}$$

where P_{fan} is the rate of addition of kinetic energy to the CO_2 by the fan, ρ is the density of the CO_2 at the conditions studied (~99 kg/m^3), V is the characteristic velocity of the largest scales of turbulence in the bomb, and b is a characteristic dimension of the bomb interior (~80 mm).

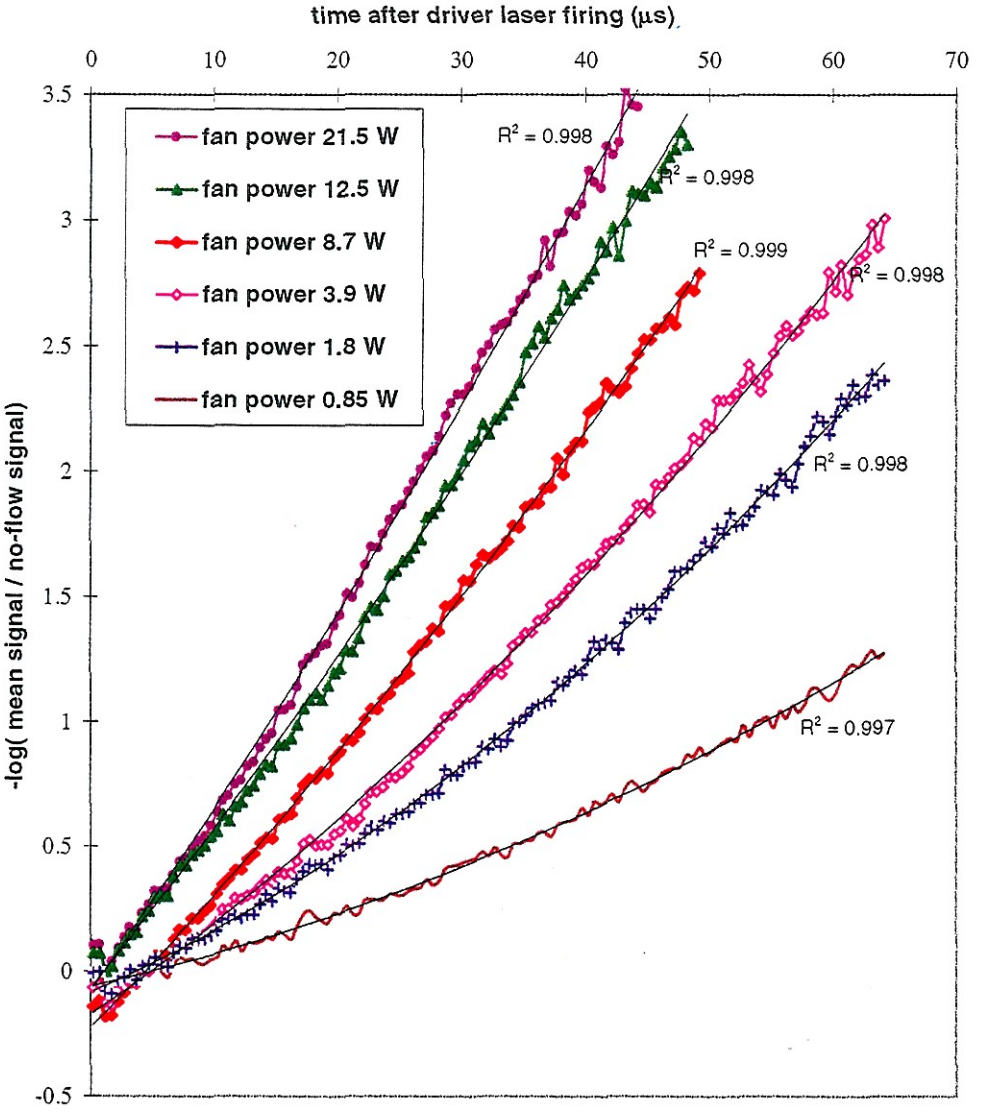

FIG. 11.29. The negative logarithm of the signal intensities is plotted against time. The best-fit quadratic curves are over-plotted. The finite slope at $t = 0$ is caused by thermal grating dephasing by turbulent fluid motion. The upward curvature of the data is caused by coherent motion of the thermal grating away from the source beam.

It was assumed for these estimates that the fan converted 80% of its electrical energy to kinetic energy of the gas over all operating powers, an arbitrary and imprecise choice. Better estimates of the turbulence parameters could be obtained by direct measurement, for example using hot-wire anemometry or heterodyne LITA velocimetry. These rough estimates suffice, however, for illuminating the cause of exponential decay of the signal. Notice the large Reynolds numbers ($> 10^6$) in the low-velocity flow. These are caused by the very low viscosity (ν) of the high-pressure gas. The grating

wavelength ($\sim 15.2\mu$m) is comparable to the Kolmogorov length scale, $\lambda_K \sim (\nu^3 b/V^3)^{1/4}$, which is the smallest length-scale of free turbulent flows. Fluid motion on this length scale is damped strongly by viscosity. A cascade of kinetic energy from larger scales of turbulent motion re-supplies energy to the eddies at this scale. The "turnover" time of these smallest eddies is the Kolmogorov time-scale, $\tau_K \sim (\nu b/V^3)^{1/2}$. The lifetimes of the gratings are comparable to the Kolmogorov time-scale. Turbulent flows may also be described by the Taylor length scale, λ_T, an *interfacial* length scale that is roughly the thickness of the "boundary layer" between turbulent eddies. Associated with this length scale is the Taylor time-scale, which is identical to the Kolmogorov time scale. Fig. 11.30 shows the curves of Fig. 11.29 re-plotted against time nondimensionalized by the estimated Kolmogorov scales. The curves collapse onto each other within the uncertainty in the turbulence scales. The collapse of the slope of the curves is marginal, an unsurprising result given the crudity of the flow-condition estimates. However, there is no systematic trend in the slopes and other simple scalings of the time axis provide worse collapse of the data. The $1/e$-times in the decay of the signals correspond approximately to the Kolmogorov time scales.

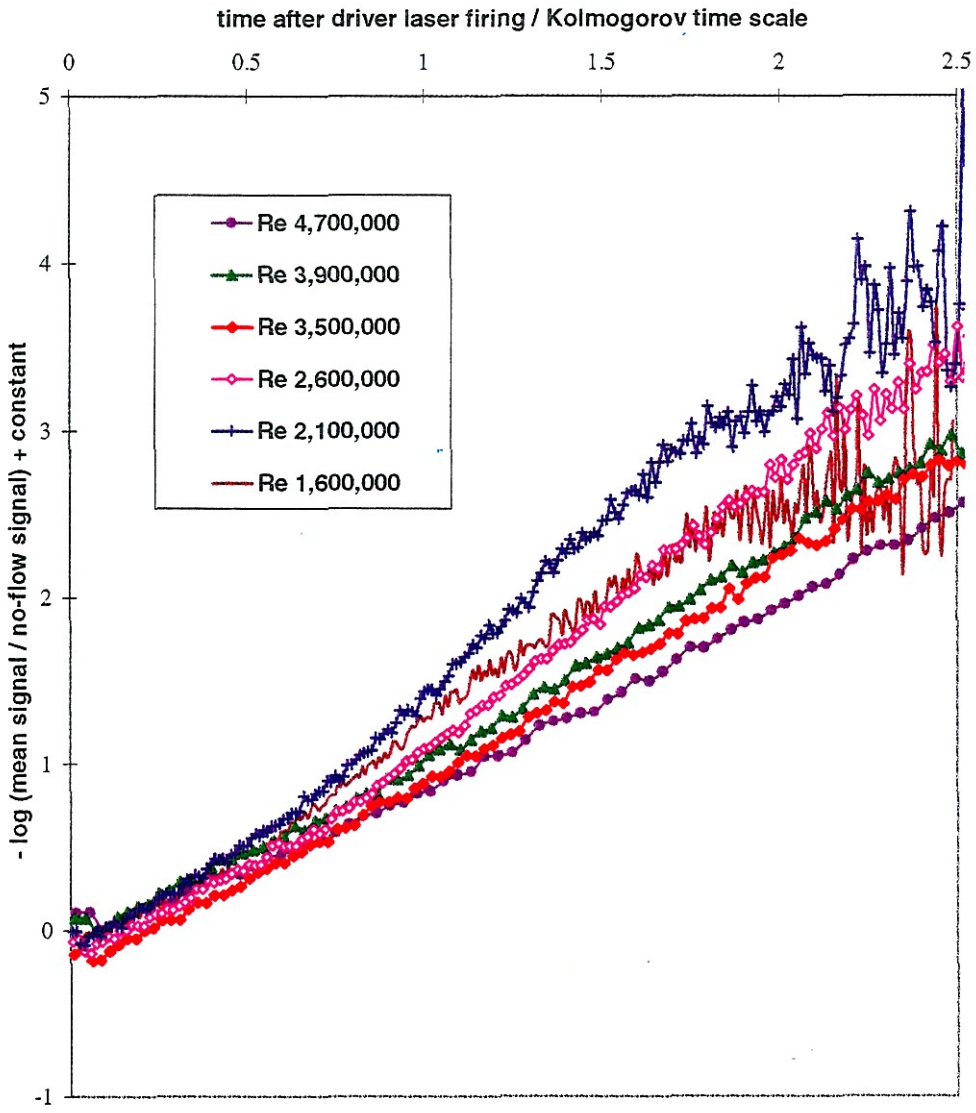

FIG. 11.30. Replot of the data in Fig. 11.29 with the time axes of each curve scaled to the estimated Kolmgorov time scale.

Fan Power, P_{fan} (W)	*Signal Decay Time* (μs)	*Est. Flow Speed,* V (m/s)	*Reynolds Number,* Re	*Kolm. Time Scale,* τ_K (μs)	*Kolm. Length Scale,* λ_K (μm)	*Taylor Length Scale,* λ_T (μm)	τ_{nf}/τ_K	λ_x/λ_K	ℓ / λ_T
0	102 (τ_{nf})	0	0	inf.	inf.	inf.	0	0	0
0.85	48	1.0	1,600,000	64	1.8	240	1.6	8.7	33
1.8	25	1.4	2,100,000	44	1.5	210	2.3	10	37
3.9	20	1.6	2,600,000	30	1.2	190	3.4	13	42
8.7	16	2.1	3,500,000	20	1.0	170	5.1	16	48
12.5	14	2.4	3,900,000	17	0.9	160	6.0	17	51
21.5	12	2.8	4,700,000	13	0.8	140	7.8	20	56

TABLE 11.1 Turbulence parameters of the stirring-fan experiments.

The Taylor length scale is much smaller than the long dimension of the gratings (~8 mm), thus the gratings may experience multiple inertial eddies—patches of fluid that move relatively independently under the action of inertial as opposed to diffusive forces, separated from each other by thin shear layers. Thus, motion induced by inertial eddies can also decohere the thermal gratings. Fig. 11.31 shows the ratio of 15 single-shot LITA signals to the mean signal at a fan power of 3.9 W. The signals lying above the mean tend to be smooth. The signals below the mean are often oscillatory, indicating that inertial eddies have sheared the thermal grating. The shear layer thickness, $\sim \lambda_T$, is small compared to the grating length ℓ, thus, the sheared grating consists mostly of coherent grating sections moving at different velocities. The velocity difference creates Doppler beats in the signal. The relative velocities may be inferred accurately from the frequency of the oscillation. The highest velocity difference is about half the estimated large-scale velocity in the bomb. Most of the Doppler beats correspond to velocity differences closer to one-tenth the estimated large-scale velocity. These measurements are most likely to reveal the velocity scales of eddies the size of the long grating dimension. Since this is roughly one-tenth the characteristic dimension of the bomb, the corresponding reduction in velocity scale is reasonable. It is noteworthy that this is the first application of LITA for heterodyne velocimetry. This form of differential velocimetry may be useful for the study of turbulence on scales and in locations that are difficult to probe.

Having addressed the turbulent contribution to the decay of the signals, it is possible to regard the Gaussian element of the decay of the gratings separately. The mean speed of the grating (normal to the source beam) may be inferred by the coefficient of the quadratic term of the curve fits shown in Fig. 11.29. This leads to the velocity estimates in Table 11.2.

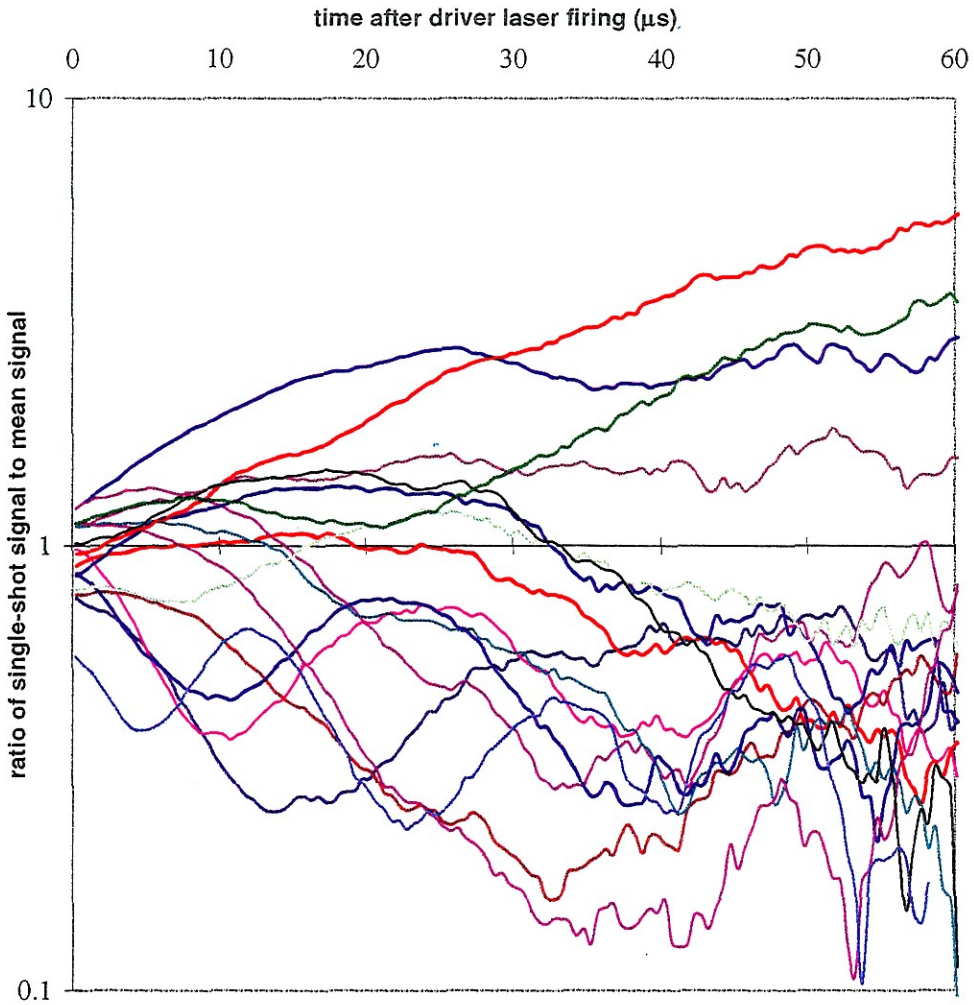

FIG. 11.31. Ratio of single-shot-to 30-shot-mean LITA data obtained in high-pressure CO_2 with a stirring fan power of 3.9 W. Ringing from Doppler beating is evident in most of the 15 curves. This ringing occurs when the shear layer of a turbulent eddy intersects the thermal grating, rendering two coherent gratings with different velocities.

Fan Power (W)	*Est. Flow Speed, V* (m/s)	$V\tau_{nf} \cdot(\sigma^2+w^2)^{-1/2}$	*Calc. Speed from Gaussian Decay* (m/s)
0.85	1.0	0.18	1.8
1.8	1.4	0.23	2.4
3.9	1.6	0.30	2.3
8.7	2.1	0.39	2.2
12.5	2.4	0.44	2.2
21.5	2.8	0.52	2.3

TABLE 11.2 Estimates of mean flow speed from the magnitude of finite-beam effects.

These estimates are uncertain because of the small amount of curvature and the noise of the data in Fig. 11.29. However, they are consistent within their large uncertainty with the magnitudes of the large-scale velocity estimated using simple dimensional analysis. The accuracy of these "homodyne" speed measurements would be improved by eliminating noise using more signal averaging. Tightly focused beams enhance this effect.

In many situations, effects of convection and turbulence would be detrimental to the measurement of transport properties. The importance of the finite beam-size effect (quadratic element of the curves in Fig. 11.29) is dictated by the magnitude of the convection parameter $V\tau_{nf}/\sqrt{\sigma^2+w^2}$, where τ_{nf} is the no-flow lifetime of the grating. The convection parameter is given approximately by

$$\frac{V\tau_{nf}}{\sqrt{\sigma^2+w^2}} \sim \frac{\lambda_g^2 \mathrm{Re}\,\mathrm{Pr}}{4\pi^2 b\sqrt{\sigma^2+w^2}}, \tag{11.3}$$

where Re is the Reynolds number of the flow based upon the length scale b, and Pr is the Prandtl number of the gas.

The magnitude of the effect of turbulence on the signal is more complicated to estimate. The important parameter for the effect of small-scale turbulence on the signal is the ratio of the (no flow) lifetime of the grating to the Kolmogorov time scale, τ_{nf}/τ_K. This parameter is approximately

$$\frac{\tau_{nf}}{\tau_K} \sim \left(\frac{\lambda_g}{b}\right)^2 \frac{\mathrm{Re}^{3/2}\mathrm{Pr}}{4\pi^2}, \tag{11.4}$$

where the Reynolds number Re is based upon the fluctuating large-scale speed and the length scale b.‡ If this ratio is sufficiently large, dephasing of the grating by small-scale turbulence may be important, provided the Kolmogorov length scales are not much larger than the grating wavelength. The ratio of these length scales, λ_g/λ_K, is an important parameter that is given approximately by

$$\frac{\lambda_g}{\lambda_K} \sim \frac{\lambda_g}{b}\mathrm{Re}^{3/4}. \tag{11.5}$$

‡ The distinction between the mean speed and the fluctuating speed is not important in the experiments conducted in the bomb, but is important in most other flow experiments.

As observed in the single-shot data in Fig. 11.31, turbulence at larger scales can also affect the signal. The importance of this effect is measured by the parameter ℓ/λ_T that is given approximately by

$$\frac{\ell}{\lambda_T} \sim \frac{\ell}{b}\left(\frac{\mathrm{Re}}{15}\right)^{1/2}. \tag{11.6}$$

As evidenced by the data and the magnitudes of these parameters (included in Table 11.1), all three effects are important in the tests conducted on high pressure CO_2. The variation of these parameters with Reynolds number, for typical beam geometries, appears in Fig. 11.32. The convection and turbulence effects can be mitigated by adjustment of the beam parameters, as described in Fig. 11.32. The magnitude of convection and turbulence effects at other conditions may be estimated using Fig. 11.32 and Fig. 11.33, which graphically relates the Reynolds, Knudsen, and Mach numbers. The intersection of the horizontal and vertical shaded regions highlight the conditions of the experiments presented in this section. Because the convection and turbulence effects are approximately functions only of the Reynolds number, the magnitude of these effects is roughly constant across horizontal lines. The vertical dashed line is approximately atmospheric conditions in air.

There are other effects associated with flow and turbulence which may be important in practical applications. Beam steering by susceptibility gradients in the flow is likely to be the most important of these effects. Susceptibility gradients can be caused by gas composition, temperature, and density gradients created, for example, by combustion and compressible flow. To first order, beam steering affects the alignment of beams, which has been demonstrated to be important in the interpretation of signals. Higher order effects can defocus beams, change beam-crossing angles, etc. The use of a forward phase-matching geometry with narrow beam-crossing angles mitigates, but does not eliminate the effects of beam steering. The use of unfocused beams with this beam geometry and intelligent experimental design is likely to be required in order to obtain accurate measurements when LITA is applied to optical-diagnostic-unfriendly flows in large flow facilities, such as T5.

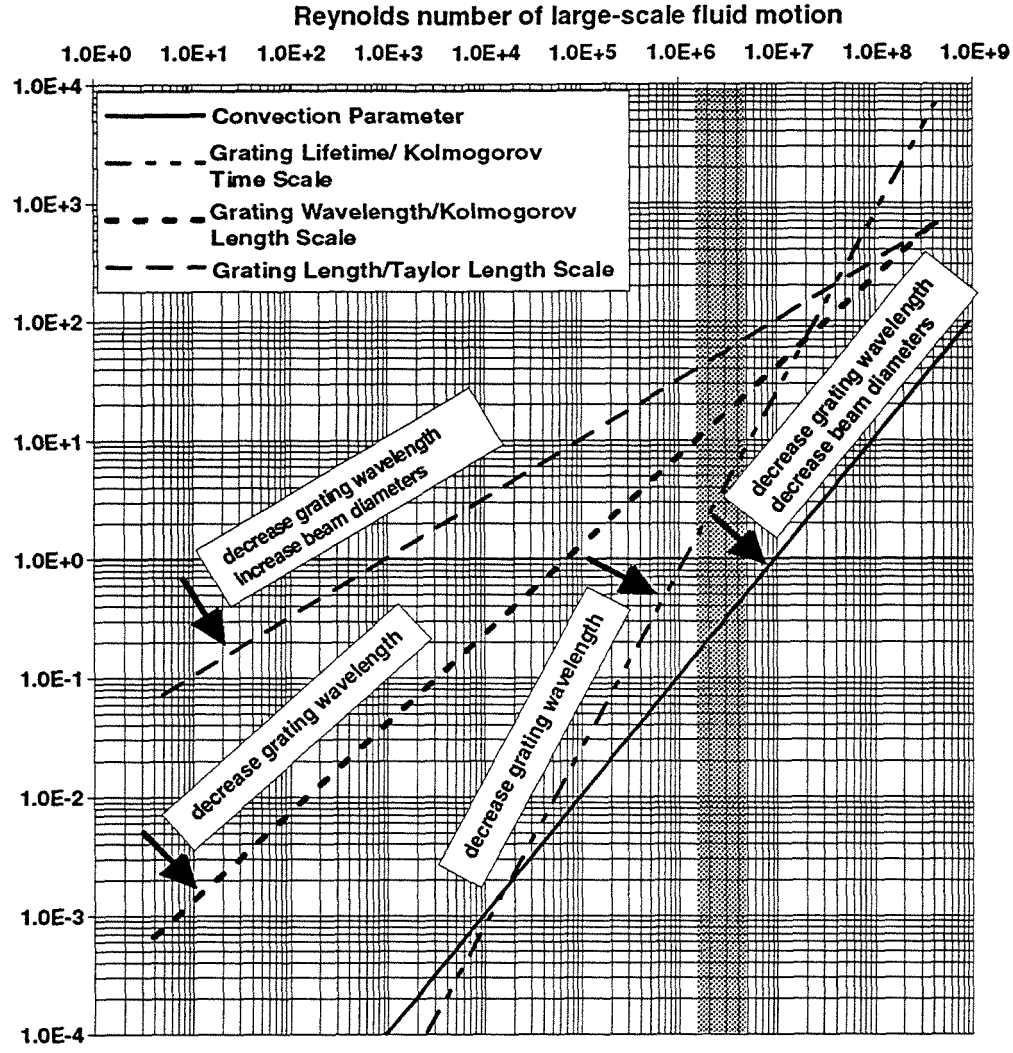

FIG. 11.32. Plot of the convection- and turbulence-parameter values vs. Reynolds number for the beam parameters used in these experiments. The text with each curve notes how to modify beam parameters to reduce fluid motion effects. Tests were conducted in the shaded region.

11.6 Multiplex Spectrum Measurements

The multiplex experiments at GALCIT are at an early stage of development at the time of this writing. Initial spectra have been taken with the broad-bandwidth flashlamp-pumped dye laser tuned near 570 nm. In this region at several atmospheres of pressure, little spectral structure was observed in NO_2-seeded CO_2. However, signal strengths are encouragingly high. Indeed, the surface of the optical fiber that is used to feed the signal beam into the spectrometer has been damaged from the intense, focused signal beam. Work is underway to examine the spectral region of NO_2-

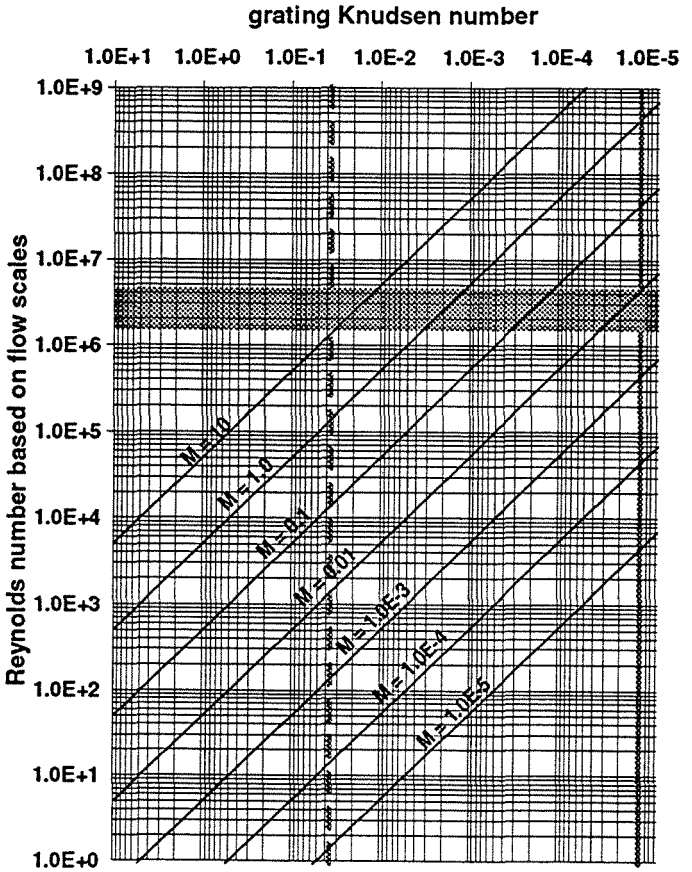

FIG. 11.33. Reynolds, Knudsen, and Mach number relationship in the tests. The importance of convection and turbulence effects is approximately constant with Knudsen number. The intersection of the horizontal and vertical shaded regions is the scope of the finite flow-speed tests. The dashed line describes atmospheric air.

seeded air that is shown in Fig. 11.15. The signal beam can usually be seen quite clearly, a tremendous advantage in alignment. The signal beam also has a temporal modulation similar to that in narrowband LITA, allowing both types of gas property measurements to be taken using the same laser pulse.

Spectral measurements using multiplex LITA may be impractical in gases with large nonresonant susceptibilities, since the number density of resonant molecules will have to be relatively high in order to modulate the susceptibility in a detectable fashion. High densities of resonant species may cause excessive absorption of the source and signal beams. Further study will reveal the limitations of multiplex LITA as a spectroscopic technique.

11.7 Experimental Notes

The experience of recording and analyzing LITA signals in a variety of gases over a wide range of seed-gas concentrations and buffer-gas pressures has been fraught with hard-learned lessons. Some of these lessons are generic to nonlinear optical diagnostics and have probably also been experienced by other experimenters. Several of them, however, seem to be relatively specific to LITA and nonlinear optical diagnostics in high-pressure gases. The most important of these lessons deals with the problems exacerbated by the use of focused beams, namely beam misalignment effects (lamented throughout the results section!) and the beam-propagation effects of beam self-focusing, self-defocusing, and beam steering.

Fig. 11.34 shows the variation of peak and integrated signal strength as a function of grating Knudsen number or gas pressure. Approximate regimes are noted where finite-thermalization-rate, beam misalignment, and beam propagation effects are likely.[‡] The strong dependence of signal on pressure (Knudsen number) at constant seed-gas mixture fraction motivates the use of LITA at pressures in which the beam misalignment and propagation effects are likely.

11.7.1 Beam Misalignment

As has been repeatedly mentioned, accurate beam alignment is of paramount importance in obtaining accurate transport measurements using narrowband LITA. Although an extended model including the effects of misalignment could be used in the nonlinear filtering, the uncertainty in the extracted transport properties would undoubtedly increase. The difficulty is to be able to identify beam misalignment effects in the signals. Figs. 11.35 and 11.36 show LITA signals taken with varying amounts of deliberate and gross beam misalignment. Fig. 11.35 shows the effects when the signals are primarily from nonresonant electrostriction. A beam misalignment of ~10 μm (over a 1 m path!) yields a recognizable but "unfittable" signal. As the source beam is steered away in the plane of propagation of the coherent acoustic wavepackets,

[‡] Fig. 11.34 may be used in connection with Fig. 11.32 and Fig. 11.33 to assess the feasibility and potential complications of LITA measurement in a particular flow.

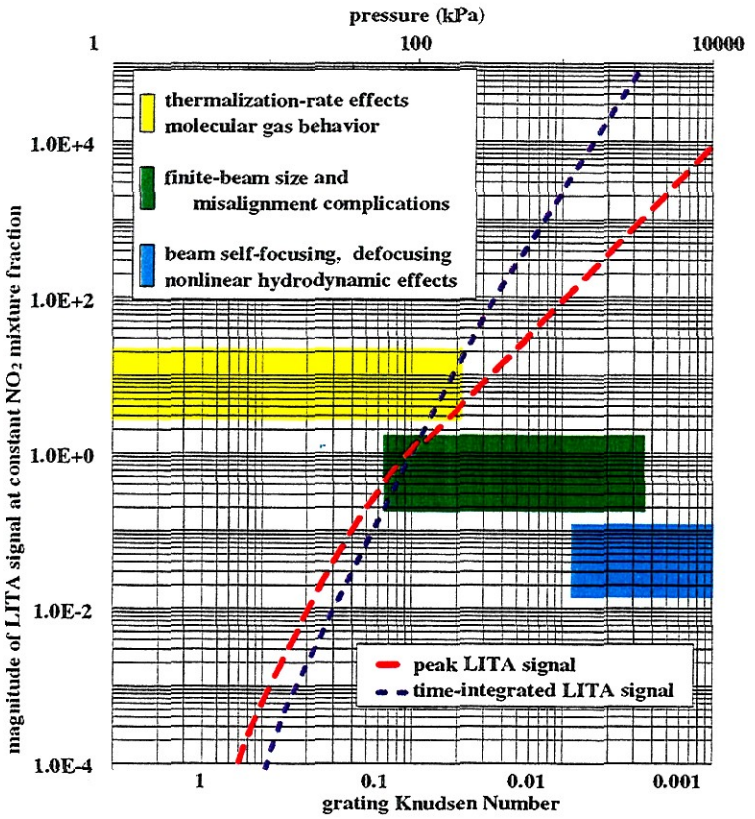

FIG. 11.34. Peak and integrated LITA signal as a function of pressure (grating Knudsen number) at constant seed-gas mixture fraction and beam geometry (from experimental data). Approximate regimes of various complicating effects are noted

the peak of the signal shifts to later times. The ringing disappears as only one of the counter-propagating waves contributes to the signal. The signal strength drops rapidly both from acoustic damping and the effect of the spatial filter in front of the detector. Fig. 11.36 shows the effect of gross beam alignment in experiments in which thermalization dominates. Two other "flaws" are evident in the signals in Fig. 11.36. The decay of the signal from the first peak is markedly larger than provided by the linear model. This effect is evidently caused by thermally-induced beam-steering caused by the driver laser. In these tests, enough NO_2 was present (~1 part-per-thousand) and the pressure was high enough to warrant this conclusion. Nonlinear hydrodynamic behavior may also have caused this effect. A third effect is self-defocusing or thermal blooming of the source beam, evidenced by the extended duration of the ringing part of the signal. This effect also arises from the combination of high pressure and NO_2 concentration.

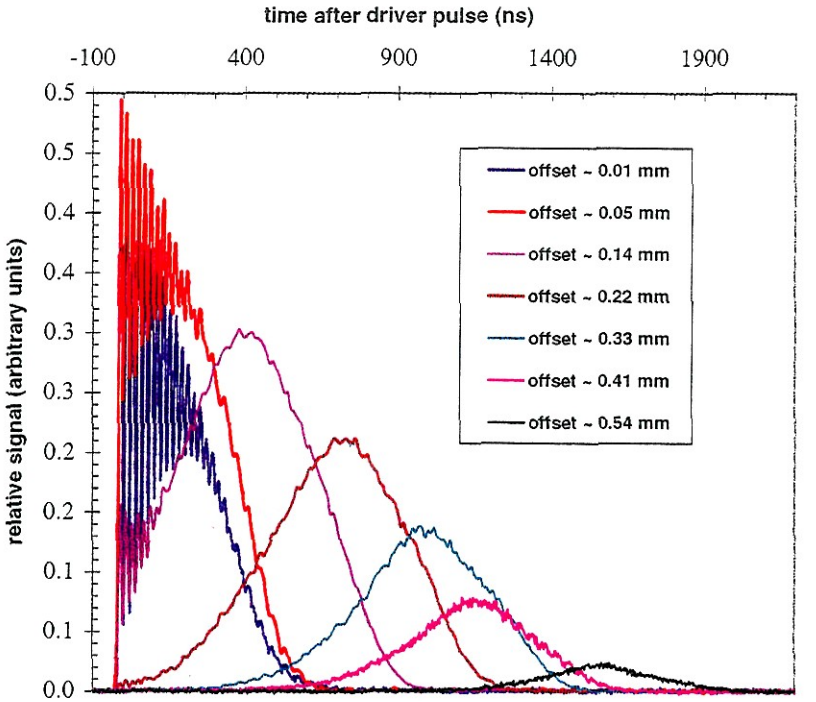

FIG. 11.35. Nonresonant electrostriction-generated LITA signals with varying degrees of gross beam misalignment.

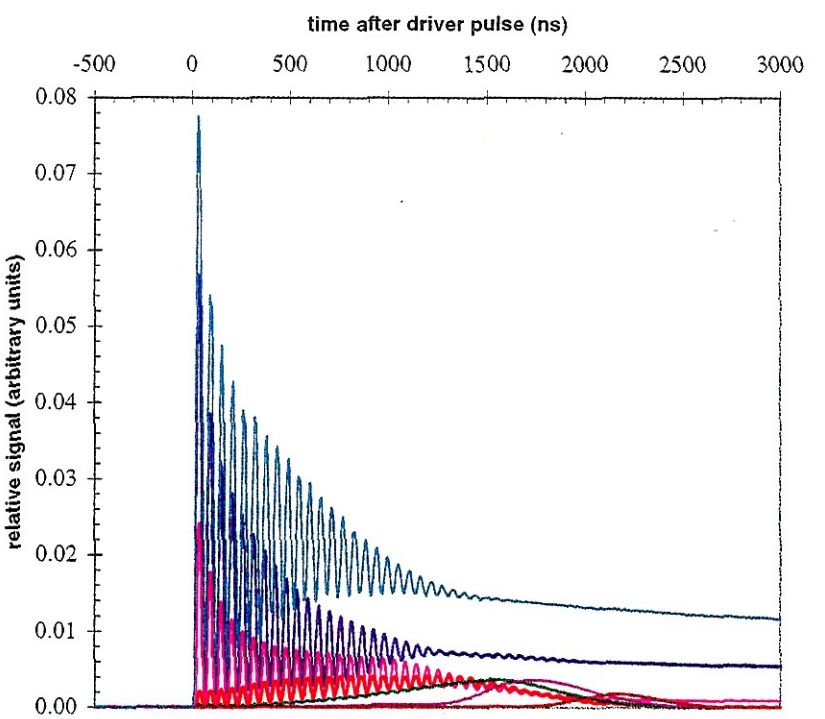

FIG. 11.36. Thermalization-generated LITA signals with varying degrees of gross beam misalignment.

11.7.2 Beam Self-focusing and Defocusing

Beam self-focusing and defocusing effects were observed in many of the experiments conducted at elevated pressure. These effects were apparent on the diameters of the beams leaving the bomb and were most marked on the CW source beam. Self-focusing occurred in air when NO_2 concentration was low enough that electrostriction dominated thermalization. Electrostriction along a beam's path through the gas in the bomb squeezes the gas toward the intense beam center (if the real part of the gas susceptibility at the source laser wavelength is positive). The increase in density along the center of the beam raises the local index of refraction, creating an index gradient which causes rays at the periphery of the beam to curve inward. This effect is susceptible to runaway since the self-focusing enhances the electrostriction effect. Several times, the high-power dielectric coating on the inside of the exit window has been burned by the self-focused argon-ion laser beam. Self-defocusing is usually caused by thermalization. Heating of the gas in the intense core of a laser beam lowers the density and thereby index of refraction at the core. This index gradient curves off-center rays of laser light outward, defocusing the beam. At high concentrations of NO_2, self-defocusing has been observed to spread the exiting diameter of the source beam by a factor of more than twenty. The extended duration of the ringing parts of the signals in Fig. 11.36 over those of other high-pressure signals, (e.g., in Fig. 11.7) is caused by self-defocusing of the source beam.

These effects degrade the accuracy of LITA measurement. They can lead to anomalously large or small signals. The dimensions of the beams are uncertain and a function of the pressure and gas composition, thus the effect is not easily "calibrated" away. These effects have been alleviated but not eliminated by chopping the source laser down to ~1 ms pulses (and driving in the first ~100 μs of the source laser pulse) and limiting the NO_2 concentration. Another strategy is to use unfocused beams.

11.7.3 Beam Steering

As mentioned previously, beam steering effects degrade the accuracy of LITA signals. They are caused by perturbations (and the spatial derivatives of perturbations) in the gas susceptibility caused by temperature, density, and species concentration perturbations in the gas. In early experiments using the high-pressure bomb, filling of the bomb with a pure gas from the top created a vertical seed-gas concentration gradient that was large enough to steer beams by ~10°. Temperature gradients were likewise a problem. At high pressures, several minutes of settling time were required before reliable data could be taken. This effect was remedied to a large part by installing the stirring fan. Using unfocused beams reduces the sensitivity to beam-steering effects.

A second beam-steering effect is caused by refraction of the finite angles that the beams make with the entrance and exit windows. Over the large pressure range studied, the angle of refraction of the beams entering the gas changes appreciably. This refraction does not change the grating vector, provided the bisector of the beams is aligned normal to the windows, a significant point when accurate sound speed and velocity measurements are desired over a range of flow conditions. However, dispersion of the gas between the index of refraction at the driver and source laser frequencies can affect beam overlap. This effect may be in part responsible for the difficulty in the accurate measurement of transport properties over the wide range of pressures in this study.

Part IV. Conclusions and Projections

CHAPTER 12
Conclusions

Laser-induced thermal acoustics is a laser technique for accurately measuring fluid properties remotely and nonintrusively. The physics that dictate the formation of the LITA signal are well understood. Intuitive interpretations of the physical processes have been described and illustrated. The LITA signal arises from a sequence of opto-acoustic and acousto-optic effects. So far, two opto-acoustic effects have been observed, electrostriction and thermalization. These effects depend on the real and imaginary parts of the linear susceptibility of the fluid, respectively. Because the two opto-acoustic effects produce signals with different characteristics, LITA can provide a measure of both parts of the complex linear susceptibility of a fluid.

An analytical expression for the magnitude and time history of LITA signals has been derived using the linearized equations of hydrodynamics and light scattering. The analysis treats both thermalization and electrostriction. The additional effects of photolysis and photophoresis may be included in a straight-forward manner by incorporating the equations of forced species diffusion, provided in Sec. 4.2. The analysis includes finite beam-size, finite beam-duration, and finite thermalization-rate effects, which lend generality to the result. High-order diffraction effects in the propagation of the laser-induced sound waves are ignored, limiting the applicability of the analysis of the signals produced by the sound waves long after opto-acoustic driving. Also, beam-divergence and noise is ignored. Further assumptions are described in Chapter 3. Using a SUN Sparc 5 computer, a 2000-point history of the signal can be calculated using the analytical expression in approximately one-half second. This speed of calculation makes nonlinear least-squares fitting or filtering of experimental signals practical. A computer routine has been written which automatically performs nonlinear least-squares fitting of the theoretical model to sequences of experimental data by adjusting the parameters of the model. This fitting routine is an optimal nonlinear filtering operation by which fluid properties are extracted from the signal. The filtering of each signal requires approximately one-minute on the SUN Sparc 5.

LITA has been demonstrated in gases ranging from rarefied air and helium to near-critical CO_2. The theoretical model represents experimental signals from both thermalization and electrostriction accurately. Filtering using the theoretical model consistently leads to over-prediction of the sound speed at grating Knudsen numbers greater than ~0.1. The equations of hydrodynamics do not apply in this rarefied regime, since they require the length-scales of fluid-property gradients to be much larger than the mean-free molecular paths. The over-prediction of the sound speed is consistent with the enhanced rate of the propagation of energy and momentum that is expected as molecular collisions become rare. At lower Knudsen numbers, the accuracy of sound-speed measurements is typically 0.1% for relatively noise-free signals. For noisy signals, accuracies may degrade to ~1%. The best accuracy of thermal diffusivity measurements has been ~1%. However, typical results are much worse (~10–20%). These measurements are sensitive to slight beam misalignment. While the effect of gross beam misalignment is obvious (Fig. 11.35 and Fig. 11.36), the effects of slight beam alignment are subtle. Tweaking the beams into precise alignment is difficult. Retaining the precise alignment over broad pressure excursions without "retweaking" is impossible with the experimental arrangement used in these tests. Thus, the accuracy of transport property measurements presented in Chapter 11 is far worse than the limiting value. The use of unfocused beams and phase-conjugate geometries is expected alleviate these problems in future tests.

LITA has been successfully applied for the spectroscopic study of gas components. Relatively noise-free susceptibility spectra have been taken of >50 parts-per-billion NO_2 in atmospheric air. At these concentrations, there are $\sim 30 \cdot 10^6$ molecules of NO_2 in the sample volume (approximately a femtogram of NO_2). Thus LITA can be used for ultra-sensitive detection of trace species at atmospheric pressures and higher. This sensitivity arises from the linear signal dependence on species concentration at trace levels. For abundant species, the signal dependence on concentration may be quadratic or quartic, depending upon the tuning of the driver and source lasers. Multiplex LITA, has been successfully demonstrated. This technique provides $|\chi^{(1)}|^2$ spectra like that of Rayleigh scattering. Species concentrations may be measured in a single laser shot using this technique, provided the nonresonant susceptibility is suitably low.

The effects of turbulence on the LITA signals has been explored using a stirring fan mounted inside the bomb. At high pressures in CO_2, the fan is capable of generating flows with Reynolds numbers $\sim 10^6$. Turbulence on multiple scales evidently affected the rate of decay of the signal from the thermal grating. The lifetime of the mean signals was found to scale with estimated Kolmogorov and Taylor time scales. Eddies were observed to slice the thermal gratings, leaving coherent grating parts which moved with a relative velocity, evidenced by Doppler beating in the scattered signals. The velocities inferred by the Doppler beats correspond to those expected by dimensional analysis. This is the first application of heterodyne LITA velocimetry. LITA velocimetry has many advantages over laser-Doppler velocimetry: its signal beam is coherent, it requires no particle seeding, and it is readily applied to pulsed flows.

LITA is a new tool for the measurement of fluid properties. It excels at high pressures, where other techniques fail, admits simple, accurate modeling, and permits otherwise unobtainable remote, nonintrusive measurement of transport properties. Furthermore, LITA apparatus costs an order-of-magnitude less than many conventional diagnostic techniques. LITA can be applied to measure physical and spectroscopic properties of a gas in a single laser pulse. Given the early stage and unsophisticated nature of the experiments presented in Ch. 9, the accuracy of LITA measurements presented in Ch. 11 is good.

CHAPTER 13

Current and Future Work

Current and future work in LITA falls into three categories: technique extension, technique refinement, and technique application. As there exists considerable interest in LITA and associated grating techniques, the development effort will be distributed over several laboratories. The work described in this section reflects only that which will be pursued in the near future at GALCIT.

13.1 Technique Extension

Since the first single-shot narrowband LITA signals were detected a little over a year ago, LITA has been developed to the point that accurate sound-speed and thermal and viscous transport property measurement is practical and relatively simple. The sophistication of understanding of LITA obtained in this early analytical and experimental work opens the door to a large variety of related techniques.

LITA velocimetry, demonstrated in a primitive form using fan turbulence, will be developed into a technique which extends the range of application of laser velocimetry. LITA velocimetry may be expected to apply naturally to pulsed, unseeded, sooty, luminous flows, all of which contraindicate the use of the common laser-Doppler-velocimetry (LDV) technique. Heterodyne LITA velocimetry will be demonstrated on a pulsed jet and at the exit of a combustion-driven shock tube using the high-pressure bomb as a test-section. Both flow sources provide well-defined flow conditions, allowing comparison of measured and theoretical velocities. The combustion driven shock tube can provide flows at up to ~7 km/s, allowing LITA velocimetry to be tested at higher velocities than have ever been attempted using LDV.

The use of multiplex LITA for absolute species concentration measurements and rotational temperature measurements will be explored. Such a technique could be useful in the study of the formation of pollutants in combustors, the study of combustion in RAMJET and SCRAMJET engines, and other flows which involve chemical reactions.

LITA is usually not limited to point measurements by signal strength concerns, except at low pressures. One dimensional (linear) and two dimensional (planar) LITA measurements are not *a priori* excluded. The difficulty with these techniques is the need to make measurements using an array of detectors. If the signal is to be time-resolved, an enormous data recording rate is required. Two techniques appear to be within reach with the equipment at GALCIT. The first is simple 2-D imaging of the integrated or peak LITA signal using a CCD or intensified CCD 2-D array. This would provide a semi-quantitative image of the resonant-species concentration field. The second involves sweeping in time the image of a LITA signal from a line in the gas across a 2-D CCD array in the manner of a "streak camera." This poses far more serious challenges than the planar imaging, but provides more easily quantifiable information.

The measurement of species diffusion rates by LITA should be possible using photophoresis as the opto-acoustic effect. For photophoresis to be important, the driver laser must have a pulse that is comparable to or longer than the time-scale of diffusion across a grating wavelength. The flashlamp-pumped dye laser (FPDL), in narrowband operation, should be suitable for this purpose. Alternatively, the argon-ion laser could be used to drive and the FPDL used as the source laser, although with a sacrifice in tunability. Photolysis and resonant multiphoton ionization may be other candidates for forming species concentration gratings. These techniques have the advantage of not needing a long-pulse laser but suffer from large secondary effects (such as strong heating, acoustic and nonlinear wave formation, etc.).

Finally, several interesting effects which were observed and tested during these early studies may prove to be worthy of further consideration. LITA may measure small-scale turbulent properties of a flowing gas. A pulsed laser with a suitable repetition rate (e.g., a copper-vapor laser) could time-resolve the effect of the convection

of thermal gratings. By changing the characteristic scales of the gas and gratings, different scales of turbulence can be studied. The ability to make measurements from gratings that have propagated or convected from their point of formation suggests some interesting applications. By probing the grating with a suitably large source beam, the Lagrangian gas-property field in a flowing gas may be measured. For example, a grating with planes normal to a shock wave could be formed upstream of the shock wave. The change in properties as the grating convects or propagates through the shock wave would be evident in the signal. While there are many potential complications to this type of experiment, the possibility of making Lagrangian field measurements is interesting. LITA can explore rarefied-gas effects using simple, well-defined perturbations. The increase in effective sound speed was observed in LITA experiments with Knudsen number of the order unity. Effects on transport properties can likewise be measured and compared with the predictions of, for instance, the Chapmann-Enskog or Boltzmann equations.

13.2 Technique Refinement

The experimental capabilities and technique surrounding the narrowband LITA experiments has improved dramatically from the earliest tests. The adverse effects of beam misalignment, incomplete mixing, beam-steering, etc., have been addressed as they have been identified. Given the quality of the theoretical LITA model, and the large ratios of LITA signal-to-noise in the current system, the limit of sound-speed measurements above atmospheric pressure in careful experiments *should* be half the uncertainty of the temperature measurement in the bomb, ~0.015%. This degree of uncertainty is considerably higher than that of other standard sound-speed measurement techniques. The measurement of transport properties above one atmosphere should be less than 1% uncertain in experiments with exceptional beam alignment, as was seen in air after the beam alignment was tweaked. With the current arrangement, such "tweaking" is apparently needed to counter beam steering effects. For precision measurements over broad pressure excursions, unfocused beams may be used to eliminate the need for tweaking. Bulk viscosity measurements will likewise benefit from the use of unfocused beams.

The robustness of LITA experiments must also be refined in order for LITA to succeed in measurements on, for instance, the T5 free-piston shock tunnel. Foremost is the need to improve the strength of the signals, which will be accomplished, in part, by converting the FPDL to operate with a narrow bandwidth emission. The intensity of the signals obtained using the FPDL as a source laser will be $\sim 10^6$ times those obtained comparably using the argon-ion laser. This increase in signal strength permits the use of a large-diameter source beam to mitigate beam steering effects and solid-state detector arrays in line- and plane-imaging experiments described earlier.

13.3 Technique Application

Several applications of LITA that are under development have already been described. LITA will be used to measure velocities, sound-speeds, transport-properties, and species concentration in a combustion-driven shock tube and ultimately T5. Work in collaboration with Dr. M. Brown of MetroLaser seeks to apply LITA to tests at NASA Lewis of a high-pressure, next-generation, jet-engine combustor.

LITA will also continue to be used to measure gas properties in the static test cell. Of primary interest are the transport properties of near critical and supercritical gases. Supercritical water, almost a universal solvent, has been proposed for the elimination of particularly hazardous organic wastes. Vigorous chemical reactions occur in supercritical water which rapidly decompose organics into simple, nonhazardous component elements and molecules. There has been little quantitative study of transport phenomena in supercritical fluids, particularly quantitative measurement of mutual (species dependent) diffusivities which are important in modeling and understanding reaction dynamics. Initially, supercritical CO_2 will be studied because of its readily-accessible critical point. Ultimately supercritical water should be studied, although this will require a new test chamber.

References

Abrams, R. L. and Lind, R. C. (1978) "Degerenate four-wave mixing in absorbing media," *Opt. Lett.*, **2**, 94–96.

Bélanger, J. (1993) *Studies of Mixing and Combustion in Hypervelocity Flows with Hot Hydrogen Injection*, PhD. Thesis, Calif. Inst. of Technology, Pasadena, CA.

Berne, B. J. and Pecora, R. (1976) *Dynamic Light Scattering*, New York: John Wiley & Sons, Inc.

Bervas, H., Attal-Trétout, B., Le Boiteux, S. and Taran, J. P. (1992) "OH detection and spectroscopy by DFWM in flames; comparison with CARS," *J. Phys. B*, **25**, 949–969.

Boyd, R. W. (1992) *Nonlinear Optics*, (San Diego, CA: Academic Press), pp 126–143, pp 327–331.

Bloembergen, N. (1965) *Nonlinear Optics*, Reading, MA: W. A. Benjamin.

Boersch, H. and Eichler, H. J. (1967) *Z. Angew. Phys.* **22**, 378.

Brown, M. S., Rahn, L. A. and Dreier, T. (1992) "High-resolution degenerate four-wave mixing spectral profiles of OH," *Opt. Lett.*, **17**, 76–79.

Buntine, M. A., Chandler, D. W. and Hayden, C. C. (1995) "Detection of Vibrational-Overtone Excitation in Water via Laser-Induced Grating Spectroscopy," *J Chem. Phys.*, **102**, 2718–2726.

Chapman, S. (1970) *The Mathematical Theory of Non-uniform Gases*, 3rd ed., Cambridge University Press.

Charmet, J. C., Cloitre, M., Fermigier, M., Guyon, E., Jenffer, P., Limat, L. and Petit, L. (1986) "Application of Forced Rayleigh Scattering to Hydrodynamic Measurements," *IEEE J. Quant. Elect.*, **22**, 1461–1468.

Cooper, J., Charlton, A., Meacher, D. R., Ewart, P. and Alber, G. (1989) "Revised theory of resonant degenerate four-wave mixing with broad-bandwith lasers," *Phys. Rev. A*, **40**, 5705–5715.

Cooper, G. A. J. and Ewart. P. (1985) "Theory of resonant degenerate four-wave mixing with broad-bandwidth lasers," *Phys. Rev. A*, **31**, 2344–2352.

Cummings, E. (1992) "Techniques of single-shot thermometry by degenerate four-wave mixing," GALCIT Report FM 92-2, Calif. Inst. of Technology, Pasadena, CA.

Cummings, E. B. (1993) "Laser-induced Thermal Acoustics (LITA): Four-wave Mixing Measurement of Sound Speed, Thermal Diffusivity, and Viscosity," Proceedings of the International Conference on Lasers 1993, SOQUE, McLean, VA, 441–450.

Cummings, E. B. (1994a) "Laser-induced Thermal Acoustics (LITA): Simple, Accurate Single-shot Gas Measurements," 1994 Technical Digest Series, Vol 5, Optical Society of America, Washington, DC.

Cummings, E. B. (1994b) "Laser-induced Thermal Acoustics (LITA): Simple Accurate Gas Measurements," *Opt. Lett.***19**, pp 1361–1363.

Cummings, E. B., Leyva, I. A. and Hornung, H. G. (1995) "An expression for laser-induced thermal acoustic signals from finite beams," *Appl. Opt.*, to be published in May 1995.

Desai, R. C., Levenson, M. D. and Barker, J. A. (1983) "Forced Rayleigh scattering: Thermal and acoustic effects in phase-conjugate wave-front generation," *Phys. Rev. A*, **27**, 1968–1976.

Dreier, T. and Rakestraw, D. J. (1990) "Degenerate Four-Wave Mixing Diagnostics on OH and NH Radicals in Flames," *Appl. Phys. B*, **50**, 479–485.

Duarte, F. J. (1981) *High Power Dye Lasers*, New York: Springer-Verlag.

Eckbreth, A. C. (1988), *Laser Diagnostics for Combustion Species and Temperature*, Cambridge, MA: Abacus Press.

Eichler, H., Enterlein, G., Glozbach, P., Munschau, J. and Stahl, H. (1972) "Power Requirements and resolution of Real-Time Holograms in Saturable Absorbers and Absorbing Liquids," *Appl. Opt.*, **11**, 372–375.

Eichler, H. J., Günter, P., and Pohl, D. W. (1986) *Laser-Induced Dynamic Gratings*, New York: Springer-Verlag.

Einstein, A. (1910) *Ann. Phys.* **30**, 1275.

Ewart, P. and Maczmarek, M. (1991) "Two-dimensional mapping of temperature in a flame by degenerate four-wave mixing in OH," *Appl. Opt.*, **30**, 3996–3999.

Ewart, P. and Snowdon, P. (1990) "Multiplex degererate four-wave mixing in a flame," *Opt. Lett.*, **15**, 1403–1405.

Faris, G. W., Jusinski, L. E., Dyer, M. J., Bischel, W. K. and Hickman A. P. (1990) "High-resolution Brillouin gain spectroscopy in fused silica," *Opt. Lett.*, **15**, 703–705.

Fourkas, J. T., Brewer, T. R., Kim, H. and Fayer, M. D. (1991) "Picosecond time-resolved four-wave mixing experiments in sodium-seeded flames," *Opt. Lett.*, **16**, 177–179.

Gomez, A. and Rosnier, D. E. (1993) "Thermophoretic Effects on Particles in Counterflow Laminar Diffusion Flames," *Combust. Sci. and Tech.*, **89**, 335–362.

Govoni, D. E., Booze, J. A., Sinha, A. and Crim F. F. (1993) "The non-resonant signal in laser-induced grating spectroscopy of gases," *Chem. Phys. Lett.*, **216**, 525–529.

Green, M. S. and Sengers, J. V., editors, (1966) *Critical Phenomena; Proceedings of a Conference ...*, National Bureau of Standards Miscellaneous Publication, 107–132.

Gruneisen, M. T., Gaeta, A. L. and Boyd, R. W. (1985) "Eaxct theory of pump-wave propagation and its effect on degenerate four-wave mixing in saturable-absorbing media," *J. Opt. Soc. Am. B*, **2**, 1117–1121.

Herman, R. M. and Gray. M. A. (1967) "Theoretical prediction of the stimulated thermal Rayleigh scattering in liquids," *Phys. Rev. Lett.*, **19**, 824–828.

Hilsenrath, J. (1955) *Tables of Thermal Properties of Gases*, NBS Circular 564.

Hirschfelder, J. O., Curtiss, C. F. and Bird, R. B. (1954) *Molecular Theory of Gases and Liquids*, New York: John Wiley & Sons, Inc.

Hornung, H. G. (1992) "Performance data of the new free-piston shock tunnel at GALCIT", AIAA 92-3943.

Hu. P. H., Goldstone, J. A. and Ma, S. S. (1989) "Theoretical study of phase conjugation in stimulated Brillouin scattering," *J. Opt. Soc. Am. B*, **6**, 1813–1822.

Key, P. Y., Harrison, R. G., Little, V. I. and Katzenstein J. (1970) "Bragg Reflection from a Phase Grating Induced by Nonlinear Optical Effects in Liquids," *IEEE J.*

Quant. Elect., **6**, 641–646.

Köhler, W. (1993) "Thermodiffusion in polymer solutions as observed by forced Rayleigh scattering," *J. Chem. Phys.*, **98**, 660–668.

Kummrow, A., Woggon, S. and Lau, A. (1994) "Forced light scattering by broad-bandwidth incoherent pump lasers," *Phys. Rev. A*, **50**, 4264–4275.

Landau, L. D. and Liftshitz, E. M. (1960) *Electrodynamics of Continuous Media*, Cambridge, MA: Addison-Wesley Publishing Company, Inc., pp 377–383.

Landau, L. and Placzek, G. (1934) *Physik Z. Sowjetunion*, **5**, 172.

Lucht, R. P., Farrow, R. L., Rakestraw, D. J. (1993) "Saturation effects in gas-phase degenerate four-wave mixing spectroscopy – nonperturbative calculations," *J. Opt. Soc. B* **10**, 1508–1520.

Masson, B. S. (1991) "Nonlinear evolution of a stimulated Brillouin scattering dynamic grating in a fluid," *J Opt. Soc. Am. B*, **8**, 378–383.

Meacher, D. R., Charlton, A. and Ewart, P. (1990) "Degenerate four-wave mixing with broad-bandwidth pulsed lasers," *Phys. Rev. A*, **42**, 3018–3027.

Meijer, G. and Chandler, D. W. (1992) "Degenerate four-wave mixing on weak transitions in the gas phase using a tunable excimer laser," *Chem. Phys. Lett.*, **192**, 1–3.

Miller, E. J., Skeldon, M. D. and Boyd, R. W. (1989) "Spatial evolution of laser beam profiles in an SBS amplifier," *Appl. Opt.*, **28**, 92–96.

Miller, R. J. D., Casalegno R., Nelson, K. A., and Fayer, M. D. (1982) "Laser-induced ultrasonics: a dynamic holographic approach to the measurement of weak absorptions, optoelastic constants and acoustic attenuation," *Chem. Phys.*, **72**, 371–379.

Mountain, R. D. (1966) "Spectral Distribution of Scattered Light in a Simple Fluid," *Rev. Modern Phys.*, **38**, 205–214.

Nelson, K. A. and Fayer, M. D. (1980) "Laser induced phonons: A probe of intermolecular interactions in molecular solids," *J. Chem. Phys.*, **72**, 5202–5218.

Nelson, K. A., Lutz, D. R.. Fayer, M. D. and Madison, L. (1981) "Laser-induced phonon spectroscopy. Optical generation of ultrasonic waves and investigation of

electronic excited-state interations in solids," *Phys. Rev. B*, **24**, 3261–3275.

Ottusch, J. J. and Rockwell, D. A. (1991) "Stimulated Brillouin scattering phase-conjugation fidelity fluctuations," *Opt. Lett.*, **16**, 369–371.

Paul, P., Farrow, R. L. and Danehy, P. M. (1995) "The Characteristics of Thermal Gratings Produced in a DFWM Scattering Geometry," *J. Opt. Soc. B*, to be published.

Perry, R. H., Green, D. W. and Maloney, J. O., editors (1984) *Perry's Chemical Engineers' Handbook, 6th Edition*, New York: McGraw-Hill, 3-270–272.

Pohl, D., Reinhold, I. and Kaiser, W. (1968) "Experimental Observation of Stimulated Thermal Brillouin Scattering," *Phys. Rev. Lett.*, **20**, 1141–1143.

Press, W. H., Flannery. B. P., Teukolsky, S. A. and Vetterling, W. T. (1986) *Numerical Recipes*, Cambridge University Press.

Rakestraw, D. J., Farrow, R. L. and Dreier, T. (1990) "Two-dimensional imaging of OH in flames by degenerate four-wave mixing," *Opt. Lett.*, **15**, 709–711.

Ramsey, J. M. and Whitten, W. B. (1987) "Degenerate Four-Wave Mixing as a Spectrochemical Analysis Technique," *Anal. Chem.*, **59**, 167–171.

Rose, T. S., Wilson, W. L., Wäckerle, G. and Fayer, M. D. (1987) "Gas phase dynamics and spectroscopy probed with picosecond transient grating experiments," *J Chem. Phys.*, **86**, 5370–5391.

Schelonka, L. P., and Kramer, M. A. (1989) "Theory of thermal blooming correction by phase conjugation," *Opt. Lett.*, **14**, 949–951.

Shen, Y. R. (1986) "Basic considerations of Four-Wave Mixing and Dynamic Gratings," *IEEE J. Quant. Elect.*, **22**, 1196–1203.

Siegman A. E. (1977) "Bragg diffraction of a Gaussian beam by a crossed-Gaussian volume grating," *J. Opt. Soc. Am.*, **67**, 545–550.

Stampanoni-Panariello, A., Hubschmid, W. and Hemmerling, B. (1994) "Laser Diagnostics by Electrostrictive Gratings in the Gas Phase," in *Laser Applications to Chemical Analysis*, 1994 Technical Digest Series, Vol. 5 (Optical Society of America, Washington, DC), 119–123.

Tasjian, D., (1988) Cynosure, Wiggins, MA, private communication.

Thompson, P. A. (1988) *Compressible-Fluid Dynamics*, Maple Press Co.

Vander Wal, R. L., Holmes, B. E., Jeffries, J. B., Danehy, P. M., Farrow, R. L. and Rakestraw, D. J. (1992) "Detection of HF using infrared degenerate four-wave mixing," *Chem. Phys. Lett.*, **191**, 251–258.

Vargaftik, N. B., Filippov, L. P., Tarzimanov, A. A. and Totskii, E. E. (1994) *Handbook of Thermal Conductivity of Liquids and Gases*, CRC Press.

Vincenti, W. G. and Kruger, C. H. (1977) *Introducton to Physical Gas Dynamics*, Huntington, NY: Robert E. Krieger Publishing Company.

Watkins, D. E., Ridley, K. D. and Scott, A. M. (1989) "Self-pumped four-wave mixing using backward and forward Brillouin scattering," *J, Opt. Soc. Am. B*, **6**, 1693–1700.

Watkins, D. E., Scott, A. M. and Ridley, K. D. (1990) "Effect of signal frequency on four-wave mixing through stimulated Brillouin scattering," *Opt. Lett.*, **15**, 1267–1269.

Weise, N., Eichler, J. and Salk, J. (1989) "Nonlinear Complex Susceptibility of Cresyl Violet Solution Measured with a Dynamic Grating Method," *IEEE J. Quant. Elect.*, **25**, 403–407.

Williams, S., Rahn, L. A., Paul, P. H., and Forsman, J. W. (1994) "Laser-Induced Thermal Grating Effects in Flames," *Opt. Lett.*, **19**, 1681–1683.

Winter, M. and Radi, P. P. (1992) "Nearly degenerate 4-wave mixing using phase-conjugate pump beams," *Opt. Lett.*, **17**, 320–322.

Yiping, C. Rao, D. N. and Prasad, P. N. (1992) "Investigation of Laser-Induced Acoustic Phonons in Poly(*p*-phenylenevinylene) Uniaxially Stretched Films," *J. Phys. Chem*, **96**, 5617–5622.

Appendices

APPENDIX A

Linear Scattering

Linear scattering occurs when perturbations in a medium disrupt the phase of wave propagating through the medium. Some of the energy of the waves is redirected out of the original path or "dephased." Scattering or dephasing is a phenomenon which can occur in any system described by a wave equation. Weak scattering may be quantified using a perturbation method or linearized model. An equation for linear light scattering is used in the analysis in Ch. 7. The derivation of this equation is presented in this appendix so that assumptions and approximations used in the derivation are clear. The scattering equation has relevance outside light scattering, for example in the (linear) scattering or dephasing of sound waves. When multiple scattering—scattering of scattered waves—becomes important, the analysis of the scattered waves becomes much more complicated. The analysis simplifies again when scattering occurs on a length scale that is comparable or shorter than the wavelength. In this limit, the wave propagates diffusively.

LITA employs "linear" scattering of an applied optical electric field (the source beam) by a medium with weak perturbations (thermal/acoustic gratings). The derivation that follows is adapted only slightly from that of Landau and Liftschitz (1960) and Berne and Pecora (1976). The incident and scattered fields are denoted by the subscript o and s (consistent with the subscripts for the source and signal beam in LITA) and the total fields by no subscript.

$$\begin{aligned} \mathbf{E} &= \mathbf{E}_o + \mathbf{E}_s, \\ \mathbf{D} &= \mathbf{D}_o + \mathbf{D}_s, \\ \mathbf{H} &= \mathbf{H}_o + \mathbf{H}_s, \end{aligned} \tag{A.1}$$

where $\mathbf{E}$ is the electric field vector, $\mathbf{D}$ is the "displacement" vector, and $\mathbf{H}$ is the magnetic field vector of the light in the medium.* Both the total and incident fields

* The magnetic field vector $\mathbf{H}$ should not be confused with the length scale H, nor should the displacement vectors be confused with diffusivities.

satisfy Maxwell's equations; thus, by the linearity of the equations, the scattered fields must also comply,

$$\nabla \times \mathbf{E}_s = -\frac{1}{c}\frac{\partial \mathbf{H}_s}{\partial t}, \tag{A.2a}$$

$$\nabla \times \mathbf{H}_s = \frac{1}{c}\frac{\partial \mathbf{D}_s}{\partial t}, \tag{A.2b}$$

$$\nabla \cdot \mathbf{H}_s = 0, \tag{A.2c}$$

$$\nabla \cdot \mathbf{D}_s = 0. \tag{A.2d}$$

Taking the curl of Eq. A.2a and substituting Eq. A.2b eliminates $\mathbf{H}_s$,

$$\nabla \times \nabla \times \mathbf{E}_s = -\frac{1}{c^2}\frac{\partial^2 \mathbf{D}_s}{\partial t^2}. \tag{A.3}$$

Assume that the perturbation creates in the medium a dielectric field

$$\epsilon(\mathbf{r},t) = \epsilon_0[(1+\chi_0)\mathbf{I} + \boldsymbol{\chi}_1(\mathbf{r},t)], \tag{A.4}$$

where, ϵ_0 is the vacuum permittivity, χ_0 is the unperturbed material susceptibility, and $\boldsymbol{\chi}_1(\mathbf{r},t)$ is the susceptibility perturbation field, which is given a tensor form for generality,** and is much smaller than χ_0. Thus

$$\begin{aligned}\mathbf{D}/\epsilon_0 &= [(1+\chi_0)\mathbf{I} + \boldsymbol{\chi}_1]\cdot(\mathbf{E}_o + \mathbf{E}_s) \\ &= (1+\chi_0)\mathbf{E}_o + \boldsymbol{\chi}_1 \cdot \mathbf{E}_o + (1+\chi_0)\mathbf{E}_s + \boldsymbol{\chi}_1 \cdot \mathbf{E}_s.\end{aligned} \tag{A.5}$$

Using Eq. A.1 and $\mathbf{D}_s/\epsilon_0 = (1+\chi_0)\mathbf{E}_s$, and assuming $\mathbf{E}_s << \mathbf{E}_o$, one obtains, by neglecting the second-order term in Eq. A.5, namely $\boldsymbol{\chi}_1 \cdot \mathbf{E}_s$,

$$\mathbf{D}_s/\epsilon_0 = (1+\chi_0)\mathbf{E}_s + \boldsymbol{\chi}_1 \cdot \mathbf{E}_o. \tag{A.6}$$

Using the vector identity $\nabla \times \nabla \times \mathbf{A} = -\nabla^2\mathbf{A} + \nabla(\nabla \cdot \mathbf{A})$ and substituting Eq. A.6 into Eq. A.3 provides the forced wave equation for the scattered displacement field,

$$\nabla^2 \mathbf{D}_s/\epsilon_0 - \frac{1+\chi_0}{c^2}\frac{\partial^2 \mathbf{D}_s}{\partial t^2} = -\nabla \times \nabla \times (\boldsymbol{\chi}_1 \cdot \mathbf{E}_o). \tag{A.7}$$

** This permits consideration of aleotropic behavior of the scattering medium. Among other opto-acoustic effects, the driver laser can induce molecular orientation or alignment, leading to an aleotropic susceptibility perturbation. These effects are not treated in the main analysis, which assumes material isotropy, but are readily inserted.

Substituting the Hertz vector, $\boldsymbol{\pi}_s$, of the scattered field, defined by $\mathbf{D}_s \equiv \nabla \times \nabla \times \boldsymbol{\pi}_s$, into Eq. A.7 simplifies the form of the forcing term,

$$\frac{\nabla^2 \boldsymbol{\pi}_s}{\epsilon_0} - \frac{1+\chi_0}{c^2}\frac{\partial^2 \boldsymbol{\pi}_s}{\partial t^2} = -\boldsymbol{\chi}_1 \cdot \mathbf{E}_o, \tag{A.8}$$

which has the formal solution

$$\boldsymbol{\pi}(\mathbf{R},t) = \frac{\epsilon_0}{4\pi}\int_V \frac{\boldsymbol{\chi}_1(\mathbf{r},t') \cdot \mathbf{E}_o(\mathbf{r},t')}{|\mathbf{R}-\mathbf{r}|}\, d^3r, \tag{A.9a}$$

$$t' \equiv t - \frac{\sqrt{\epsilon_0(1+\chi_0)}}{c}|\mathbf{R}-\mathbf{r}|. \tag{A.9b}$$

The vector $\mathbf{R}$ is the position vector of the of the point at which the scattered field is sought (the point of observation). The vector $\mathbf{r}$ is the position vector of the volume element d^3r of the the scattering volume V. The parameter t', the "reduced time," accounts for the finite light propagation time from the scattering element to the point of observation. Consider the incident light to be a (quasi-) monochromatic finite plane wave, such as is found at the focus of a Gaussian beam, with an electric field distribution

$$\frac{1}{2}\mathbf{E}_o(\mathbf{r},t)\exp i(\mathbf{k}_o \cdot \mathbf{r} - \omega_o t') + \text{c.c.} \tag{A.10}$$

Assume the envelope of the electric field changes slowly enough that the susceptibility may be regarded as constant over the homogeneously-broadened incident-beam frequency range. Eq. A.9a may be manipulated using the definition of the Hertz vector to obtain the scattered electric field distribution, $^{\dagger}\mathbf{E}_s(\mathbf{R},t)$,

$$\mathbf{E}_s(\mathbf{R},t) = \frac{1}{2}\nabla \times \left[\nabla \times \frac{1}{4\pi}\int \frac{\boldsymbol{\chi}_1(\mathbf{r},t';\omega_o)\cdot \mathbf{E}_o(\mathbf{r},t)}{|\mathbf{R}-\mathbf{r}|}\exp i(\mathbf{k}_o\cdot\mathbf{r} - \omega_o t')\, d^3r\right] + \text{c.c.} \tag{A.11}$$

Assuming that the scattered field will be detected far from the scatterer, the distance $|\mathbf{R}-\mathbf{r}|$ may be approximated by $R - \mathbf{r}\cdot\hat{\mathbf{e}}_s$, where $\hat{\mathbf{e}}_s$ is the unit vector in the $\mathbf{R}$-direction. Then Eq. A.9b becomes

$$t' \simeq t - \sqrt{\frac{\epsilon_0(1+\chi_0)}{c}}(R - \mathbf{r}\cdot\hat{\mathbf{e}}_s). \tag{A.12}$$

Define the scattering dipole moment density vector, $\boldsymbol{\mu}_s(\mathbf{r},t) = \boldsymbol{\chi}_s(\mathbf{r},t)\cdot\mathbf{E}_i(\mathbf{r},t)$. In terms of its temporal Fourier transform, $\boldsymbol{\mu}(\mathbf{r},\omega)$, the dipole moment density field is

$$\boldsymbol{\mu}_s(\mathbf{r},t') = \int_{-\infty}^{\infty} \boldsymbol{\mu}_s(\mathbf{r},\omega)\exp(-i\omega t')\, d\omega. \tag{A.13}$$

---

† This expression for the electric field assumes the detector resides in a medium of weak susceptibility.

Defining $\omega_s \equiv \omega_o + \omega$, $\mathbf{k}_p \equiv \sqrt{\epsilon_0(1+\chi_0)}\omega_s \hat{\mathbf{e}}_s/c$, and $\mathbf{q}_p \equiv \mathbf{k}_0 - \mathbf{k}_p$, substituting Eq. A.13 and neglecting terms of higher order than $1/R$, Eq. A.11 becomes

$$\mathbf{E}_s(\mathbf{R},t) = \frac{1}{2}\frac{1}{4\pi R}\int_{-\infty}^{\infty} \exp i(k_p R - \omega_o t)\mathbf{k}_p \times \left[\mathbf{k}_p \times \int_V \exp i[(\mathbf{k}_o - \mathbf{k}_p)\cdot\mathbf{r}]\,\boldsymbol{\mu}_s(\mathbf{r},\omega)\,d^3r\right] + \text{c.c.} \quad (A.14)$$

The scattering dipole moment density fluctuations are assumed to be limited to frequencies much lower than that of the incident light, thus $\omega_s \simeq \omega_o$. Therefore, assume $|\mathbf{k}_p| \simeq |\mathbf{k}_s| \simeq |\mathbf{k}_o|$, then

$$\mathbf{E}_s(\mathbf{R},t) = \frac{1}{2}\frac{1}{4\pi R}\exp i[k_s R - \omega_o t]\mathbf{k}_s \times \left[\mathbf{k}_s \times \int_V \exp(i\mathbf{q}\cdot\mathbf{r})\boldsymbol{\chi}_1(\mathbf{r},t)\cdot\mathbf{E}_o(\mathbf{r},t)\,d^3r\right] + \text{c.c.}, \quad (A.15)$$

where the expression for the dipole energy density field has been replaced and $\mathbf{k}_s$, the wave vector of the scattered light, and $\mathbf{q} \equiv \mathbf{k}_o - \mathbf{k}_s$, the *scattering vector* have been defined. This past step in the analysis simply avoids a temporal convolution over fluctuations in the scattering dipole moment field, for example, amplitude noise in the incident light, by assuming a large separation in time scales of the fluctuation and oscillation frequency. In some cases, this is not valid. In nearly *all* cases, the (hydrodynamic) evolution of the susceptibility perturbation is slow compared to the frequencies of the incident light.‡ The integration in Eq. A.15 is the three-dimensional spatial Fourier transform of the scattering dipole moment density, $\boldsymbol{\mu}_s(\mathbf{q},t)$. Using the vector identity $\mathbf{A}\times(\mathbf{B}\times\mathbf{C}) = \mathbf{B}(\mathbf{A}\cdot\mathbf{C}) - \mathbf{C}(\mathbf{A}\cdot\mathbf{B})$, and $\mathbf{E}_s\cdot\mathbf{k}_s = 0$, one obtains from manipulation of Eq. A.15,

$$\mathbf{E}_s(\mathbf{R},t) = \frac{-k_s^2}{4\pi R}\cos(k_s R - \omega_o t)\,\boldsymbol{\mu}_s(\mathbf{q},t), \quad (A.16)$$

which is the starting point in Ch. 7.

The relatively simple result for light scattering bears some discussion. The electric field $\mathbf{E}_s$ at a point $\mathbf{R}$ is proportional to a single component of the Fourier transform of the scattering dipole moment density field, $\boldsymbol{\mu}(\mathbf{q},t)$, where $\mathbf{q} = \mathbf{k}_o - \mathbf{k}_s$ is the scattering vector. Laser-induced grating or coherent scattering techniques exploit this property. The scattering dipole field of a grating-shaped perturbation has a sharply peaked Fourier transform. The scattering vector at the scattering peak is called the *phase-matched* or *Bragg* scattering vector. By aligning the grating-forming and scattering

‡ The same is not necessarily true in population-grating or exciton techniques, as the evolution of these gratings and therefore their susceptibility perturbation may be much faster.

beams so that they are carefully phase-matched, the scattered signal can be coherently enhanced by many orders of magnitude. Because the perturbation is weighted by the incident field, the effect of diffraction is included. Diffraction obviously is important in an analysis of the effects of finite beams. However, if only scattering is to be considered, the incident field may be assumed to be an infinite plane wave, as in the analyses from which this derivation was adapted (see, for example, Berne (1976)). Conversely, if one wants only to examine diffraction phenomena, the perturbation may be made uniform in space. The linear scattering of sound waves may be treated in an analogous manner starting either with the equations of hydrodynamics or simply the wave equation for the propagation of pressure perturbations, with a similar result. An expression for linear scattering of sound waves is derived in Chernov (1960), along with equations for the attenuation from dephasing of a sound wave. This dephasing phenomenon has been observed in LITA signals taken in CO_2 near its liquid-vapor critical point, where large density (and therefore acoustic impedance) fluctuations spontaneously form.

APPENDIX B

Complete Finite-Beam Expression for Homodyne LITA

The complete expression for the homodyne-detected LITA signal including all the diffusion terms and the convolutions over the driver beam pulse-shapes is

$$\frac{\mathcal{L}_{hom}}{P_o^2(t)} = \frac{k_o^2 w^4}{16\pi^2 \cos^2\phi}|\chi(\omega_o)|^2 \int_0^\infty \int_0^\infty P_d(t-\tau_1)P_d(t-\tau_2)$$

$$\times \Bigg[\mathrm{Re}\Bigg\{ 2A_P^2 N_P(\tau_1)N_P(\tau_2)\sqrt{\frac{4\zeta_P(\tau_1)\xi_P(\tau_1)\zeta_P(\tau_2)\xi_P(\tau_2)}{(\xi_P^2(\tau_1)+\xi_P^2(\tau_2))\,(\zeta_P^2(\tau_1)+\zeta_P^2(\tau_2))}}$$

$$\times \exp\left(-2c_s^2\left[\frac{\tau_1^2\xi_P^2(\tau_1)}{\mathbf{H}_P^4(\tau_1)}+\frac{\tau_2^2\xi_P^2(\tau_2)}{\mathbf{H}_P^4(\tau_2)}\right]\right)\Sigma_P(\tau_1)\Sigma_P(\tau_2)$$

$$+4A_PA_TN_P(\tau_1)N_T(\tau_2)\sqrt{\frac{4\zeta_P(\tau_1)\xi_P(\tau_1)\zeta_T(\tau_2)\xi_T(\tau_2)}{(\xi_P^2(\tau_1)+\xi_T^2(\tau_2))\,(\zeta_P^2(\tau_1)+\zeta_T^2(\tau_2))}}$$

$$\times \exp\left(\frac{-2\xi_P^4(\tau_1)c_s^2\tau_1^2}{\mathbf{H}_P^4(\tau_1)(\xi_P^2(\tau_1)+\xi_T^2(\tau_2))}\right)\Sigma_P(\tau_1)\Sigma_T(\tau_2)$$

$$+4A_PA_DN_P(\tau_1)N_D(\tau_2)\sqrt{\frac{4\zeta_P(\tau_1)\xi_P(\tau_1)\zeta_D(\tau_2)\xi_D(\tau_2)}{(\xi_P^2(\tau_1)+\xi_D^2(\tau_2))\,(\zeta_P^2(\tau_1)+\zeta_D^2(\tau_2))}}$$

$$\times \exp\left(\frac{-2\xi_P^4(\tau_1)c_s^2\tau_1^2}{\mathbf{H}_P^4(\tau_1)(\xi_P^2(\tau_1)+\xi_D^2(\tau_2))}\right)\Sigma_P(\tau_1)\Sigma_D(\tau_2)\Bigg\}$$

$$+2A_PA_P^*N_P(\tau_1)N_P^*(\tau_2)\sqrt{\frac{4\zeta_P(\tau_1)\xi_P(\tau_1)\zeta_P(\tau_2)\xi_P(\tau_2)}{(\xi_P^2(\tau_1)+\xi_P^2(\tau_2))\,(\zeta_P^2(\tau_1)+\zeta_P^2(\tau_2))}}\Sigma_P(\tau_1)\Sigma_P^*(\tau_2)$$

$$+2A_TA_DN_T(\tau_1)N_D(\tau_2)\sqrt{\frac{4\zeta_T(\tau_1)\xi_T(\tau_1)\zeta_D(\tau_2)\xi_D(\tau_2)}{(\xi_T^2(\tau_1)+\xi_D^2(\tau_2))\,(\zeta_T^2(\tau_1)+\zeta_D^2(\tau_2))}}\Sigma_T(\tau_1)\Sigma_D(\tau_2)$$

$$+A_T^2N_T(\tau_1)N_T(\tau_2)\sqrt{\frac{4\zeta_T(\tau_1)\xi_T(\tau_1)\zeta_T(\tau_2)\xi_T(\tau_2)}{(\xi_T^2(\tau_1)+\xi_T^2(\tau_2))\,(\zeta_T^2(\tau_1)+\zeta_T^2(\tau_2))}}\Sigma_T(\tau_1)\Sigma_T(\tau_2)$$

$$+A_D^2N_D(\tau_1)N_D(\tau_2)\sqrt{\frac{4\zeta_D(\tau_1)\xi_D(\tau_1)\zeta_D(\tau_2)\xi_D(\tau_2)}{(\xi_D^2(\tau_1)+\xi_D^2(\tau_2))\,(\zeta_D^2(\tau_1)+\zeta_D^2(\tau_2))}}\Sigma_D(\tau_1)\Sigma_D(\tau_2)\Bigg]\,d\tau_1\,d\tau_2 \quad (B.1)$$

This expression applies when $\ell^2 >> w^2$, i.e., small values of the beam-crossing angle, θ, because finite-beam size effects in the $x-$direction were ignored for brevity. This expression appears to model experimental signals fairly well even if the driver beams depart significantly from their Gaussian ideal. Accurate source beam alignment, however, is very important, particularly in experiments using focused beams.